The role of cannabinoid receptor 2 in toll-like receptor-mediated microglial activation

Doctoral thesis
to obtain a doctorate (PhD)
from the Faculty of Medicine
of the University of Bonn

Bolanle Fatimat Olabiyi

from Osogbo, Nigeria

2023

Written with authorization of

the Faculty of Medicine of the University of Bonn

First reviewer: Prof. Dr. Andreas Zimmer

Second reviewer: Prof. Dr. Waldemar Kolanus

Day of oral examination: 24.08.2023

From the Institute of Molecular Psychiatry

Director: Prof. Dr. Andreas Zimmer

Table of Contents

List of abbreviations **7**

1. Introduction **14**

1.1 Microglia: Origin, history and functions 14

1.2 Microglia: Key mediator of innate immune response 17

1.3 Toll-like receptor signaling 17

1.4 Role of metabolism in microglial activation 20

1.5 Role of microglial activation in neuroinflammation 21

1.6 Endocannabinoid system 22

1.7 Cannabinoid receptor 2 signaling 23

1.8 Common/Available tools for studying the function of CB2 25

1.8.1 CB2 knockout 25

1.8.2 CB2 pharmacological model 25

1.9 CB2 in neuroinflammation 27

1.10 CB2 and TLR signaling crosstalk: Influence on microglial activation 28

1.11 Aim of the project 29

2. Materials and Methods **30**

2.1 Devices and equipment 30

2.2 Chemicals/reagents 31

2.3 List of drugs and stimulants 33

2.4 Antibodies 33

2.5 Consumables 34

2.6 Solutions/buffer 35

2.7 Mice 38

2.7.1 Experimental groups 39

2.8 Genotyping 39

2.8.1 DNA isolation 39
2.8.2 DNA amplification by polymerase chain reaction 39
2.8.3 Gel electrophoresis 40
2.9 Cell culture experiments 41
2.9.1 Primary neonatal microglia culture 41
2.9.2 Organotypic hippocampal slice culture preparation 42
2.9.3 Bone marrow-derived macrophages 43
2.10 Stimulation of cultured cells 44
2.11 Immunocytochemistry 45
2.12 Protein analysis 45
2.12.1 Protein isolation 45
2.12.2 BCA protein assay 46
2.12.3 Automated western blotting by Simple Western™ 46
2.13 Flow cytometry 48
2.14 Immunohistochemistry, image acquisition and image analysis 49
2.14.1 Iba1 and CD68 staining 49
2.14.2 Image acquisition by confocal microscopy 50
2.14.3 Microglial morphology analysis using MotiQ (Image J plugin) 50
2.14.4 Image analysis using ImageJ (CD68 intensities) 51
2.15 ELISA (Enzyme-linked immunosorbent assay) 52
2.16 Seahorse analysis 54
2.17 Statistical analysis 56
2.18 Collaborators and integrated project 56
3. Results 57
3.1 Role of CB2 in TLR-induced microglial activation (Genetic knockout studies) 57
3.1.1 Primary microglia from $CB2^{-/-}$ mice are less responsive to TLR stimulation 57
3.1.2 Protein analysis of MAPK, Akt and NF-κB phosphorylation in TLR-stimulated microglia 60

3.2 Role of CB2 in TLR-induced microglial activation (Pharmacological inhibition studies) 65
3.2.1 The CB2 antagonist SR144528 suppresses TLR-induced microglial cytokine secretion only at high concentration 65
3.2.2 SR144528 has no effect on cytokine secretion in unstimulated microglia 67
3.2.3 SR144528 (at nM) does not affect CD68 intensity in the CA1 region of OHSCs before and after TLR stimulation 68
3.2.4 SR144528 (at nM) does not affect microglial Iba1 and CD68 intensities in TLR-stimulated OHSCs 72
3.2.5 SR144528 (at nM) does not considerably alter microglial morphology in TLR stimulated OHSCs 75
3.2.6 SR144528 (at nM) does not influence cytokine secretion in TLR4-stimulated Bone marrow-derived macrophages 78
3.2.7 SR144528 (at 1 μM) reduced TLR4-induced microglial inflammatory cytokine secretion independent of CB2 receptors 80
3.2.8 SR144528 (at 1 μM) decreased CD68 activity in the CA1 region of TLR4-stimulated OHSCs in a CB2 independent manner 80
3.2.9 SR144528 (at 1 μM) does not act via CB2 to modulate TLR4-induced microglial Iba1 and CD68 intensities in OHSCs 83
3.2.10 SR144528 (at 1 μM) alters microglial morphology in TLR4 stimulated OHSCs independent of CB2 85
3.2.11 SR144528 (at 1 μM) has no effect on cell death and cell surface maker expression in TLR4 stimulated microglia 87
3.2.12 Effect of CB2 activation on LPS/IFN-γ-induced microglial cytokine secretion 89
3.3 Role of CB2 in LPS/IFN-γ-induced metabolic reprogramming in microglia (Pharmacological inhibition vs CB2 knockout studies) 90
3.3.1 $CB2^{-/-}$ microglia show improved maximal respiration before and after LPS/IFN-γ stimulation 90
3.3.2 $CB2^{-/-}$ macrophages show similar metabolic activity as in WT macrophages after LPS/IFN-γ stimulation 92

3.3.3 SR144528 (at 1 μM) marginally influences seahorse metabolic activity in LPS/IFN-γ stimulated microglia 94
3.3.4 SR144528 (at 1 μM) does not influence seahorse metabolic activity in LPS/IFN-γ stimulated Bone marrow-derived macrophages 96

4. Discussion 99

4.1 CB2 deletion decreases inflammatory profile in TLR-stimulated microglia 100

4.2 Molecular mechanism by which CB2 induce TLR-mediated microglial activation 101

4.3 Pharmacological blockade of CB2 receptor does not affect TLR-induced microglial activation 103

4.4 Pharmacological blockade of CB2 receptor does not affect TLR4-induced cytokine secretion in bone marrow-derived macrophages 105

4.5 SR144528 (at 1 μM) reduced TLR4-induced microglial inflammatory cytokine secretion independent of the CB2 receptor 105

4.6 Differential effects of $CB2^{-/-}$ and pharmacological inhibition on glucose metabolic parameters in TLR4-induced microglial activation 108

4.7 $CB2^{-/-}$ or pharmacological inhibition does not affect glucose metabolic parameters in TLR4-induced bone marrow-derived macrophages 109

4.8 Conclusions 110

5. Abstract 112

6. List of figures 113

7. List of tables 115

8. References 116

9. Acknowledgements 131

10. List of publications 132

List of abbreviations

2-AG	2-arachidonoylglycerol
3D	Three-dimensional
AA	Arachidonic acid
AD	Alzheimer's disease
AEA	Anandamide or *N*-arachidonoylethanolamine
Akt/PKB	Protein kinase B
ANOVA	Analysis of variance
AP1	Activator protein 1
APC	Allophycocyanin
APP	Amyloid beta-precursor protein
Arg1	Arginase 1
ATP	Adenosine triphosphate
AU	Arbitrary unit
Aβ	Amyloid beta
BBB	Blood-brain barrier
BCA	Bicinchoninic acid
BMDMs	Bone marrow-derived macrophages
bp	Base pair
BSA	Bovine serum albumin
CA1	Cornu Ammonis area 1
cAMP	Cyclic adenosine monophosphate
CB1	Cannabinoid receptor 1
CB2	Cannabinoid receptor 2
$CB2^{-/-}$	Constitutive knockout of CB2 receptor

CBD	Cannabidiol
CCL2 (MCP-1)	C-C motif chemokine ligand 2/ monocyte chemoattractant protein-1
cDNA	Complementary DNA
CD	Cluster of differentiation
cDNA	Complementary DNA
Cnr1	Cannabinoid receptor 1 (gene)
Cnr2	Cannabinoid receptor 2 (gene)
CNS	Central nervous system
CO_2	Carbon dioxide
COX-2	Cyclooxygenase-2
CpG	5′-Cytosine-phosphate-Guanine-3’ oligodeoxynucleotide
CREB	cAMP-response element binding protein
DAGL	Diacylglycerol lipase
DAMPs	Damage-associated molecular patterns
DAPI	4′,6-diamidino-2-phenylindole
DC	Dendritic cell
DG	Dentate gyrus
dH_2O	Deionised water
DMEM	Dulbecco’s Modified Eagle Medium
DMSO	Dimethyl sulfoxide
DNA	Deoxyribonucleic acid
dNTP	Deoxyribose nucleoside triphosphate
ds RNA	Double stranded RNA
DTT	Dithiothreitol
ECAR	Extracellular acidification rate

eCBs	Endocannabinoids
ECS	Endocannabinoid system
EDTA	Ethylenediaminetetraacetic acid
E	Embryonic day
ELISA	Enzyme-linked immunosorbent assay
ERKs	Extracellular signal-regulated kinases
EtBr	Ethidium bromide
EtOH	Ethanol
FAAH	Fatty acid amide hydrolase
FACS	Fluorescence-activated cell sorting/flow cytometry
FBS	Fetal bovine serum
FCCP	Carbonyl cyanide-4 (trifluoromethoxy) phenylhydrazone
FITC	Fluorescein isothiocyanate
FSC	Forward scatter count
GABA	Gamma aminobutyric acid
GLUT1	Glucose transporter 1
gMFI	Geometric mean fluorescence intensity
GPCRs	G-protein coupled receptors
GPR55	G-protein coupled receptor 55
HD	Huntington's disease
hr	Hour/hours
HBSS	Hanks' balanced salt solution
HIF-1α	Hypoxia inducible factor-1 subunit alpha
Hprt	Hypoxanthine-guanine phosphoribosyl transferase
HRP	Horseradish peroxidase

Iba1	Ionized calcium-binding adapter molecule-1
ICAM-1	Intercellular adhesion molecule-1
ICC	Immunocytochemistry
IFNs	Interferons
IFN-γ	Interferon-γ
IgG	Immunoglobulin G
IHC	Immunohistochemistry
IKK	Inhibitor of NF-κB kinase
IL	Interleukin
iNOS	Inducible nitric oxide synthase
IP_3	Inositol 1,4,5-triphosphate
IP-10	IFN-inducible protein of 10 kDa
IRAKs	Interleukin-1 receptor-associated kinases
IRFs	Interferon regulatory factors
IRF3/IRF7	Interferon regulatory factor-3/7
JNK	JUN N-terminal kinase
JWH-133	John William Huffman 133
LPS	Lipopolysaccharide
LRRs	Leucine-rich repeats
MAGL	Monoacylglycerol lipase
MAPKs	Mitogen-activated protein kinases
M-CSF	Macrophage colony-stimulating factor
MEM	Minimum essential medium
MGV	Mean gray value
min	Minutes

MKK	MAPK kinase
mM	Millimolar
mRNA	Messenger RNA
mTOR	Mammalian target of rapamycin
MyD88	Myeloid differentiation primary response protein 88
N	Sample size (number)
n.s.	Not significant
N/A	Numerical aperture
Na-Azide	Sodium azide
NAPE-PLD	N-acyl phosphatidylethanolamine phospholipase D
NF-κB	Nuclear factor kappa light chain enhancer of activated B cells
NGS	Normal goat serum
NO	Nitric oxide
NOS2	Nitric oxide synthase 2
OCR	Oxygen consumption rate
OD	Optical density
OXPHOS	Oxidative phosphorylation
OHSCs	Organotypic hippocampal slice cultures
PAMPs	Pathogen-associated molecular patterns
PBS	Phosphate-buffered saline
PCR	Polymerase chain reaction
PD	Parkinson’s disease
PE	Phycoerythrin
PerCP	Peridinin-chlorophyl-cyanine 5.5
PFA	Paraformaldehyde

PI3K	Phosphatidylinositol-3-kinase
PIP2	Phosphatidylinositol 4,5-bisphosphate
PK	Protein kinase
PLC	Phospholipase C
PLL	Poly-L-Lysine
PolyI:C	Polyinosinic-polycytidylic acid
PRRs	Pattern recognition receptors
pyr	Pyramidal
Raf	Rapidly accelerated fibrosarcoma
RIPA	Radioimmunoprecipitation assay
RNA	Ribonucleic acid
ROI	Region of interest
ROS	Reactive oxygen species
rpm	Rounds per minute
RPMI	Rosewell park memorial institute medium
RT	Room temperature
SDS	Sodium dodecyl sulfate
SEM	Standard error of the mean
SSC	Side scatter count
ssRNA	Single stranded RNA
TAE	Tris-acetate-EDTA
TE	Tris-EDTA
THC	Tetrahydrocannabinol
TIR	Toll/interleukin 1 receptor/resistance protein
TLRs	Toll-like receptors

TMB	3,3',5'5'-tetramethylbenzidine
TNF-α	Tumor necrosis factor-alpha
TRAF6	Tumour necrosis factor receptor-associated factor 6
TRAM	TRIF-related adapter molecule
TRIF	TIR-domain containing adapter protein inducing interferon beta
TRIS	Tris (hydroxymethyl) aminomethane
TRPV1	Vanilloid receptor type 1
UV	Ultraviolet
WT	Wild type

1. Introduction

1.1 Microglia: Origin, history and functions

Microglia were first identified in 1899 by Nissl, who described them as rod-like shaped cells (Stäbchenzellen) with phagocytic and migratory capacities (Nissl, 1899). The following year, they were thought to be phagocytic cells called mesoglia originating from the mesoderm and distinct from neurons or neuroglia (Robertson, 1900). The term ‘microglia’ was first coined by del Rio-Hortega, who used it to describe macrophages penetrating the brain during embryonic development (del Rio-Hortega, 1919, 1932). Microglia were therefore initially thought to be bone marrow-derived monocytes that travel through the bloodstream to differentiate into tissue resident macrophages. However, this origin was highly debated for many years until the recent last decade when emerging studies established that microglia are of true embryonic origin (Ginhoux et al., 2010, 2013; Kierdorf et al., 2013). Early during development, between embryonic days E7.5 and E8.5 in mice, hematopoietic cells in the yolk sac blood island give rise to microglia progenitors (**Figure 1.1**). These developing microglia progenitors then migrate to the brain and other tissues, where they differentiate into fetal microglia around E9.5 (Ginhoux et al., 2010, 2013; McGrath et al., 2003).

Besides the yolk sac-derived microglia progenitors, a second wave of hematopoietic myeloid precursor emerges from the fetal liver around E12.5 (Ginhoux & Prinz, 2015; Naito et al., 1990). The monocytes derived from fetal liver travel through the bloodstream to differentiate in various tissues; the brain is an exemption because it is safeguarded by the blood-brain barrier (BBB) at E13.5 (**Figure 1.1**). Furthermore, a third group of myeloid cells originating from the bone marrow has also been reported to colonize the brain during inflammation or in pathological conditions (Hoeffel & Ginhoux, 2018; Soulet & Rivest, 2008; Priller et al., 2001) (**Figure 1.1**). These pathologically-derived macrophages exhibit microglial-like features and may even form a lasting population in the brain (Cuadros et al., 2022; Lund et al., 2018; Cronk et al., 2018). Nevertheless, it is now generally accepted that the term ‘microglia’ refers to the brain resident myeloid cells of yolk sac origin - the specialized innate immune cell of the central nervous system (CNS) (Cuadros et al., 2022).

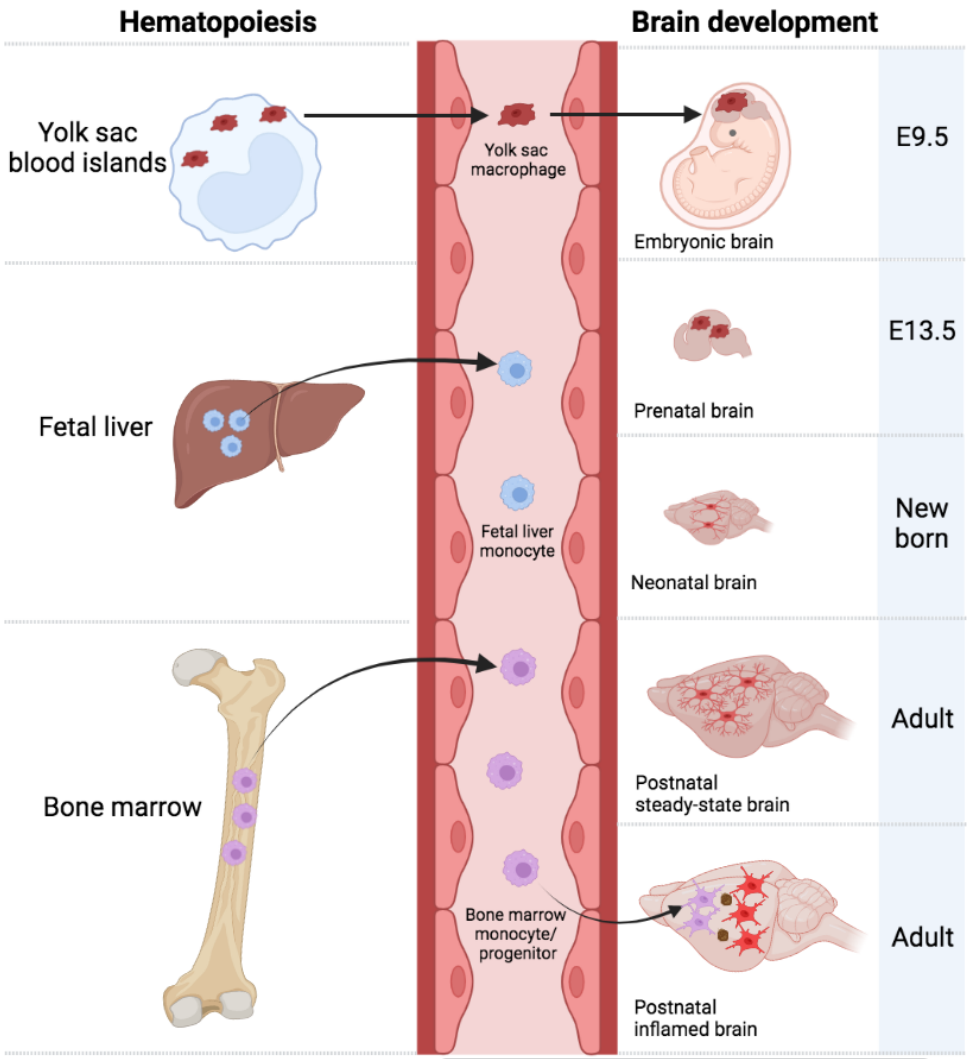

Figure 1.1: Origin of microglia from yolk sac progenitors. During early development (E9.5), primitive microglia progenitors from yolk sac blood islands migrate to the brain and develop into microglia. Formation of blood-brain barrier BBB begins at E13.5, thereby preventing the fetal liver-derived macrophages from entering the developing brain. After birth, growing microglia with high proliferative potential colonize the central nervous system till adulthood is reached. In the normal brain, the population of microglia is maintained through regulated proliferation. However, during inflammation coupled with disturbed blood-brain barrier permeability, myeloid cells derived from bone marrow can be recruited into the brain to become an integral network of the brain. However, the process is still not fully understood. Figure adapted from (Ginhoux et al., 2013).

Microglia represent about 5 - 20 % of the whole glia population in the brain (Hugh Perry, 1998; Yang et al., 2010). A key characteristic of microglia that distinguishes them from other types of glial cells is their dynamic nature (Colonna & Butovsky, 2017; Parkhurst & Gan, 2010). They exhibit diverse morphological states depending on the stage of development and activation mode (Stratoulias et al., 2019; Savage et al., 2019). These

include ameboid, ramified and reactive states. Microglia are mostly ameboid during the perinatal stage of development. This is then transformed into the ramified state at the postnatal stage. The highly branched ramified microglia with thin processes are the most predominant forms in the adult CNS (Smolders et al., 2019; Cuadros & Navascués, 1998). Reactive or activated microglia, on the other hand, are often associated with pathological or inflammatory conditions (Deczkowska et al., 2018). They have morphological features that resemble that of the developing ameboid microglia with large cell bodies and short branches/protrusions (**Figure 1.2**).

Microglia primarily function as surveillance entities that strive to maintain homeostatic balance in the CNS (Casano & Peri, 2015; Colonna & Butovsky, 2017). As the specialized cells of the innate immune system, they are essential in mediating immune response to invading pathogens or threats (Casali & Reed-Geaghan, 2021; Muzio et al., 2021).

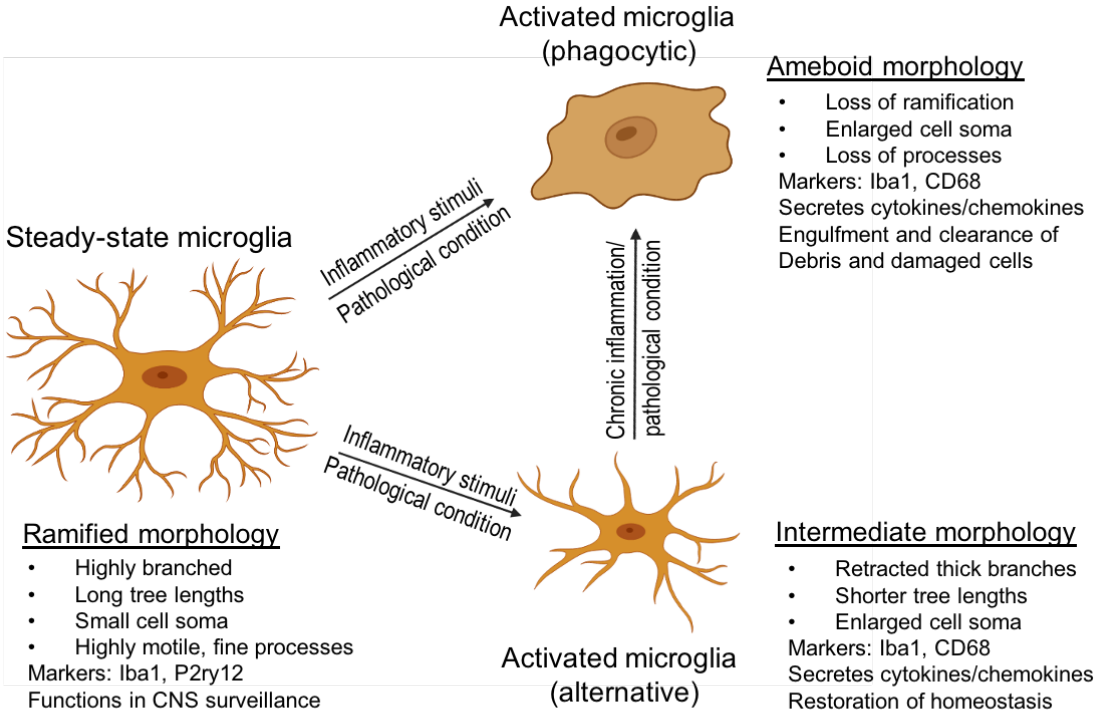

Figure 1.2: Microglia morphology in homeostatic and activated states. Microglia in the adult brain can assume at least three morphological forms depending on activation mode. In steady-state, microglia are highly ramified with long, thin and fine processes. Upon exposure to inflammatory stimuli or acute pathological conditions, they transform into a less ramified state with thick retracted processes, lower branches and enlarged soma. During chronic inflammation/pathological conditions, microglia's ramification is lost with ameboid morphology and enlarged soma. Modified from (Edler et al., 2021; Lier et al., 2021).

1.2 Microglia: Key mediator of innate immune response

Microglia, being an integral part of the first line of defense against infections or harmful stimuli, their response is usually rapid and unspecific (Brubaker et al., 2015). In the healthy brain, microglia constantly survey their surrounding with their highly branched and mobile processes to sense any changes or pathogenic attacks in the CNS (Nimmerjahn et al., 2005). To detect danger signals, microglia are equipped with pattern recognition receptors (PRRs) such as toll-like receptors (TLRs) that identify pathogen-associated molecular patterns (PAMPs) or damage-associated molecular patterns (DAMPs) like viral or bacterial molecules (Takeda et al., 2003; Barton & Medzhitov, 2003). The binding of TLRs to their respective DAMPs or PAMPs triggers a cascade of intracellular signaling that generally results in rapid microglial activation and subsequently elicits an inflammatory response. This response is often characterized by the secretion of pro-inflammatory cytokines and chemokines, including interleukin-6 (IL-6), tumor necrosis factor-alpha (TNF-α), C-C motif chemokine ligand 2 (CCL2), and additionally; reactive oxygen species (ROS), and growth factors (Wolf et al., 2017). These TLR-mediated microglial responses are tightly regulated, keeping the CNS innate immunity in check.

1.3 Toll-like receptor signaling

Toll-like receptors (TLRs) are classified as transmembrane proteins that interact with PAMPs and DAMPs to elicit an innate immune response. TLRs are one of many PRRs expressed in diverse immune cells, including microglia (Vijay, 2018). They are highly conserved across species ranging from nematodes like *Caenorhabditis elegans* (Tenor & Aballay, 2008) to *Drosophila melanogaster* (Hashimoto et al., 1988), to humans (Medzhitov et al., 1997) as well as other animal species (Vaure & Liu, 2014). To date, at least 13 TLRs are recognized in mammals. TLRs are primarily classified based on their localization in the cell and the DAMPs they recognize (Roh & Sohn, 2018). For example, TLRs 1-2, 4-6, and 10 are cell surface bound; they primarily bind to the bacterial components, lipopolysaccharide (LPS) and lipoproteins (**Figure 1.3**). TLRs 3, 7-9, and 13 are in turn endosomal based; they interact with single/double-stranded ribonucleic acid (RNA) and deoxyribonucleic acid (DNA) (**Figure 1.3**).

TLR signaling is initiated by the binding of DAMPs or PAMPS to the extracellular domain of TLRs, containing the leucine-rich repeats (LRRs) (Akira & Takeda, 2004;

Takeda et al., 2003). The receptor-ligand complex causes a conformational change leading to the recruitment of adapter proteins like Toll/interleukin-1 receptor/ resistance protein (TIR)-domain containing adapter protein inducing interferon beta (TRIF) and myeloid differentiation primary response protein 88 (MyD88). TLR3 mainly recruits the TRIF, while all other TLRs recruit the MyD88 (Duan et al., 2022; Fiebich, Batista, et al., 2018). Notably, TLR4 can recruit both MyD88 and TRIF because it can be endocytosed from the cell surface to the endosome, where it can switch from MyD88 to TRIF (**Figure 1.3**). Depending on the adapter activated, a cascade of intracellular signaling is induced via the TRIF or MyD88-dependent pathways (O'Neill et al., 2013).

The MyD88 pathway involves additional interaction with proteins like tumour necrosis factor receptor-associated factor 6 (TRAF6) and interleukin-1 receptor-associated kinases (IRAKs), leading to a phosphorylation cascade involving the mitogen-activated protein kinases (MAPKs). The kinases subsequently activate transcription factors such as nuclear factor kappa light chain enhancer of activated B cells (NF-κB) or interferon regulatory factors (IRFs) which enter the nucleus to bring about the transcription of pro-inflammatory mediators (Aderem & Ulevitch, 2000; Duan et al., 2022; Takeda et al., 2003). Such pro-inflammatory mediators include cytokines like TNF-α, IL-1β, IL-6, IL-12, and chemokines like CCL2 (Kielian, 2006).

The TRIF pathway recruits TRAF3 and TRIF-related adapter molecule (TRAM), which triggers downstream intracellular events leading to the translocation of IRF3 to the nucleus, thereby transcribing type 1 interferons (IFNs). Besides IRFs, the TRIF-dependent pathway can also activate the NF-κB transcription factor leading to a downstream pro-inflammatory response (Duan et al., 2022). Other transcription factors that might be involved in both signaling pathways include activator protein 1 (AP1) and cyclic adenosine monophosphate (cAMP)-response element binding protein (CREB).

Overall, microglial TLR activation via MyD88 or TRIF-dependent pathway is essential for innate immune response to threats or pathogens and therefore mediates inflammatory responses as a defense mechanism.

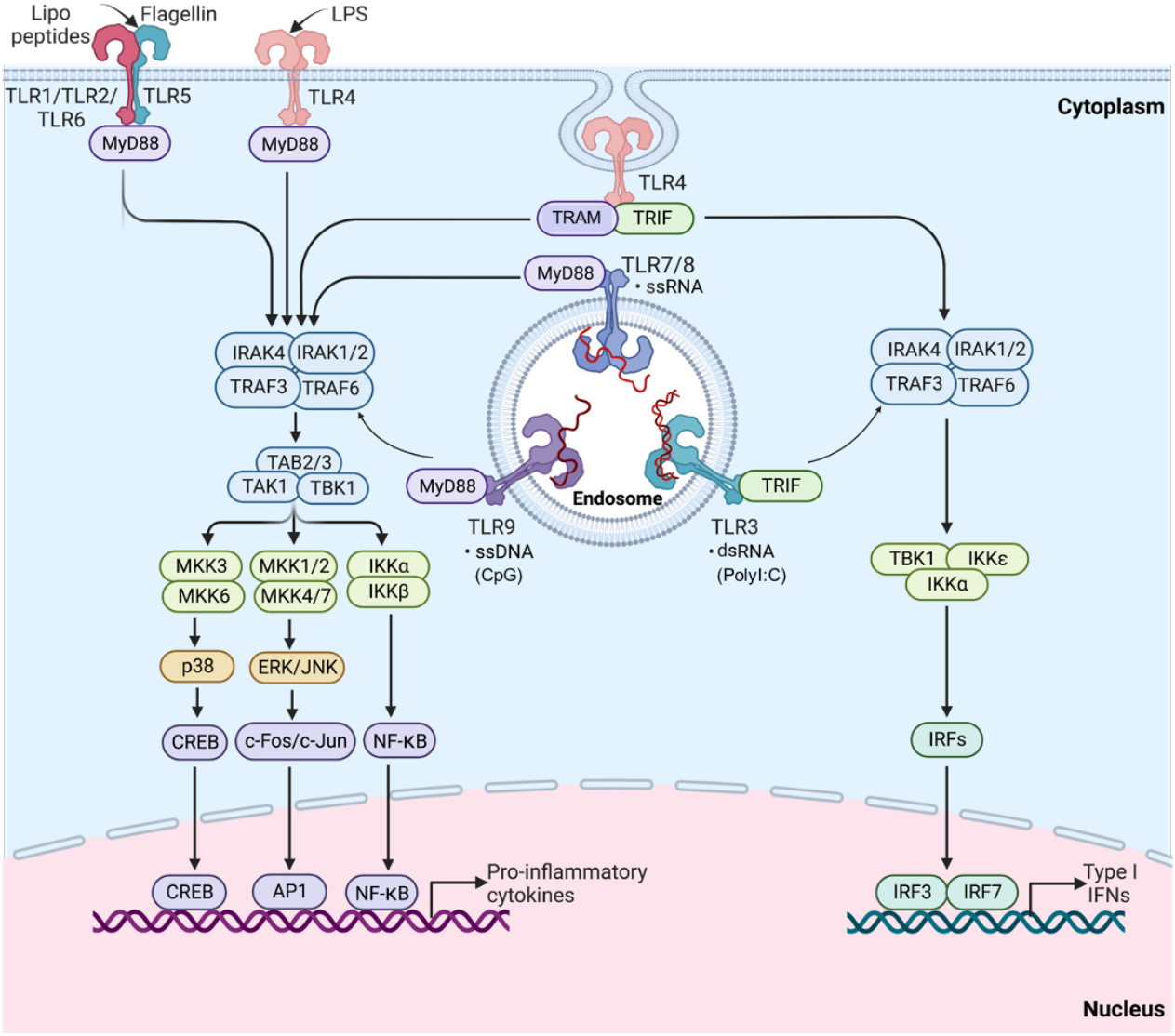

Figure 1.3: Toll-like receptor signaling pathway. TLR4 or TLR5 and heterodimers of TLR1-TLR2, TLR2-TLR6 interact with their respective DAMPs on the cell surface. In the endosome, TLR3, TLR7-9 bind to their bacterial or viral nucleic acid DNA or RNA components. The ligand-receptor complex induces dimerization of TLRs, which recruits adapter proteins such as myeloid differentiation primary response protein 88 (MyD88) or Toll/interleukin-1 receptor/ resistance protein (TIR)-domain containing adapter protein inducing interferon beta (TRIF). This further triggers a cascade of phosphorylation events involving mitogen-activated protein kinases (MAPKs) including extracellular signal-regulated kinases (ERKs), p38, and JUN N-terminal kinase (JNK) in the cell. The phosphorylated kinases subsequently activate the transcription factors including nuclear factor kappa light chain enhancer of activated B cells (NF-κB), activator protein 1 (AP1), cyclic adenosine monophosphate (cAMP)-response element binding protein (CREB) and interferon regulatory factors (IRFs), that enter the nucleus where they bind to the response element on the DNA to facilitate the expression of pro-inflammatory cytokines and type 1 interferons (IFNs). Modified version of (O'Neill et al., 2013) and (Duan et al., 2022).

1.4 Role of metabolism in microglial activation

Several glucose metabolic pathways are involved in maintaining energy homeostasis in immune cells, including microglia. Such pathways include glycolysis, which takes place in the cytosol and oxidative phosphorylation (OXPHOS) which occurs in the mitochondria. The end product of complete glucose metabolism is energy produced as adenosine triphosphate (ATP). The regulation of these pathways is necessary for normal microglia function (Bielanin & Sun, 2022). Over the last ten years, studies in the booming immunometabolism field have sought to characterize metabolic alterations that happen in activated immune cells. Under normal conditions, microglia primarily generate ATP via OXPHOS. However, upon exposure to inflammatory stimuli, microglia and macrophages switch their metabolism from OXPHOS to glycolysis (Baik et al., 2019; Bernier et al., 2020; Cheng et al., 2021; Kelly & Aj O'Neill, 2015; Lauterbach et al., 2019; Van den Bossche et al., 2017). This event is commonly known as metabolic reprogramming. (**Figure 1.4**).

The first evidence of this altered metabolism occurred in the 1920s when Otto Warburg observed a shift from oxidative metabolism to aerobic glycolysis in tumour cells (Warburg, 1925; Vander Heiden et al., 2009). This rewired metabolism was named the Warburg effect. In Warburg situation, cancer cells take up a high amount of glucose and convert it to lactate instead of pyruvate in the presence of oxygen, hence the term 'aerobic glycolysis'. It is now largely known that similar rewired metabolism also occurs in immune cells during activation (Kelly & Aj O'neill, 2015; Lauro & Limatola, 2020; O'Neill et al., 2016). Metabolic reprogramming during immune cell activation is often accompanied by a shift from an anti-inflammatory to a pro-inflammatory state where levels of cytokines and ROS become elevated (Cheng et al., 2021). Past studies have demonstrated that inhibition of glycolysis components, for example, glucose transporter 1 reduced the inflammatory responses in microglia (Wang et al., 2019). More so, treating macrophages with 2-deoxyglucose (an inhibitor of the glycolysis rate-limiting enzyme, hexokinase) reduced LPS-induced IL-1β secretion (Tannahill et al., 2013). Furthermore, 2-deoxyglucose suppressed TNF-α, IL-12, IL-6 and cluster of differentiation 40 (CD40) expression in dendritic cells stimulated with LPS (Cheng et al., 2021; Everts et al., 2014). Judging from these findings, it is evident that glucose metabolism has a significant role in microglial activation and inflammatory responses. A schematic representation of metabolic reprogramming in the immune cell is presented in **Figure 1.4**.

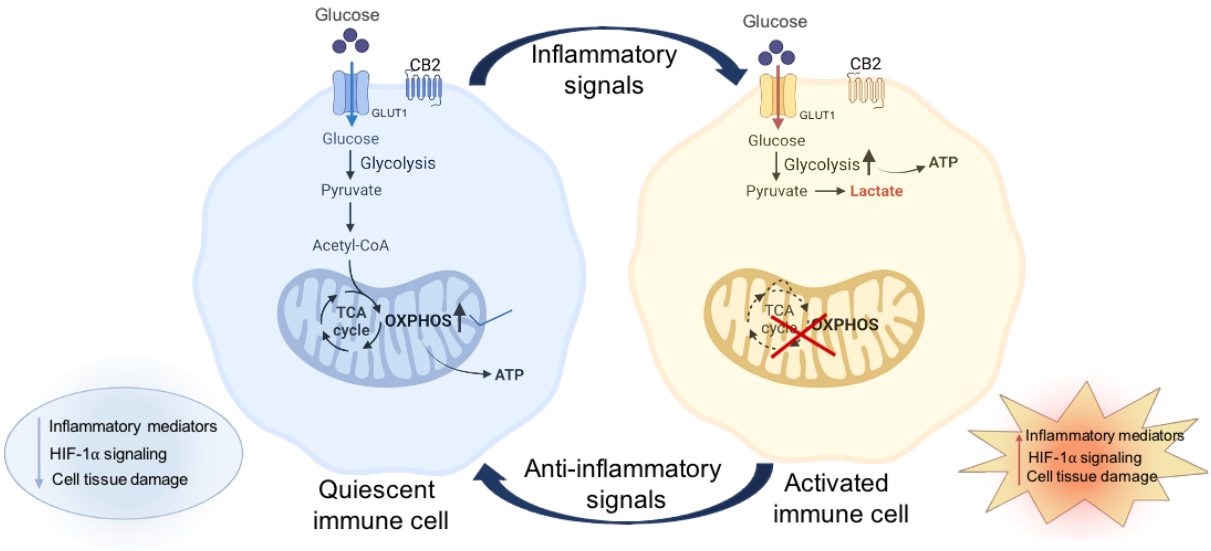

Figure 1.4: Metabolic reprogramming during immune cell activation. Regulated balance between glycolysis and OXPHOS is crucial for immune function. In a steady-state cell, OXPHOS is the main means of generating ATP. Exposure to inflammatory stimuli causes immune cells to switch metabolism from OXPHOS to glycolysis, causing a higher glycolysis rate for ATP production in these activated cells. Metabolic reprogramming is associated with increased production of inflammatory mediators, higher HIF1-α signaling and tissue damage. Abbreviations: OXPHOS: oxidative phosphorylation, ATP: adenosine triphosphate, GLUT1: glucose transporter 1, HIF1-α: hypoxia inducible factor-1 subunit alpha. Adapted from (Bielanin & Sun, 2022).

1.5 Role of microglial activation in neuroinflammation

Neuroinflammation has long been described as a hallmark of many neurodegenerative disorders, including Alzheimer's and Parkinson's diseases (Leng & Edison, 2021; Badanjak et al., 2021) among others. While microglia can play a protective role in innate immune defense, they have also been implicated in exacerbating neuroinflammation in these diseases (Wolf et al., 2017). Hence, microglia can serve as both friend and foe in neuroinflammation.

During inflammatory exposure, microglia are rapidly activated and they undergo morphological and functional changes to mediate inflammatory responses. This often includes a switch from ramified to ameboid form (Fernández-Arjona et al., 2019; Arcuri et al., 2017) and phagocytosis of damaged cells or harmful debris. Furthermore, activated microglia release pro-inflammatory cytokines (Wolf et al., 2017), which recruit other immune cells to the site of infection. Moreover, they secrete growth factors to promote repair and survival of the cell (Mado et al., 2023; Pons & Rivest, 2020). In light of this,

microglia may play a protective role in CNS. As long as homeostasis is maintained in the brain, acute microglial activation and inflammation are essential mechanisms to clear unwanted pathogens and damaged cells in the CNS. However, uncontrolled or prolonged microglial activation can lead to a chronic state of inflammation which can be detrimental and is often linked to many neuropathological disorders (Wolf et al., 2017; Streit et al., 2004). The pathogenic effects of microglial inflammation can largely be attributed to excessive secretion of pro-inflammatory cytokines, elevated levels of ROS and chemokines which can disturb the homeostasis in the brain.

Summarily, microglial activation can exacerbate or protect against neuroinflammation depending on the duration and extent of exposure to inflammatory stimuli. Hence, understanding microglial activation in response to inflammatory stimulation and identifying potential therapeutic targets for neuroinflammatory and -degenerative conditions is of great significance. One possible target that has been studied for its immunomodulatory effects in microglia and other immune cells is the cannabinoid receptor 2 of the endocannabinoid system (Komorowska-Müller & Schmöle, 2021).

1.6 Endocannabinoid system

The endocannabinoid system (ECS) is a complex neuromodulatory system that regulates numerous physiological processes ranging from synaptic function, mood regulation, appetite, neurogenesis, stress response, immune function to energy homeostasis (Castillo et al., 2012; de Melo Reis et al., 2021; Lu & Mackie, 2021; Oddi et al., 2020). The ECS consist of three major components: the endocannabinoids, the enzymes involved in synthesizing/degrading these endocannabinoids, and the cannabinoid receptors to which the cannabinoids bind to.

Endocannabinoids (endogenous cannabinoids, eCBs) are lipid-soluble molecules secreted upon demand. The most common eCBs are 2-arachidonoylglycerol (2-AG) and anandamide or *N*-arachidonoylethanolamide (AEA), which are synthesized via enzymatic reactions. The eCBs bind to the cannabinoid receptors to elicit the physiological function mentioned above (Mechoulam et al., 1995; Mechoulam & Parker, 2013). While 2-AG is regarded as a full agonist of the cannabinoid receptors, AEA is considered a partial agonist (Mecha et al., 2015). Besides eCBs, exogenous cannabinoids like plant-derived tetrahydrocannabinol (THC) and cannabidiol have been shown to also act on the

cannabinoid receptors to bring about psychotropic effects. THC is considered the primary psychoactive compound found in *Cannabis sativa* (marijuana hemp), and its use for psychoactive purposes dates back to about 12,000 years ago (Crocq, 2020).

The enzyme producing 2-AG is mainly diacylglycerol lipase (DAGL), whereas N-acylphosphatidylethanolamine phospholipase D (NAPE-PLD) synthesizes AEA. The degradation of 2-AG is mainly carried out by the enzyme monoacylglycerol lipase (MAGL), while fatty acid amide hydrolase (FAAH) breaks down AEA. However, both FAAH and NAPE-PLD can metabolize 2-AG (Basavarajappa, 2007).

The two main ECS receptors are the G-protein coupled receptors (GPCRs): cannabinoid receptor 1 (CB1) and cannabinoid receptor 2 (CB2), which share about 45 % homology (Zimmer et al., 1999; Munro et al., 1993). The CB1 is encoded by *Cnr1* gene and is abundant in the CNS; CB1 is highly expressed in neurons and has been shown to play a role in gamma aminobutyric acid (GABA)-ergic and glutamatergic neurotransmission (Howlett et al., 2002). Its high presence has also been reported in the cortex, hippocampus and cerebellum, where it regulates behaviour and cognition (Howlett et al., 2002). CB2 on the other hand, is weakly expressed on neurons. Its predominant location is in the immune cells like microglia (Komorowska-Müller & Schmöle, 2021; Schmöle et al., 2015), where it regulates immune function and neuroinflammation (López et al., 2018). Other known but less explored receptors of the ECS include G-protein coupled receptor 55 (GPR55) and vanilloid receptor type 1 (TRPV1) (Brown, 2007). This study focused on the CB2 receptor's role in microglial activation due to its association with immune regulation.

1.7 Cannabinoid receptor 2 signaling

CB2 signaling begins with the activation of the CB2 receptor by endogenous or exogenous ligands (**Figure 1.5**). Since CB2 is a GPCR coupled to the $G_{i/o}$ family of $\alpha\beta\gamma$ subunits, the $G_{i/o}\alpha$ subunit dissociates from $G\beta\gamma$ subunit during CB2 activation to inhibit adenylate cyclase, causing lower production of cAMP and subsequently reducing protein kinase A (PKA) activity (Howlett et al., 2002; Mccoy, 2016). The $G\beta\gamma$ subunit in turn, initiates a series of intracellular signaling cascade involving phosphatidylinositol-3-kinase (PI3K), phospholipase C (PLC) and rapidly accelerated fibrosarcoma (Raf) kinase. PLC converts phosphatidylinositol 4,5-bisphosphate (PIP2) to inositol 1,4,5-trisphosphate (IP_3), which

eventually causes calcium (Ca^{2+}) release. Whereas Raf kinase and PI3K further activate various MAPKs like ERK1/2, JNK and p38 MAPK which results in transcription factor activation and subsequent regulation of genes involved in cell survival, migration, inflammation and proliferation (Howlett et al., 2002; Kibret et al., 2022; Mccoy, 2016). CB2 activation can alternatively initiate the PI3K/Akt/mTOR signaling involving the protein kinase B (PKB) which is also referred to as Akt and downstream mammalian target of rapamycin (mTOR), thereby regulating cell growth, survival and metabolism (**Figure 1.5**) (McCoy, 2016).

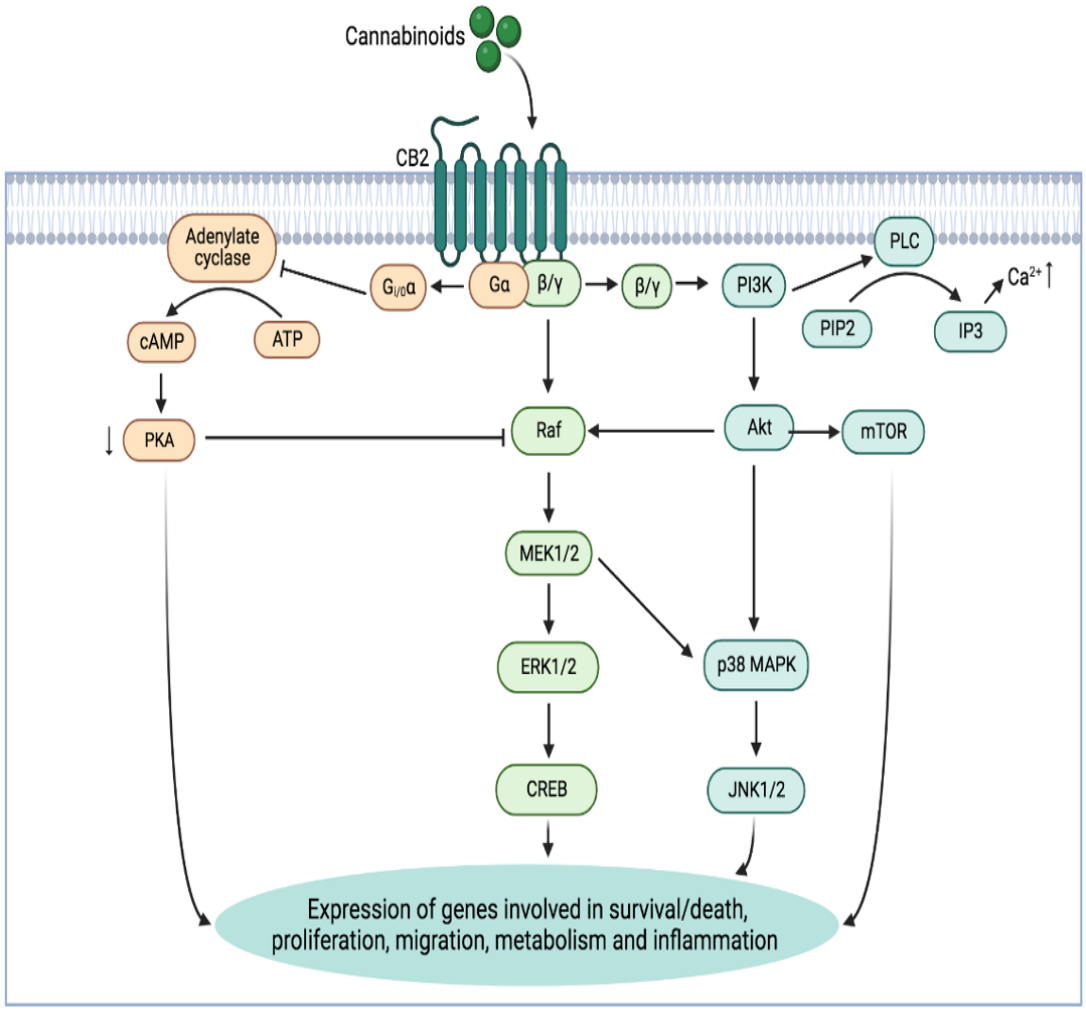

Figure 1.5: CB2 receptor signaling pathway. Upon binding of CB2 to cannabinoids, the $G_{i/o}\alpha$ subunit dissociates from $G\beta\gamma$ to inhibit adenylate cyclase, causing lower production of cAMP and reduced protein kinase A (PKA) activity. Unlike the $G_{i/o}\alpha$, the $G\beta\gamma$ activate MAPKs via Raf kinase or phosphatidylinositol-3-kinase (PI3K) induction. The activated MAPKs, JNK1/2, p38 or ERK1/2, can further trigger the transcription factors like CREB, consequently regulating survival/death, proliferation or inflammation. The $G\beta\gamma$ can also induce PI3K-mediated phospholipase C (PLC) conversion of phosphatidylinositol 4,5-

bisphosphate (PIP2) to inositol 1,4,5-trisphosphate (IP_3), which eventually raises intracellular calcium (Ca^{2+}) levels. Alternatively, $G\beta\gamma$ can activate PI3K/Akt/mTOR signaling leading to the regulation of genes involved in cell metabolism, proliferation, survival/death, and migration. Adapted from (McCoy, 2016).

1.8 Common/Available tools for studying the function of CB2

1.8.1 CB2 knockout model

Mice lacking CB2 receptors were first generated in 2000 (Buckley et al., 2000). Using homologous recombination, CB2 knockout ($CB2^{-/-}$) mice were created by replacing 341 base pairs of the coding exon 3 of the CB2 gene (*Cnr2*) with the neomycin sequence. This led to the deletion of 131 amino acids at the receptor‘s carboxyl terminal resulting in the ablation of transmembrane domains 6 and 7 as well as part of the intracellular loop 3.

Following the success of the $CB2^{-/-}$ mouse line generation, the authors compared the physical features like weight and size between the $CB2^{-/-}$ and their wild type (WT) counterparts and found no noticeable difference. They also reported that the psychotropic effects of THC were similarly active in both WT and $CB2^{-/-}$ mice (Buckley et al., 2000). Although, a study from another group showed hyperactivity of osteoclasts with decreased osteoblast precursors in $CB2^{-/-}$ mice, suggesting that $CB2^{-/-}$ mice may exhibit low bone mass phenotype (Ofek et al., 2006). But overall, $CB2^{-/-}$ was regarded as a promising tool for studying inflammation and immune activation (Turcotte et al., 2016), presumably due to its predominant expression in immune cells and its regulatory role in immune function.

1.8.2 CB2 pharmacological model

Many synthetic compounds have been employed to study CB2 function. Some of these compounds are preferred over others based on selectivity, efficacy and potency. The most commonly used synthetic CB2 agonist is JWH-133, while the most widely used CB2 antagonist is SR144528. Where a few compounds display selectivity for CB2 receptors, others may be unspecific. Table 1.1 summarizes the list of available CB2 agonists and antagonists known to modulate CB2 activity (Turcotte et al., 2016).

Both genetic and pharmacological models are regarded as valuable tools for studying the role of CB2 signaling in neuro-inflammatory conditions (Correa et al., 2005; Ehrhart et al., 2005; Aso et al., 2013; Schmöle et al., 2015). However, both methods come with advantages and disadvantages. Where constitutive or cell type-specific deletion of

CB2 receptors can provide information about CB2 functions (Komorowska-Müller et al., 2021), compensatory responses triggered by genetic manipulation may confound data interpretation. On the other hand, pharmacological approaches can provide information about the functional consequences of acute CB2 blockade (Aso et al., 2013; Correa et al., 2005), but they are strongly dependent on the selectivity/specificity of the pharmacological compound, and the study of long-term effect is challenging. Thus, it is essential to compare the results of constitutive lack and acute pharmacological blockade of CB2 on microglial activation to validate results from one model and increase confidence in the results obtained.

Table 1.1: List of synthetic CB2 agonists/antagonists

CB2 ligands	Compound	Ki	Other TRP and receptor targets	Selectivity for mCB2
Agonists	JWH-133	3.4 nM	TRPV1	40
	AM1241(R,S)	3.4 nM	TRPA1	17
	JWH-015	13.8 nM	_	5
	HU308	22.7 nM	_	12
	GP-1a	0.037 nM	_	20
	HU210	0.061-0.52 nM	CB1, GPR55, 5-HT_2	2
	CP55940	0.6-5.0 nM	CB1, GPR55	3
	WIN55212-2	62.3 nM	CB1, TRPA1	0.3
Antagonists	SR144528	0.6 nM	_	6026
	AM630	31.2 nM	TRPA1	115

TRP: Transient receptor potential ion channel –: no other known target apart from CB2

Ki: Inhibitory constant (required concentration to bring about 50 % of maximum inhibition)

Ki: Dissociation constant that indicates the binding affinity of a compound to the receptor. It can also represent the concentration required to occupy 50 % of receptors.

The calculation for CB2 selectivity by (Soethoudt et al., 2017) = 10^(pKi CB2 - pKi CB1). Adapted and modified version of (Soethoudt et al., 2017; Turcotte et al., 2016).

1.9 CB2 in neuroinflammation

CB2 is primarily found in immune cells, including microglia, so its plausible role in immune response and neuroinflammatory processes has been widely studied. CB2 expression has been shown to increase in microglia, astrocytes and other immune cells during neuroinflammation/ neurodegeneration (C Benito et al., 2008; Carlisle et al., 2002; Cristina Benito et al., 2003; López et al., 2018) and its activation has been demonstrated to promote a less inflammatory state *in vivo* and *in vitro* (Vuic et al., 2022). In transgenic APP 2576 mice, CB2 activation with JWH-133 was shown to reduce TNF-α levels and decreased activated microglia with improved cognition (Martín-Moreno et al., 2012), while in AβPP/PS1 mice model, JWH-133 similarly lowered inflammatory cytokine expression and microglia reactivity (Aso et al., 2013). Moreover, another CB2 agonist, 0-1966 reduced activated microglia number and boosted motor function in a traumatic brain injury model (Elliott et al., 2011). In *in vitro* studies, CB2 agonist JWH-015 increased Aβ clearance in human macrophage cell lines (Tolón et al., 2009). More so, CB2 activation with AEA lowered cytokine levels in myeloid dendritic cells from multiple sclerosis patients (Chiurchiù et al., 2013). One of the suggested mechanisms for CB2-mediated immune suppression is associated with MAPK pathways. For example, CB2 activation with AEA increased anti-inflammatory cytokine IL-10 secretion via JNK and ERK1/2 pathway during inflammatory stimulation (Correa et al., 2010). In short, these findings support that CB2 activation has anti-inflammatory effects in microglia and other immune cells and could have potential therapeutic effects in neuroinflammatory conditions.

Somewhat contradictory to these findings, $CB2^{-/-}$ mice also produced anti-inflammatory effects. For instance, CB2 deletion in an Alzheimer's disease mouse model (APP/PS1) resulted in improved cognition and lower inflammatory responses (Schmöle et al., 2018). Additionally, the morphology of plaque-associated microglia in APP/PS1*$CB2^{-/-}$ mice indicated that they were less activated compared to APP/PS1 control mice (Schmöle et al., 2018).

Given the surprising similarities between CB2 activation and CB2 deletion models, it becomes even more apparent that validation of $CB2^{-/-}$ results with CB2 pharmacological antagonist is necessary to increase the degree of confidence in these results as well as proper interpretation.

1.10 CB2 and TLR signaling crosstalk: Influence on microglial activation

The interaction between CB2 and TLRs has been discussed for years. Both CB2 and TLRs are found in immune cells and have known immune regulatory functions (schematic representation in **Figure 1.6**). Many studies that investigated the interplay between CB2 and TLR signaling showed mostly anti-inflammatory, but also pro-inflammatory effects of CB2 activation in TLR stimulated microglia, macrophages and dendritic cells. To begin with, activation of CB2 with JWH-133 increased anti-inflammatory IL-10 production in macrophages upon TLR4 stimulation with LPS (Correa et al., 2005). A different CB2 agonist AM1241 also suppressed inflammatory responses to LPS/IFN-γ in N9 microglial cells (Ma et al., 2015). Furthermore, AEA and WIN55212-2 decreased the activity of inducible nitric oxide synthase (iNOS) in TLR4-stimulated microglia (Eljaschewitsch et al., 2006).

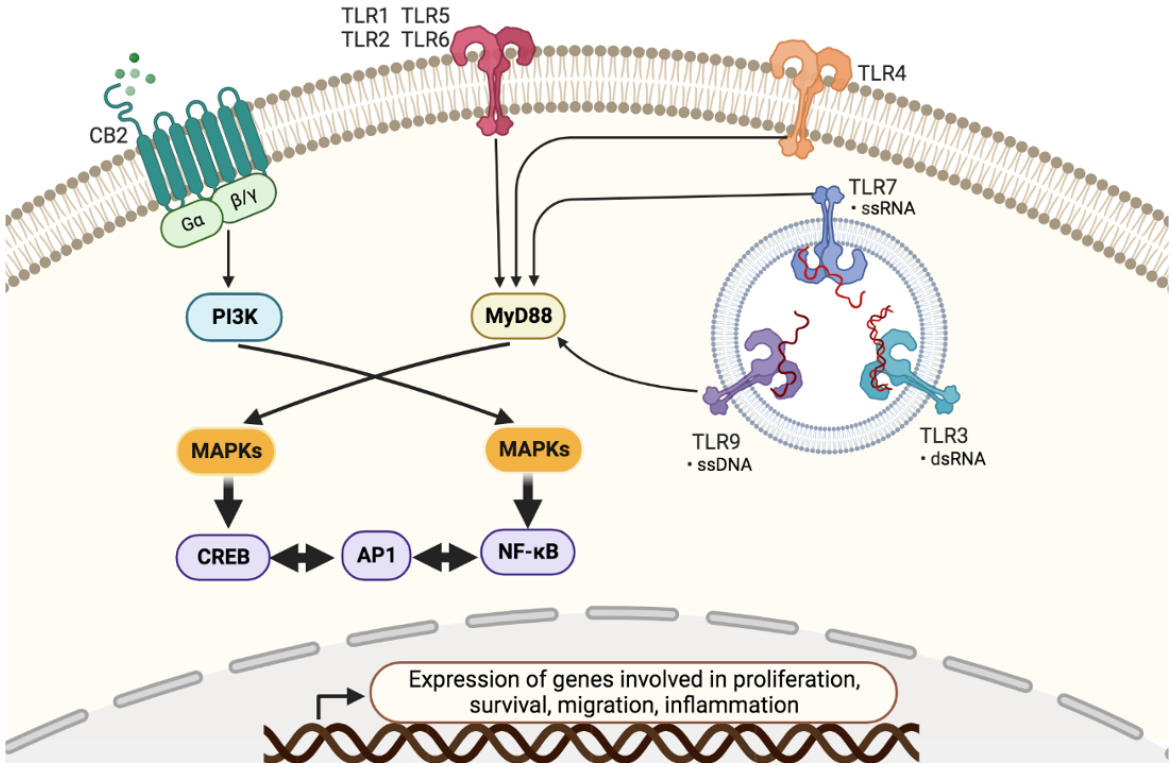

Figure 1.6: Interplay between CB2 and TLR signaling. CB2 activation causes phosphatidylinositol-3-kinase (PI3K) to activate a cascade of intracellular events involving mitogen-activated protein kinases (MAPKs) and transcription factors like activator protein 1 (AP1), cAMP-response element binding protein (CREB) and nuclear factor kappa light chain enhancer of activated B cells (NF-κB). Interestingly, TLR signaling also activates MAPKs and the transcription factors CREB, AP1 and NF-κB downstream of MyD88. Hence, these two pathways were hypothesized to interact at the point of convergence, thereby regulating one another. Modified from (Badal et al., 2017; Mccoy, 2016).

Based on the previous results from our lab, $CB2^{-/-}$ also exhibited dampened inflammatory effects in microglia upon TLR stimulation. Decreased inflammatory cytokines (TNF-α, IL-6 and CCL2) and reduced inflammatory surface markers (ICAM-1 and CD40) were observed in $CB2^{-/-}$ microglia compared to the WT after TLR4 stimulation with LPS/IFN-γ (Schmöle, Lundt, Ternes, et al., 2015). In alignment with these results, our transcriptional profiling data further revealed that $CB2^{-/-}$ microglia have an attenuated TLR-induced gene activation profile compared to the WT. Furthermore, it was demonstrated that $CB2^{-/-}$ microglia showed less activated microglial morphology after TLR3 and TLR4 stimulation in organotypic hippocampal slice cultures (OHSCs). Despite these findings, the molecular mechanism of the dampened phenotype in $CB2^{-/-}$ remains unclear. Moreover, validation of $CB2^{-/-}$ data with the CB2 antagonist is still missing.

1.11 Aim of the project

This project builds upon the previous research conducted in our lab, where it was demonstrated that primary microglia from $CB2^{-/-}$ mice had lower inflammatory responses to LPS/IFN-γ stimulation (Schmöle et al., 2015), but this finding is limited to only TLR4 stimulation as effects from other TLRs are missing. It was further shown that CB2 deletion had beneficial impact on cognition in APP/PS1 mouse model of AD; however, the molecular mechanism is missing (Schmöle, et al., 2015; Schmöle et al., 2018). Moreover, it was reported that the anti-inflammatory effect of CB2 deletion on microglial activation is also present but less pronounced in other myeloid cells outside the CNS. However, these studies lack validation from pharmacological models using CB2 antagonists. The current project is aimed to deepen our understanding of CB2's influence on TLR-mediated microglial activation by answering the following crucial questions:

- Does CB2 deletion modulate inflammatory profile in primary microglia after TLR3, TLR4 and TLR9 activation?
- What is the molecular mechanism by which CB2 deletion suppresses TLR-mediated microglial activation?
- Does CB2 receptor act along the metabolic-inflammatory axis to modulate TLR4-induced microglial activation?
- Does pharmacological inhibition of CB2 mimic the effects observed in CB2 constitutive knockout with respect to TLR-induced microglial activation?

2. Materials and Methods

2.1 Devices and equipment

Device	Identifier or company
Analytical balance	Sartorius BP 2100, Elk Grove, IL, USA
Autoclave	Laboklav 55-195, Germany
CCD camera	Axiocam MRm, Zeiss, Jena, Germany
Centrifuges	Biofuge fresco, Heraeus, Thermo Scientific, Germany Multifuge 3SR, Heraeus and Kendro, Germany Megafuge 16R, Heraeus, ThermoFisher, Germany
Confocal microscope	TCS SP8, Leica
Electrophoresis chamber	Sub-Cell GT System, Bio-Rad Laboratories, Germany
Flow cytometer	FACS-Canto II, BD Bioscience, Heidelberg, Germany
Freezers	Hera freeze HFU B series, Thermo Scientific (-80 ˚C) Liebherr (-20 ˚C)
Gel imaging system	ChemiDoc MP, Bio-Rad laboratories GmbH, Germany
Hemocytometer	Neubauer counting chamber, CarlRoth, Germany
Ice machine	CoolNat 186792, Ziegra, Germany
Incubators	Cell culture incubator, Binder GmbH Common bench incubator, biometra OV 5, USA
Laminar flow hood	Herasafe, Kendro
Liquid nitrogen flask	Chart Industries, Inc, Germany
Magnetic stirrer	MR3001, Heidolph, Germany
Microplate reader	MRX TC II, Dynex Technologies, USA
Microscopes	ApoTome2, Zeiss, Jena, Germany, Nikon Eclipse TS100, Japan, Carl Zeiss microimaging, Geta
Microwave	Severin 800, Germany
Mini centrifuge	Galaxy mini centrifuge, Merck eurolab
Oven	Varioklav 25T, H+P Labortechnik
pH meter	Inolab, WTW

Seahorse XFe96 analyzer	Agilent Technologies
Shaker	Edmund Bühler GmbH, Germany
Thermocycler	Thermal Cycler Tc100, Bio-Rad
Thermomixer	Eppendorf AG, Hamburg, Germany
Tissue culture hood	HERsafe, Thermo Scientific, Germany
Vibratome	Lecia VT 1200S
Vortexer	Vortex-Genie 2, Scientific Industries, USA
Water bath	GFL 1002, Gesellschaft für Labortechnik mbH, Germany
WES machine	Proteinsimple, a biotechne brand, USA
XFe96 Analyzer	Agilent Technologies, 102601-100 USA

2.2 Chemicals/reagents

Chemicals/reagents	**Company (Catalog number)**
100 bp DNA ladder	Life Technologies (15628-050)
2-Mercaptoethanol	Gibco(31350-010)
2-Propanol/isopropanol	Carl Roth (6752.4)
4',6-diamidino-2-phenylindole (DAPI)	Sigma-Aldrich (10236276001)
Agarose	Carl Roth (2267.4)
Antibody diluent for WES	Proteinsimple (042-203)
Bovine serum albumin (BSA)	PAN-Biotech (P06-1391500)
Citric acid	Promega (H526a)
CpG	Metabion (CpG1668)
Deoxycholate	Applichem (A1694,0250)
dNTP mix (10 mM)	Sigma-Aldrich (D7295)
DTT, dithiothreitol for WES (EZ standard pack)	Proteinsimple (PS-ST01EZ)
Dulbecco's Modified Eagle Medium (DMEM)+Glutamax, 4.5 g/L glucose	Gibco (61965-026)
Ethanol (EtOH) absolute	VWR (20821.330)
Ethidium bromide (EtBr) solution (10 mg/ml)	Sigma-Aldrich (E1510)
Ethylenediaminetetraacetic acid (EDTA), disodium salt	Calbiochem (324503)

Ethylene glycol	Sigma-Aldrich (102466)
Fetal bovine serum (FBS)	PAA (A15-108)
Fluoromount-G®	SouthernBiotech (0100-01)
Hanks' Balanced Salt Solution (HBSS)	Gibco (24020-091, 14175-053)
HEPES	Gibco (15630-056)
Horse serum	Gibco (26050-088)
Hydrochloric acid (HCl) 37 %	Carl Roth (X942.1)
Interferon-gamma (IFN-γ)	R&D systems (485 MI)
JWH-133	Tocris (1343)
L-glutamine 200 mM (100x)	Gibco (25030-024)
Lipopolysaccharide (LPS)	Sigma-Aldrich (L4516)
Luminol S	Proteinsimple (043-311)
MilliQ Ultrapure water	Millipore (CDUFBI001)
Minimum essential medium (MEM)	Gibco (11090-081)
Nonidet* P40 (NP 40)	Applichem (A1694,0250)
Normal goat serum (NGS)	Abcam (ab7481)
Paraformaldehyde (PFA)	Sigma-Aldrich (P6148)
Penicillin-Streptomycin (10,000 U/mL)	Gibco (15140-122)
Peroxide for WES	Proteinsimple (043-379)
Phosphatase inhibitor	Thermo scientific (A32957)
Phosphate-buffered saline (PBS) tablets	Gibco (18912014)
Phosphoric acid (H_3PO_4)	Sigma (43.808)
Polyinosinic-polycytidylic acid (Poly I:C)	Sigma (P0913)
Poly-L-lysine	Sigma (P1524)
Protease inhibitor mini (EDTA-free)	Thermo scientific (A32955)
Proteinase K	NEB (P8107S)
RPMI medium 1640	Gibco (21875-034)
Seahorse XF assay medium (RPMI)	Agilent Technologies (103576100)
Seahorse XF calibrant solution	Agilent Technologies (100840000)
Sodium azide (Na-azide)	Sigma-Aldrich (S8032)
Sodium chloride (NaCl)	Carl Roth (9265)

Sodium dodecyl sulphate (SDS)	Carl Roth (2326)
SR144528 (5 mg)	Sigma-Aldrich (SML1899)
Streptavidin HRP	Proteinsimple (042-414)
Taq Polymerase (10x ThermoPol buffer)	NEB (M0267X)
Tris-(hydroxymethyl) aminomethane (Tris-base)	Carl Roth (5429)
Tris-HCl	Carl Roth (9090.3)
Triton™ X-100	Sigma-Aldrich (T9284)
Trypsin-EDTA (1 X)	Gibco (25200-056)
TWEEN® 20	Sigma-Aldrich (P9416)
UltraPure™ agarose	Invitrogen (15510-027)
WES EZ standard pack 1 for 5 x master mix	Proteinsimple (PS-ST01EZ)
WES 10x sample buffer	Proteinsimple (042-195)
XF flux pak reagents	Agilent Technologies (102601-100)

2.3 List of drugs and stimulants

Stimulant	Concentration/Dilution	Company
CpG	1 nmol/mL	Metabion (CpG1668)
DMSO	0.1 nM	Applichem (A3672,0250)
IFN-γ	20 ng/mL	R &D system (485 MI)
JWH 133	100 nM, 1 μM	Tocris (1343)
LPS	100 ng/mL	Sigma-Aldrich (L4516)
PolyI:C	50 μg/mL	Sigma (P0913)
SR144528	1 nM - 1 μM	Sigma-Aldrich (SML1899)

2.4 Antibodies

Antibody type	Antibody specification	Company (catalog no)
Primary antibody	Rabbit anti-mouse Iba1	Wako (019-19741)
	Rat anti-mouse CD68	Bio-Rad (MCA1957)
Secondary antibody	Goat Alexa fluor 488 anti-rat	Life Technologies (A11006)
	Goat Alexa fluor 647 anti-rabbit	Life Technologies (A21245)

2.5 Consumables

Item	Specifications	Company (ref #)
Cell culture flasks	75 cm^2 with red filter cap	Cell star (658175)
Cell culture plates	24 well plates 12 well plates 6 well plates	Greiner bio-one (662 160) Greiner bio-one (665 180) Falcon (353046)
Cell scraper	18 cm handle/1.8cm blade	BD falcon (353085)
Cell strainers	70 μm nylon 100 μm nylon	Falcon (352350) Corning (431752)
Centrifugal filters	Amicon ultra 0.5 mL	Merck (UFC510096)
Chamber slides	8 well glass slides	Lab-Tek (154534)
Disposable bags	Autoclavable	Brand (7597 05)
Disposable scalpel	No. 10 pfm steel blade	Feather (02.001.30.010)
Eppendorfs for ELISA	2.5 mL purity grade 5 mL purity grade 10 mL purity grade	Biopur (G175527R) Biopur (K197280L) Biopur (K200472O)
Falcon tubes	15 mL, conical bottom 50 mL, conical bottom	Greiner bio-one (188 271) Greiner bio-one (227 261)
Microscope slides	Superfrost™ Plus 25x75x1 mm	Epredia (J1800AMNZ) Gerhard Menzel GmbH
Microscope cover glasses	High precision 24x60 mm 175+/-5 μM, No. 1.5 H	Paul Marienfeld GmbH & Co. KG (0107242)
Millipore cell culture inserts	0.4 μM, 30mm diameter	Merck (PICMORG50)
Needle	27 G1/2 0,4x13 mm	BD Microlance (300635)
Nunc ELISA plates	Nunc Maxisop 96 well	Thermo Scientific
Parafilm	4 inches x 125 ft roll	Parafilm Bemis (PM-996)
Petri dishes	60 x 15 mm style 100 x 20 mm style	BD Falcon (351016)
Pipettes	5 mL serological pipette 10 mL serological pipette 25 mL serological pipette	Costar (4487) Costar (4489) Sarstedt (86.1256.001)

	50 mL serological pipette	
Rapid flow filter unit	75 mm filter unit -500 mL 50 mm filter unit -250 mL	Thermo Sc. (156-4020) Thermo Sc. (157-0020)
Reagent reservoir	100 mL	Thermo scientific (8086)
Scalpel	No. 10 pfm steel blade	Feather (02.001.30.010)
Seahorse Agilent plates	96 well plates	Agilent (100777.004)
Seahorse XFe96 FluxPaks	Mini pack	Agilent (102601-100)
Seal plates	ELISA seal plates	Excel sc., inc (SM-KIT-SP*)
Syringe	10 mL	BD Discardit II
Tissue culture dish	100 x 20 mm style	Falcon, Corning (353003)
WES plates	25 well microplates	proteinsimple (SM W004)

2.6 Solutions/buffer

Method used for	**Solutions/Buffer**	**Composition**
Genotyping	Lysis buffer	MilliQ H_2O
		100 mM Tris/HCl pH = 8.0
		5 mM EDTA
		200 mM NaCl
		0.2 % (w/v) SDS
		Proteinase K (1mg/ml)
	Tris acetate-EDTA (TAE) buffer	MilliQ H_2O
		40 mM Tris-acetate
		1 mM EDTA pH = 8.0
	Tris-EDTA (TE) buffer, pH = 7.4	MilliQ H_2O
		10 mM Tris-HCl
		1 mM EDTA pH = 8.0
	EtBr solution	TAE buffer
		1.5 μg/mL EtBr
Cell culture media	Primary microglia culture medium	DMEM glutamax (4.5 g/L glc)
		10 % FCS (heat inactivated)

		1 % pen step
		20 % M-CSF (when applicable)
	Organotypic hippocampal slice culture medium	Minimum essential medium
		25 % horse serum
		25 % HBSS
		4.5 % glucose
		1 % L-glutamine
		1 % pen strep
		1 % amphotericin B
	Organotypic hippocampal slice dissection medium	Minimum essential medium
		1 % L-glutamine
		1 % HEPES
		1 % pen strep
	Bone marrow-derived macrophages	RPMI 1640
		15 % M-CSF (preconditioned)
		10 % FCS (heat inactivated)
		1 % pen strep
		0.1 % 2-mercaptoethanol
		0.5 mL reagent B (4 % cupric sulfate)
Flow cytometry	PBS 1 x (pH = 7.4)	500 mL MilliQ H_2O
		1 PBS tablet
	FACS buffer	PBS 1x
		2 % FCS (heat inactivated)
ELISA	ELISA wash buffer	PBS 1x
		0.05 % Tween-20
	ELISA stop solution	1 M H_3PO_4
Protein analysis	RIPA buffer (radioimmuno precipitation assay)	10 mM Tris (pH = 8.0)
		150 mM NaCl
		5 mM EDTA (pH = 8.0)
		1 % deoxycholate

		1 % NP-40 (Igepal CA630)
		0.1 % SDS
		Fill up with MilliQ H_2O
	BCA protein assay (Working reagent, WR)	24.5 mL reagent A (composed of sodium carbonate, sodium bicarbonate, sodium tartrate, and bicinchoninic acid in 0.1 M sodium hydroxide
		0.5 mL reagent B (4 % cupric sulfate)
	Automated Western blot (WES 10 x sample buffer)	Ready to use (proteinsimple, 042-195), SM-W001
	Master mix solution	400 mM DTT + sample buffer
Immunohistochemistry/ Immunocytochemistry (Iba1 and CD68)	4 % PFA (paraformaldehyde)	PBS 1x
		4 % PFA (w/v) filtered
	Preservative solution	PBS
		0.1 % Na-azide
	PBS-T (0.1 %)	0.1 % Triton X 100 in PBS
	PBS-T (0.25 %)	0.25 % Triton X 100 in PBS
	PBS-T (0.5 %)	0.5 % Triton X 100 in PBS
	Permeabilization solutions	PBS-T 0.1 % (pry microglia)
		PBS-T 0.5 % +0.1 % Na-azide (OHSCs)
	Blocking solution (primary microglia)	PBS-T 0.1 %
		5 % NGS
		3 % BSA
	Blocking solution (OHSCs)	PBS-T 0.5 %
		10 % NGS
		0.1 % Na-azide
	Antibody solution (OHSCs)	PBS-T 0.25 %
		2.5 % NGS

		0.1 % Na-azide
Seahorse metabolic analysis	Seahorse culture medium	DMEM+Glutamax
	Assay compounds/electron tranport chain inhibitors	10 mM Glucose
		1 μM oligomycin
		2 μM FCCP
		0.5/2.5 μM Antimycin/rotenone
	XF Cartridge calibrant	Seahorse assay calibrant
	Seahorse XF assay medium	RPMI without phenol red, glucose, pyruvate, glutamine (Agilent, 103576-100)

2.7 Mice

The mice used in this study were C57BL/6J wild type (WT) and B6.cgCnr2tm1Zim (constitutive CB2 knockout, $CB2^{-/-}$) mice. C57BL/6J, originally procured from a commercial breeder (Charles River) were bred in-house at the University of Bonn animal facility. The B6.cgCnr2tm1Zim ($CB2^{-/-}$) mice were generated by Buckley and colleagues (Buckley et al., 2000) using homologous recombination to replace the 3' region of the CB2 gene (*Cnr2*) coding exon 3 with phosphoglycerate kinase PGK - neomycin sequence in embryonic stem cells. This mutation led to the deletion of 131 amino acids at the Carboxyl-terminal of CB2 receptor, thereby losing part of intracellular loop 3 as well as transmembrane domains 6 and 7. To reduce the risk of genetic drift, the $CB2^{-/-}$ mice were homozygously bred and backcrossed to C57BL/6J strain every six generations.

The two mouse lines were kept under specific pathogen-free conditions with *ad libitum* access to food and water under 12 hr light/dark cycle in the University of Bonn animal facility. Mice were group-housed after weaning in standard laboratory cages equipped with an automatic ventilation system (maximum of 5 animals per cage). Cages were monitored daily, and bedding, food and water were changed weekly. Animal care and experimentation with organ retrieval followed the guidelines of the European Communities Directive 86/609/EEC and the German Animal Protection Law regulating animal research and were approved by the LANUV NRW, Germany (01_Organentnahme).

2.7.1 Experimental groups

The experimental groups consisted of mixed-gender WT and $CB2^{-/-}$ mice of different ages. Pups between p1 - p4 were used for primary microglia cell culture while p4 - p6 were used for organotypic hippocampal slice cultures (OHSCs). As for bone marrow-derived macrophages (BMDMs), adult mice between the age of 3 - 6 months were used. At least 3 independent preparations (N = 3 – 8 replicates) were performed for microglia experiments, 2 - 3 independent preparations for OHSCs experiments (N = 3) and 2 independent preparations (N = 3 - 5) for BMDMs experiments.

2.8 Genotyping

2.8.1 DNA isolation

Immediately after weaning, mouse tail biopsies (2 - 3 mm) were taken from 3 weeks old mice. The tails were dissolved in 200 μL of lysis buffer (see section **2.6**), which contained 3 μL of freshly added proteinase K (1 mg/mL). The mixture was then incubated overnight at 55 °C with slow shaking (550 rpm). The following day, samples were spun down at 13000 x g for 10 min at 4 °C to remove any pieces of unlysed tissue, after which the supernatant was transferred to a brand-new eppendorf tube. Isopropanol (200 μL) was added as a precipitant and the tube was gently inverted many times. The precipitated samples were spun down again and the resulting DNA (deoxyribonucleic acid) pellet was washed two times with 500 μL 70 % ethanol and left to air dry for 20 min. Finally, the dried DNA pellet was re-dissolved in 100 μL of TE buffer, and the resulting DNA sample was kept at 4 °C.

2.8.2 DNA amplification by polymerase chain reaction

Polymerase chain reaction (PCR) was used to amplify specific DNA fragments of interest from the isolated DNA. The three-step process of PCR include denaturation, annealing and elongation, which occur at different peculiar temperatures. Details of the PCR components and the reaction conditions are listed below. In a PCR tube, the PCR components milliQ water, thermoPol buffer, deoxyribose nucleoside triphosphates (dNTPs), primers, Taq polymerase and DNA were mixed in adequate quantities to PCR tubes after which they were carefully placed in the thermocycler for the PCR reaction.

PCR reaction for genotyping ($CB2^{-/-}$ mice)	
39 μL	MilliQ water
5 μL	10x ThermoPol buffer
1 μL	dNTP mix (10 mM)
1 μL	Primer WT: 5´-GTG CTG GGC AGC AGA GCG AAT C -3´
1 μL	Primer KO: 5´-AGC GCA TGC TCC AGA CTG CCT -3´
1 μL	Primer COM: 5'-GTC GAC TCC AAC GCT ATC TTC -3'
1 μL	Taq Polymerase
1 μL	DNA sample (around 100 ng/μL)

	PCR program	Temperature	Time
1x	**Initial denaturation**	**95 °C**	**2 min**
	Denaturation	95 °C	30 s
35 x	Annealing	60 °C	60 s
	Elongation	68 °C	45 s
1 x	Final elongation	68 °C	7 min
	Cooling	4 °C	∞

2.8.3 Gel electrophoresis

A 2 % agarose gel was prepared in TAE buffer and gently poured into the electrophoretic tray (with desired comb inserted) to solidify at room temperature. The hardened gel was transferred into TAE buffer-filled electrophoresis chamber, after which the PCR product (10 - 20 μL) mixed with 10 x loading dye (2 μL) was carefully loaded into each well. The first well contained only DNA ladder (100 bp, 5 μL) to allow for size estimation of the PCR products. Electrophoresis was run for 60 - 80 min at 120 V. Once the electrophoresis run was complete, gels were immersed into the ethidium bromide bath solution for about 15 min and bands were viewed with the aid of ChemiDoc MP imaging system (Bio-Rad Laboratories). The expected band size for WT and $CB2^{-/-}$ mice are 639 and 400 bp respectively.

2.9 Cell culture experiments

2.9.1 Primary neonatal microglia culture

Primary neonatal microglia were prepared using WT and $CB2^{-/-}$ pups between p1 to p4. Brains were extracted from decapitated pups and placed in ice-cold HBSS (Hanks' balanced salt solution). The brains were split into two hemispheres and meninges and midbrains were carefully removed. The resulting cortices were dissociated by gentle pipette resuspension to obtain a single-cell suspension and filtered through a 70 μm cell strainer. The cells were centrifuged for 10 min at 300 x g and the supernatant was discarded; the resulting pellets were cultivated in the microglia culture medium with or without M-CSF (**Table 2.1**). Cortices from pups of the same genotype were cultivated in either a 10 cm tissue culture dish or a poly-L-lysine coated T 75 cell culture flask in an incubator set at 5 % CO_2 and 37 °C (**Table 2.1**). The medium was changed the following day and twice weekly for those cultivated without M-CSF in tissue culture dishes for approximately 2 weeks or more. Whereas medium change for microglia cultured in T 75 flasks with M-CSF occurred every other day for 10 days or until the mixed glial culture reached confluency (usually wait till 14 days). For harvesting and reseeding microglia, loosely attached monolayer of mature microglia (about 80 – 90 % confluency) were shaken off the astrocytes' bottom layer at 37 °C for 1 hr at 200 rpm. Harvested microglia were either reseeded in 12/ 24 well plates or 8 well chamber slides overnight at 1.5 x 10^5 cells/mL density in each well containing a pre-warmed medium. The cells were left to sadhere to the plate till the next day when they were used for stimulation experiments.

Table 2.1: Different microglia protocols and media components

Primary microglia protocol	Medium components	Amount
Protocol I (10 cm tissue culture dishes)	DMEM + Glutamax	500 mL
	FCS	50 mL
	Pen/Strep	5 mL
Protocol II (PLL coated T 75 flasks)	DMEM + Glutamax	150 mL
	FCS	15 mL
	Pen/Strep	1.5 mL
	M-CSF (preconditioned)	30 mL

2.9.2 Organotypic hippocampal slice culture preparation

Organotypic hippocampal slice cultures (OHSCs) were generated from WT and $CB2^{-/-}$ pups between p4 - p6. Brains were carefully removed from decapitated pups and transferred into ice-cold dissection medium in petri dishes (**Table 2.2**). The cerebella were detached and discarded. The resulting cerebra from 2 - 3 brains were super-glued to the vibratome platform (dorsal part facing up) with a 2 % agarose block. The glued brains were subsequently transferred into the dissection medium, pre-poured in the vibratome tray for sectioning. 350 μm thick hippocampal slices were sectioned horizontally by the vibratome at a speed of 0.6, after which the slices were immediately immersed into a fresh ice-cold dissection medium pre-poured in the petri dishes. The intact hippocampi, with a clear view of the CA1, CA2, CA3, dentate gyrus, and the entorhinal cortex regions, were carefully dissected out from the slices using a scalpel under the dissecting microscope. The unscathed hippocampal slices were moved into freshly prepared dissection medium in new petri dishes and carefully transferred onto millipore semi-porous membrane inserts (2 - 3 slices per insert under the hood). The inserts containing the slices were placed in 6 well plates filled with 1 mL culture medium (**Table 2.3**) and cultured for 14 days at 5 % CO_2 and 37 °C. Medium change occurred every other day. On day 14, only the healthy-looking slices with flattened transparent features were used for stimulation experiments.

Table 2.2: OHSCs dissection medium composition

Components	Volume
MEM	400 mL
L-Glutamine (200 mM)	4 mL
HEPES	4 mL
Pen/Strep	4 mL

Table 2.3: OHSCs culture medium composition

Components	Volume
MEM	100 mL
Horse serum	50 mL
HBSS	50 mL
L-Glutamine (200 mM)	2 mL
Pen/Strep	2 mL
Amphotericin B	2 mL
D-Glucose (45 %)	2 mL

2.9.3 Bone marrow-derived macrophages

Bone marrow-derived macrophages (BMDMs) were generated from adult mice (3 - 6 months old). Two to three mixed-gender WT and $CB2^{-/-}$ mice were sacrificed by cervical dislocation and about 40 % of the skin was excised from their hind limbs. The tibia and femur were carefully dissected out, after which a scalpel was used to remove the remaining skin tissue. The skin-stripped femur and tibia were placed in ice-cold PBS pre-poured in a 10 cm petri dish until the remaining femurs and tibias from both genotypes were isolated. Moving to a sterile condition under the cell culture hood, the bone joints were cut open and bone marrow was flushed out into a brand-new petri dish containing ice-cold PBS using a 10 mL syringe. Bone marrows from 2 – 3 mice from the same genotype were pulled together and resuspended in ice-cold PBS until a single-cell suspension was reached. The resuspended cells were sieved via a 100 μm cell strainer and spun down at 1500 rpm for 10 min at 4 °C. After decanting supernatant, the cell pellet was resuspended in culture medium (10 mL) (**Table 2.4**) and cells were counted using hemocytometer. The cell number was adjusted to 1.5 x 10^5 cells/mL, followed by cell resuspension in culture medium (10 mL). Finally, the cells were seeded in 10 cm petri dishes and cultured at 37 °C and 5 % CO_2 for 6 - 7 days. On day 3 of the BMDMs culture, the cells were supplemented with additional 5 mL of fresh medium, making a total of 15 mL that was incubated until day 7. On the 6th or 7th day, cells were harvested by scraping and reseeded in 12 well plates (1.5 x 10^5 cells/mL) for stimulation experiments.

Table 2.4: BMDMs culture medium composition

Components	Amount (Volume)
RPMI 1640	200 mL
M-CSF	30 mL
FCS	20 mL
Pen/Strep	2 mL
β-Mercaptoethanol	0.2 mL

2.10 Stimulation of cultured cells

For genetic knockout studies, reseeded microglia (protocol I) and BMDMs from WT and $CB2^{-/-}$ mice were stimulated with the TLR ligands; LPS (100 ng/mL, TLR4 ligand) and IFN-γ (20 ng/ml), or CpG (1 nmoL/mL, TLR9 ligand) for a duration of 16 hr and or 30 min in the case of protein assays. As for pharmacological studies, WT BMDMs and WT and $CB2^{-/-}$ microglia (protocol II) were used. 15 min before TLR stimulation, re-seeded cells were first pre-treated with the CB2 antagonist, SR144528 (1 nM, 10 nM, 100 nM, 1 μM), after which they were stimulated with the TLR3 or TLR4 ligands above.

It is worth mentioning that we used protocol II for our microglia preparation for the pharmacological part of my project because we optimized our microglial protocol to improve the yield of microglial cells. We first did a pilot microglia preparation using the original protocol I and the new protocol II (see **table 2.1**). We then determined the cell count using a hemocytometer. Interestingly, protocol II produced a significant increase in cell yield (1.2×10^6 per flask) compared to the 3.0×10^5 per plate) produced for protocol. Afterward, we performed a trial ELISA measurement of cytokines to determine cytokine secretion pattern between protocol I and II. We did not observe a significant difference in the pattern of IL-6 release between both protocols. Furthermore, we performed flow cytometry analysis to determine the percentage (%) of live and CD11b+ cells between the two protocols. We found no significant difference in the % of live cells and geometric mean fluorescent intensity (gMFI) of CD11b+ cells between the control groups from both protocols. Therefore, we decided to use protocol II for subsequent experiments due to higher yield and less preparation time.

After stimulation in both cases, supernatants were transferred in a 1.5 mL tube, after which they were shock-frozen in liquid nitrogen and subsequently stored at -80 °C for ELISA. The cells were either lysed for protein analysis, harvested for flow cytometric staining, fixed for immunocytochemistry, or used for seahorse analysis. In the case of OHSCs, slices were stimulated 14 days after culture in the incubator (see **2.9.2**) with the TLR ligands, as mentioned above. Subsequently, hippocampal slices were washed in PBS and fixed for immunohistochemistry. Noteworthy, the slices were randomized at this point to prevent bias during imaging.

2.11 Immunocytochemistry

Stimulated microglia (from section **2.9**) in chamber slides were fixed in 4 % PFA (paraformaldehyde) for 10 min at RT (room temperature). Next, cells were permeabilized with 0.1 % PBS-T for 10 min and then washed thrice in PBS. After that, cells were blocked in blocking solution (see **2.6**) for 1 hr, after which they were incubated with primary antibody (see **Table 2.5**) in antibody solution (ab sln) overnight at 4 °C. The following day, cells were washed three times in 0.1 % PBS-T for 10 min, followed by incubation with secondary antibody (see **Table 2.6**) in ab sln for 1 hr. Afterward, cells were washed two times and stained with DAPI (0.1 μg/mL) at RT for 15 min. After a short PBS wash, the chamber components were carefully lifted from the chamber slides, leaving the slides with the cells intact. The slides were mounted with Flouromount-G® and sealed with coverslips using nail polish, and then kept at 4 °C until imaging. Immunocytochemistry images were obtained using the Leica TCS SP8 confocal microscope at 40x objective. Laser configuration and wavelengths for image acquisition are described in (section **2.14.2**).

Table 2.5: List of primary antibodies used for immunocytochemistry

Antigen	Conjugate	Host	Dilution	Company (Catalog#)
Mouse Iba1	-	Rabbit	1:1000	Wako (019-19741)
Mouse CD68	-	Rat	1:1000	Bio-Rad (MCA1957)

Table 2.6: List of secondary antibodies used for immunocytochemistry

Antigen	Conjugate	Host	Dilution	Company (Catalog#)
Rabbit IgG	Alexa Fluor 647	Goat	1:1000	Thermo Fisher Scientific (A21245)
Rat IgG	Alexa Fluor 488	Goat	1:1000	Thermo Fisher Scientific (A11006)

2.12 Protein analysis

2.12.1 Protein isolation

Microglia cells harvested after stimulation periods 30 min and 16 hr were lysed in 70 – 100 μL of RIPA buffer (see section **2.6**) containing protease and phosphatase inhibitors. The cells were placed on ice for 15 min, then resuspended and scraped into 1.5 mL tubes.

The resulting cell lysates were spun down at 4 °C for 15 min at the maximum speed. The protein content was dispensed into a fresh 1.5 mL tube and concentrated using amicon ultra 0.5 centrifugal filters with 100 kDa cutoff. From the retentate lysates, 5 μL was used for measurement of BCA total protein concentration while the remaining contents were aliquoted in 10 μL per tube and subsequently stored at -80 °C for protein assays.

2.12.2 BCA protein assay

The total protein concentration in the microglia lysates was determined using the Bicinchoninic assay (BCA) assay kit (Thermo Scientific, cat# 23227), adhering to the manufacturer's instructions. Briefly, 5 μL of lysates or BSA standards were incubated in replicates in 96 well plates, after which 200 μL of the working reagent (WR, see section **2.6**) were added. The plate was then placed in an incubator set at 37 °C for 30 min and left to cool at RT. Protein concentration in the protein samples was measured using microplate reader at absorbance wavelength of 562 nm. The protein concentration of the standard was between 25 – 2000 μg/mL. For subsequent WES assay, the sample volume was calculated based on the protein content in each sample.

2.12.3 Automated western blotting by Simple Western™

Western blot analysis was performed using the fully automated simple western system (proteinsimple, 12-230 kDa WES separation module). The simple WES is a gel-free, blot-free size-based immunoassay that takes place in a 25 well capillary. The multi-step process of sample loading, protein separation, immunolabeling, washing and protein detection is fully automated in a single run. Schematic overview of WES is presented in **Figure 2.1**. Assay procedures were carried based on the manufacturer's protocol. Shortly before the assay, lysates were diluted in 0.1 X sample buffer to a final concentration of 0.1 mg/mL. The master mix was then prepared by mixing an equal amount (20 μL) of 10 X sample buffer and 400 mM DTT solution. The samples were added to the master mix in a ratio of 1:4 and denatured for 5 min at 95 °C. The resulting solution was spun down and stored on ice for sample loading. In the 25-well WES microplates, 3 μL of samples and 5 μL of biotinylated ladder were first loaded in the first row of the wells, followed by antibody diluent in the second row. Next, the primary antibody solution was added in the third row (see **Table 2.7**), while HRP-conjugated secondary antibody was dispensed in the fourth,

and finally luminol peroxide mix in the fifth row. The extra bottom wells were filled with wash buffer according to WES protocol. The fully loaded plate was placed in the WES machine containing the inserted cartridge and left to run for approximately 3 hr. The assay WES bands were automatically generated with analyzed data included.

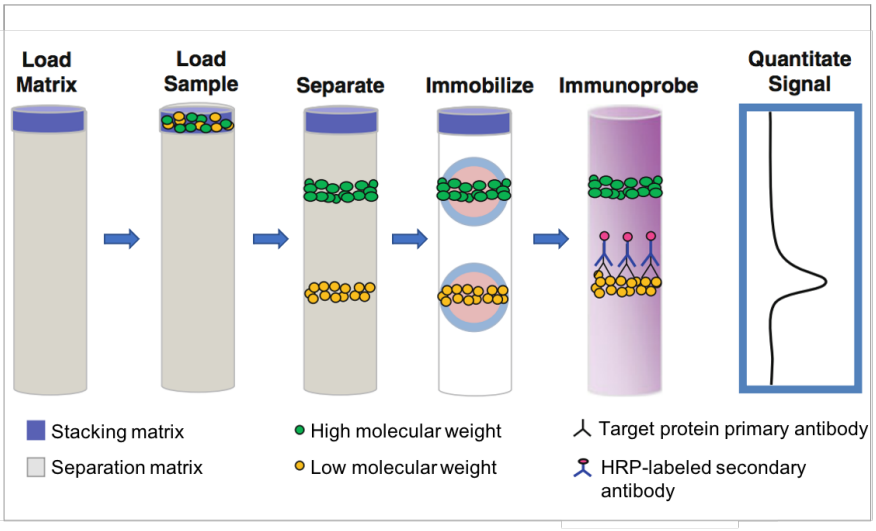

Figure 2.1: Overview of automated WES assay (proteinsimple). The gel free, blot free immunoassay occurs in a capillary, where protein samples are automatically loaded unto the stacking and separation matrix. The proteins are separated based on size and immobilized in a capillary wall. The protein of interest is detected by primary and secondary antibody probing. Assay signal is quantitated with automatic data generation. Adapted from (Harris V.M., 2015).

Table 2.7: List of antibodies used for simple western assay

Antigen	Host	Dilution	Company (Catalog #)
p38 MAPK	Rabbit	1:500	Cell signaling (9212S)
Phospho p38 MAPK (T180/Y182)	Rabbit	1:3	Cell signaling (4511S)
NF-κB p65	Rabbit	1:400	Novus biologicals (sc-372)
Phospho NF-κB p65 (Ser 536)	Rabbit	1:25	Cell signaling (3033S)
ERK1/2	Rabbit	1:400	Cell signaling (4695S)
Phospho ERK1/2 (T202/Y204)	Rabbit	1:5	Cell signaling (9101S)
Akt	Rabbit	1:50	Cell signaling (9272S)
Phospho Akt (Ser 473)	Rabbit	1:15	Cell signaling (9271L)
HRP-conjugated secondary antibody	Rabbit		Proteinsimple (042-206)
β-actin	Rabbit	1:5000, 1:2000	Santa cruz (NB6005322SS)

2.13 Flow cytometry

Flow cytometry or fluorescence-activated cell sorting (FACS) was used to determine cell surface marker expression on microglia. Briefly after supernatant harvest, cells were washed thrice with ice-cold PBS, after which 1 mL of 2 mM EDTA in PBS was added to facilitate the detachment of cells from the well bottom. Next, the cells were incubated on ice for 30 min, gently scraped using a cell scraper and transferred into 1.5 mL fresh tubes. Cells were then centrifuged at 4 °C for 5 min at 300 x g. After decanting the supernatant, cell pellets were gently resuspended in 1 mL FACS buffer and re-centrifuged at 4 °C for 5 min at 300 x g. Next, pellets were incubated in 50 μL blocking solution (Fc-receptor blocker CD16/32 antibody, 1:200 in FACS buffer) for about 10 min on ice. The blocked cells were incubated with 50 μL primary antibody mix containing mouse ((CD11b-Pacific blue, ICAM-1-FITC, CD40-PE, and CD115-PerCP (1:200 each in FACS buffer)) or (CD11b-e450, ICAM-1- FITC, CD40-APC, MHC II-PE and CD45-Bio (1:200 each in FACS buffer))) in the dark for 30 min (**Table 2.8**). The antibody-conjugated cells were stained for live/dead cells with DRAQ7 for 5 min or not.

The stained or unstained DRAQ7 cells were washed with 1 mL FACS buffer and spun down again at 4 °C for 5 min at 300 x g, supernatant discarded. The resulting cells were incubated with or without 45 μL streptavidin bio-tagged secondary antibody PerCP-Cy5.5 (1:200 in FACS buffer) on ice for 15 min in the dark. The cells were finally washed in 1 mL FACS buffer and re-centrifuged as in above. The cells obtained were resuspended in 200 μL FACS buffer and left for flow cytometry measurements. Just before the signal measurement, resuspended cells were sieved through a 40 μM gauze mesh to remove the aggregated cells into the FACS tubes. The signal was measured by the FACS Canto II using the BD FACS Diva software. FACS data were analyzed using the FlowJo software, versions 887 and X 10.0.7r2 (Tree Star Inc).

Table 2.8: List of antibodies used for flow cytometry

Antigen	Host	Conjugate	Dilution	Company	Catalog #
CD16/32	Rat	-	1:200	Biozol	101302
CD11b	Rat	eFluor 450	1:200	eBioscience	48-0112-82
CD11b	Rat	Pac. blue	1:200	BD Bioscience	553310

CD115 (CSF-1R)	Rat	PerCP/Cy5.5	1:200	Biolegend	135526
CD40	Rat	APC	1:200	BioLegend	124611
CD40	Rat	PE	1:200	Biolegend	102805
ICAM-1	Rat	FITC	1:200	eBioscience	11-0541
MHCII	Rat	PE	1:200	BioLegend	107607
MHCII	Rat	APC	1:200	eBioscience	17-5321-82
CD45	Rat	Biotin	1:200	Biozol	103104
Streptavidin		PerCP/Cy5.5	1:200	BD Pharmingen	551419

2.14 Immunohistochemistry, image acquisition and image analysis

2.14.1 Iba1 and CD68 staining

PFA fixed OHSCs (from section **2.10**) were carefully cut out from the millipore membrane inserts and rinsed thrice in ice-cold PBS. The slices were then transferred gently into a 24 well plate (2 slices/well) containing the permeabilization solution (1 mL 0.5 % PBS-T, see **2.6**). The slices were left to permeabilize for 3 days on a tumbler shaker at 4 °C. After three PBS washings at RT, the slices were blocked with blocking solution (0.5 mL 10 % NGS in 0.5 % PBS-T;1:1000 Na azide, see section **2.6**) for 2 days at 4 °C with slow shaking. After that, washing step was repeated and slices were incubated in primary antibody solution (0.5 mL 2.5 % NGS in 0.5 % PBS-T;1:1000 Na azide) for 3 days on a tumbler shaker at 4°C (**Table 2.9**). Negative controls were left unstained without primary antibodies in the solution. The slices were rewashed thrice in PBS, followed by incubation with secondary antibody solution for 2 hr on a slow shaking mode at RT and then on the bench for 3 hr at 4 °C (**Table 2.10**). Afterward, the slices were stained in DAPI (5 μL of 10 μg/mL at 1:100) for 10 min and washed thrice with PBS before mounting onto glass slides using Fluoromount-G®. Finally, the coverslips were tightly sealed with nail polish and slides kept at 4 °C in the dark.

Table 2.9: List of primary antibodies used for immunohistochemistry

Antigen	Conjugate	Host	Dilution	Company (Catalog #)
Mouse Iba1	-	Rabbit	1:1000	Wako (019-19741)
Mouse CD68	-	Rat	1:1000	Bio-Rad (MCA1957)

Table 2.10: List of secondary antibodies used for immunohistochemistry

Antigen	Conjugate	Host	Dilution	Company (Catalog #)
Rabbit IgG	Alexa Fluor 647	Goat	1:1000	Thermo Fisher Scientific (A21245)
Rat IgG	Alexa Fluor 488	Goat	1:1000	Thermo Fisher Scientific (A11006)

2.14.2 Image acquisition by confocal microscopy

Stained slices were imaged using the Leica TCS SP8 confocal microscope with the LAS X software (Leica Application Suite X, 3.5.2.18963). Using the 40x water immersion objective (40 x/1.10 WATER), z stacks of microglia from the CA1 hippocampal region were acquired in 1024 by 1024 pixel size. Specifically, the strata radiatum were imaged (0.5 μm stepsize). The following lasers were used to acquire the images;

DAPI – 405 UV Diode detection at 433-492 nm, Gain 650V)

AF647 - HeNe 633 laser (detection at 658-691 nm, Gain 630V) for the Iba1 channel

AF488 – Argon laser (495-537 nm, Gain 650V) at 20 % power for the CD68 channel

Image analysis was done using ImageJ 1.52i (National Institutes of Health, USA) to add scale bar, color and merge channels.

2.14.3 Microglial morphology analysis using MotiQ (Image J plugin)

3D morphological parameters of microglia were evaluated using the MotiQ plugin designed by Hansen and colleagues (Hansen et al., 2022). The Iba1 channel of the z stacks was used to derive morphological data because Iba1 is a known microglial activation marker. **Figure 2.2** depicts the workflow of how MotiQ analysis operates in 3 components (MotiQ cropper, thresholder, and 3D analyzer). Briefly, ≥ 36 microglial cells/ stimulation/genotype were randomly selected from 2 independent experiments. The chosen cells were cropped from their respective z stacks using the MotiQ cropper. The resulting cropped (single cell images) were thresholded using the MotiQ thresholder (MinError threshold algorithm). The thresholded images were finally analyzed using the MotiQ 3D Analyzer tool (settings: voxel depth= 0.5 μm/voxel, minimum particle volume = 10,000 voxels, length calibration = 0.3608 μm/pixel). A folder with the analyzed results was automatically generated, which included the 3D reconstructed images, skeleton and

the quantified parameters (Iba1 average intensity, branch number, tree length, branch length, ramification index, polarity index, surface, and volume, among others).

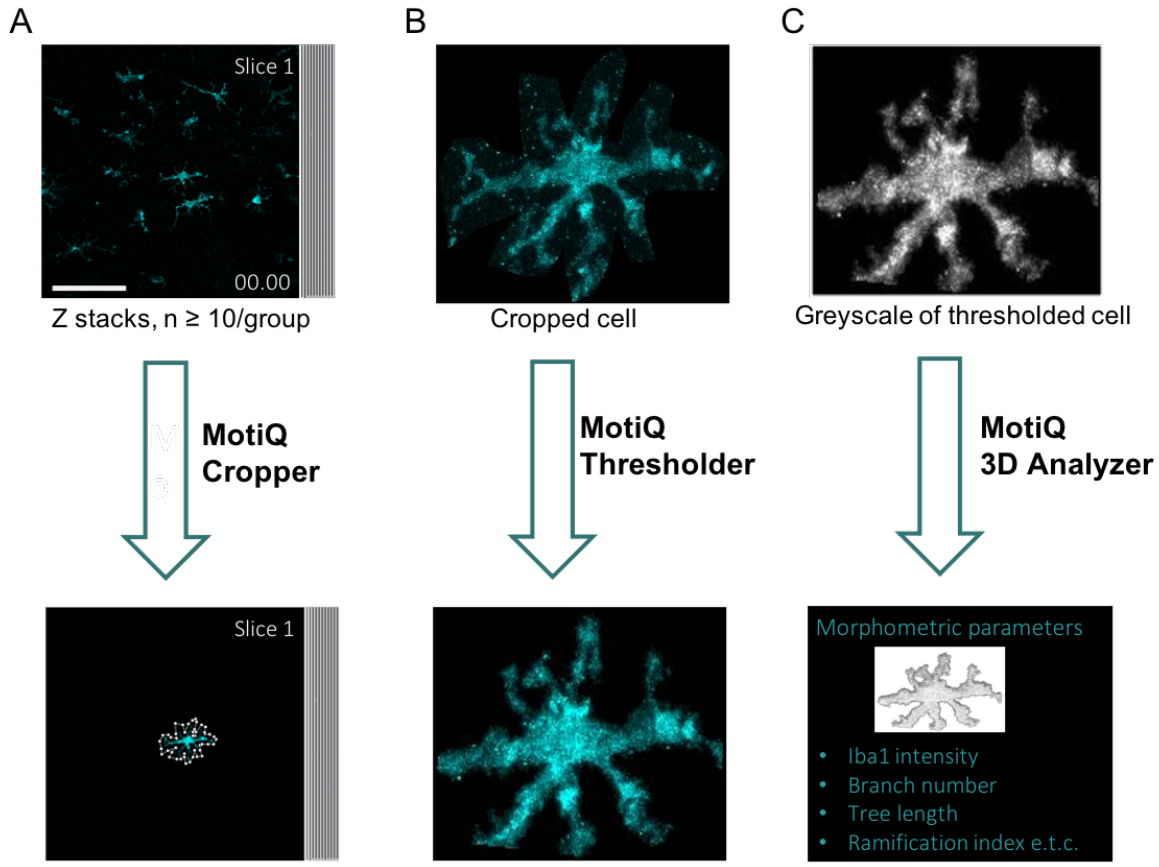

Figure 2.2: Workflow of MotiQ morphology analysis of microglia. (A) Single-cell microglia images were cropped out of the parent z stack using the MotiQ cropper (B) The cropped cells were then thresholded using the MotiQ thresholder. Representative maximum Z projection of a cropped cell is shown. (C) The thresholded images were further analyzed using the MotiQ 3D analyzer to obtain the morphometric parameters such as Iba1 intensity (A.U), branch number (n), tree length (μm), and ramification index (A.U). Other parameters analyzed (but not shown here) include: polarity index (A.U), surface (μm^2), volume (μm^3), and average branch length (μm). Modified version of (Hansen et al., 2022) MotiQ morphology analysis.

2.14.4 Image analysis using ImageJ (CD68 intensities)

Microglial CD68 intensity was measured within the Iba1+ cell in the CA1 pyramidal layer of OHSCs using ImageJ. To begin, microglia (N ≥ 36) from Iba1 channels were manually selected from the maximum Z-projections (Iba1 MAX) and saved as Iba1 ROI. The CD68 maximum Z-projections (CD68 MAX) were in turn, generated from the CD68 channels of the z stacks using the Z project command. The resulting CD68 MAX images were then

thresholded using the threshold command. Finally, CD68 signal intensity (mean gray value, MGV) was measured within Iba1 ROI using the measure command.

The area covered by CD68 (%) was determined in the CA1 pyramidal (pyr) layer of the OHSCs. The CA1 pyr layer was manually delineated based on the DAPI channel and saved as DAPI CA1 ROI. The DAPI CA1 ROI was then applied on the CD68 channel and the area was measured using the measure command. Still within the DAPI CA1 ROI, CD68 images were thresholded using the threshold command and the number/size of CD68 particles were detected using the 'Analyze particle' function. Finally, particle density was derived from the division of the number of cells by the area size.

2.15 ELISA (Enzyme-linked immunosorbent assay)

Cytokine levels in microglia and BMDMs cell culture supernatants were measured using uncoated ELISA kits (Thermo Fisher Scientific, **Table 2.11).** All cytokine measurements and assay procedures followed the manufacturer's protocol (**Tables 2.11 & 2.12**). Briefly, 50 μL capture antibody (1:250 in assay diluent 1x coating buffer) was coated on Nunc MaxiSorp 96-well plates (flat-bottom) and incubated overnight at 4 °C. The next day,4 rounds of washings with 200 μL wash buffer/well (see section **2.6**) was done and the plates were blocked with 100 μL assay diluent at RT for 1 hr. Plates were rewashed thrice and incubated with 50 μL standards (**Table 2.12**), and samples (unstimulated samples were undiluted while stimulated samples were diluted 1:50 in assay diluent) at RT for 2 hr. After washing, the wells were loaded with 50 μL detection antibody (coupled to biotin, 1:250 in assay diluent) and incubated at RT for 1 hr. The plates were washed again and incubated with 50 μL streptavidin-HRP (1:250 in assay diluent) at RT for 30 min in the dark. After a final round of washing, 50 μL TMB substrate solution was dispensed into all wells of the plate and further kept in the dark at RT for 15 min. A blue colour was formed and the reaction was stopped with 25 μL stop solution (1 M H_3PO_4). The plate was read at an absorbance wavelength of 450 nm using Dynex plate reader (Dynex Revelation 4.22 software). The cytokine levels in the samples were automatically interpolated from the standard curve in pg/mL and data statistics were obtained using Prism 9.0.

Table 2.11: ELISA Kit and reagents used for cytokine measurement

ELISA Kit	Capture antibody for coating	Detection antibody	Streptavidin HRP	Substrate solution
TNF-α (ThermoFisher) 88-7324-88	Anti-mouse TNF-α (1:250)	Anti-mouse TNF-α (1:250)	Avidin-HRP (1:250)	1x TMB
IL-6 (ThermoFisher) 88-7064-88	Anti-mouse IL-6 (1:250)	Anti-mouse IL-6 (1:250)	Avidin-HRP (1:250)	1x TMB
CCL2 (ThermoFisher) 88-7391-88	Anti-mouse CCL2 (1:250)	Anti-mouse CCL2 (1:250)	Avidin-HRP (1:250)	1x TMB
IL1β (ThermoFisher) 88-7013-22	Anti-mouse IL-1β (1:250)	Anti-mouse IL-1β (1:250)	Avidin-HRP (1:250)	1x TMB
IL-10 (ThermoFisher) 88-7105-22	Anti-mouse IL-10 (1:250)	Anti-mouse IL-10 (1:250)	Avidin-HRP (1:250)	1x TMB

Table 2.12: ELISA Standards

Cytokine Kit and Catalog #	Standard Concentration
Mouse TNF-α standard (ThermoFisher) 88-7324-88	1000 pg/mL - 7.8 pg/mL
Mouse IL-6 standard (ThermoFisher) 88-7064-88	500 pg/mL - 3.9 pg/mL
Mouse CCL2 standard (ThermoFisher) 88-7064-88	2000 pg/mL - 15.625 pg/mL
Mouse IL-1β standard (ThermoFisher) 88-7064-88	1000 pg/mL - 7.8 pg/mL
Mouse IL-10 standard (ThermoFisher) 88-7064-88	4000 pg/mL - 31.25 pg/mL

2.16 Seahorse analysis

(Oxygen Consumption rate and Extracellular acidification rate measurements)

The seahorse XFe96 analyzer was used to measure key metabolic parameters such as extracellular acidification rate (ECAR) and oxygen consumption rate (OCR) in microglia and BMDMs. The XFe96 analyzer automatically measures OCR and ECAR via a series of compound injections and subsequently monitors cellular response in real-time. OCR and ECAR indicate mitochondrial respiration and glycolysis, respectively (see **Table 2.13** for details). The seahorse assay was done according to the Seahorse XFe96 fluxpak protocol.

Briefly after microglia or BMDMs harvest (**2.9.1 and 2.9.3**), $5x10^4$ cells were seeded in XFe96 cell culture microplates in DMEM overnight (corner wells were not seeded to avoid variability in results). The next day, the cells were stimulated as stated in section **2.10** (final volume, 200 μL/well) and the XFe96 sensor cartridges were humidified by adding 200 μL assay calibrant to each well. The humidified cartridge was placed was incubated at 37 °C without CO_2 overnight. On the assay day, bubbles formed in the cartridge were removed and the stimulated cells were washed 3 times with 200 μL prewarmed seahorse assay medium (RPMI, see **2.6**). Next, the cells were incubated with 180 μL assay medium in a non-carbonated incubator at 37 °C for 1 hr. During the cell incubation period, the injection ports of the cartridge were loaded with inhibitors of electron transport chain (ETC) components diluted in assay medium (**Table 2.13**). The cartridge was then inserted in the seahorse XFe 96 analyzer machine and the plate layout was input in the seahorse program (Wave v2.4). Baseline and injection measurements were programmed according to **Table 2.14**. The assay volume was set to 180 μL and the cartridge was left in the machine to calibrate. Finally, after 1 hr of cell incubation, the culture plate was placed in the seahorse XFe96 analyzer machine and the seahorse assay was started.

After the assay run, seahorse data was exported from the software as a pzfx file which was further analyzed using Prism 9.0. The measurement readouts that can be calculated from the seahorse data include; basal respiration, non-mitochondrial respiration, ATP production, proton leak, maximal respiration and spare respiratory capacity (**Figure 2.3)**. The calculation of these mitochondrial respiration parameters is presented in **Table 2.15**.

Table 2.13: Seahorse assay injected compounds

Compound/ETC inhibitor	Final Concentration after injection
Glucose	10 mM
Oligomycin	1 μM
FCCP	2 μM
Antimycin A/Rotenone	0.5/2.5 μM

Table 2.14: Seahorse program for assay measurement

Measurement type	Program
Baseline	5 x, 2 min. Mix, 2 min. Measure
Injections 1 - 4	3 x, 2 min. Mix, 2 min, Measure

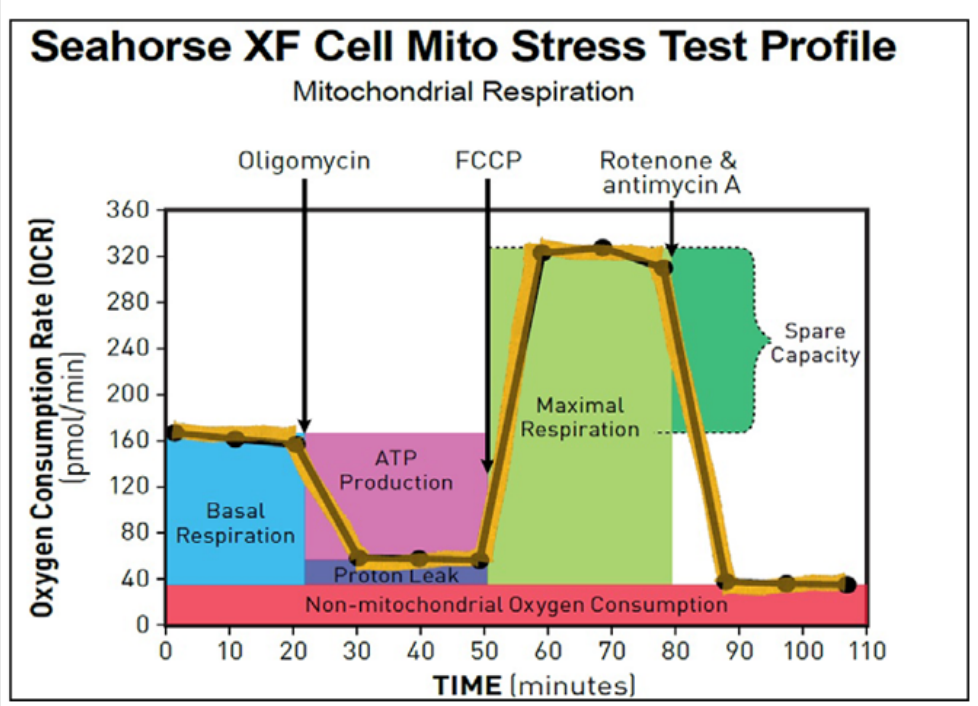

Figure 2.3: Overview of Seahorse mitochondrial respiration analysis (Agilent Seahorse XFe96 analyzer Mito Stress assay parameters) (https://www.agilent.com/cs/library/usermanuals/public/Report_Generator_User_Guide_Seahorse_XF_Cell_Mito_Stress_Test_Single_File.pdf)

Table 2.15: Calculation of mitochondrial respiration parameters

Parameter	Calculation
Basal respiration	(Last rate measurement before the first injection) – (Non-mitochondrial respiration)
Non-mitochondrial respiration	Minimum rate measurement after Rotenone/ antimycin A injection
ATP production	(Last rate measurement before oligomycin injection) – (Minimum rate measurement after oligomycin injection)
Proton (H+) leak	(Minimum rate measurement after oligomycin injection) – (Non-mitochondrial respiration)
Maximal respiration	(Maximum rate measurement after FCCP injection) – (Non-mitochondrial respiratio)
Spare respiratory capacity	(Maximal respiration) – (Basal respiration)

(https://www.agilent.com/cs/library/usermanuals/public/Report_Generator_User_Guide_Seahorse_XF_Cell_Mito_Stress_Test_Single_File.pdf)

2.17 Statistical analysis

Data are expressed as mean ± SEM from at least two or three independent experiments (see section **2.7.1**). Graph Pad Prism Software Version 9.0 was used for the statistical analysis. D' Agostino- Pearson omnibus test was used to determine if the data were normally distributed for group sizes N greater than 40 (microglia cells from z stacks). Data were analyzed using one-way or two-way analysis of variance (ANOVA), followed by Sidak's post hoc test for multiple comparisons between groups. If more than one group was not normally distributed, Kruskal – Wallis test, followed by Dunn's multiple comparisons test was used. p values < 0.05 were considered statistically significant.

2.18 Collaborators and integrated project

The seahorse assay was carried out in collaboration with Eike Geissmar, a PhD student from Prof. Dr. Eicke Latz's group. Eike Geissmar stimulated the primary microglia cells obtained from our lab and carried out the Seahorse assay.

3. Results

3.1 Role of CB2 in TLR-induced microglial activation (Genetic knockout studies)

3.1.1 Primary microglia from CB2$^{-/-}$ mice are less responsive to TLR stimulation

To investigate the role of CB2 in TLR-induced microglial activation, we first assessed the impact of CB2 deletion on the inflammatory profiles of primary microglia stimulated with three selected TLR ligands. We used PolyI:C for TLR3 stimulation, LPS/IFN-γ for TLR4 and CpG for TLR9, as described in (section **2.10**). These TLRs were selected based on their differential localization in the cell and the preferential signaling pathways they activate. While TLR4 is a membrane-bound receptor, TLR3 and 9 are endosomal-based. These receptors can either act via MyD88 signaling or TRIF signaling routes to modulate inflammatory response. This would allow us to determine the distinct effect of CB2 on each TLR-mediated microglial activation. Experimental setup is displayed in **Figure 3.1A.**

Since inflammatory chemokines and cytokines and secretion are known to increase during inflammatory stimulation, we measured their levels in the supernatants of WT and CB2$^{-/-}$ microglia following the three TLR stimulations (**Figure 3.1B-E**). We found that LPS/IFN-γ stimulation showed a significant increase in all the cytokines tested ($p < 0.0001$ for TNF-α, IL-6, CCL2 and $p = 0.0011$ for IL-1β) in WT microglia (**Figure 3.1B-E**). However, upon CB2 deletion, TNF-α, IL-6 and CCL2 levels were significantly reduced ($p_{(TNF\text{-}\alpha)} = 0.007$, $p_{(IL\text{-}6)} = 0.00011$, and $p_{(CCL2)} = 0.0451$) compared to WT microglia cells. PolyI:C stimulation caused a significant increase only in TNF-α secretion ($p = 0.0035$), which was significantly reduced in CB2$^{-/-}$ microglia ($p = 0.0328$). CpG on the other hand, did not affect the tested cytokine secretion ($p > 0.9999$) in both WT and CB2$^{-/-}$ microglia (**Figure 3.1B-E**).

After ELISA cytokine measurement, we also investigated the microglial marker Iba1(ionized calcium-binding adapter molecule 1) staining intensity, as another measure of microglial activation. As Iba1 expression is elevated during inflammatory stimulation, we stained TLR-stimulated microglia with Iba1 and analyzed the staining intensity (**Figure 3.2A**). After LPS/IFN-γ stimulation, Iba1 intensity was significantly increased ($p < 0.0001$) in WT microglia, which was significantly reduced ($p = 0.0002$) in CB2$^{-/-}$ microglia (**Figure 3.2B-C**). Poly I:C similarly increased ($p < 0.0001$) Iba1 intensity in WT microglia as in LPS/

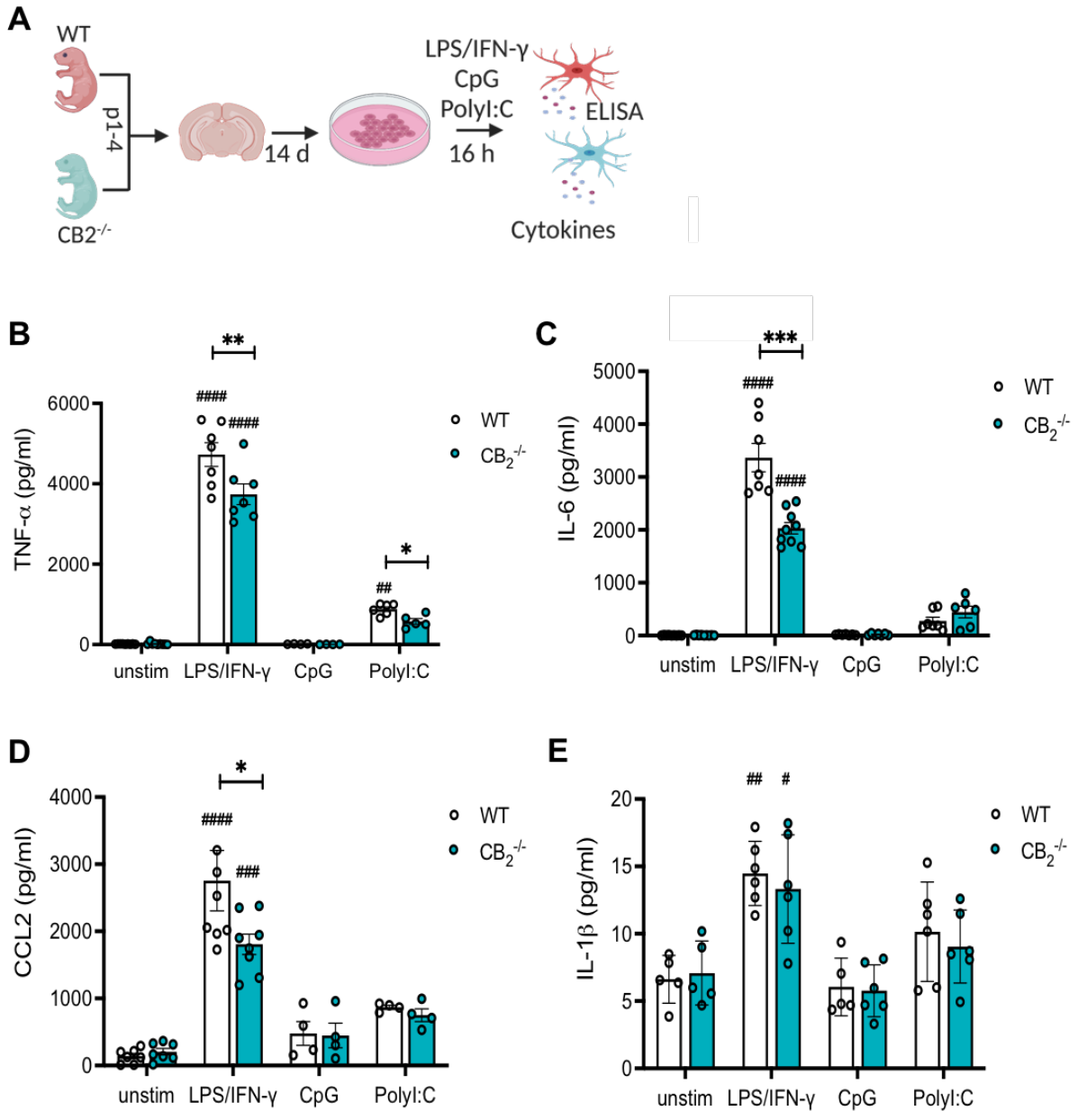

Figure 3.1: Inflammatory cytokine secretion from WT and CB2$^{-/-}$ microglia after TLR stimulation. (**A**) Experimental setup. Levels of cytokines/chemokines were quantified in supernatants of microglia stimulated with TLR ligands for 16 hr. (**B**) TNF-α, (**C**) IL-6, (**D**) CCL2, and IL-1β. N = 5-9 samples/genotype/stimulation (from three independent preparations). Data are presented as mean ± SEM. Two-way ANOVA followed by Sidak's multiple comparisons. Significant differences between WT and CB2$^{-/-}$ are indicated with *** $p < 0.001$, ** $p < 0.01$, * $p < 0.05$. Significance to the unstimulated genotype control are indicated with #### $p < 0.0001$, ### $p < 0.001$, ## $p < 0.01$, # $p < 0.05$.

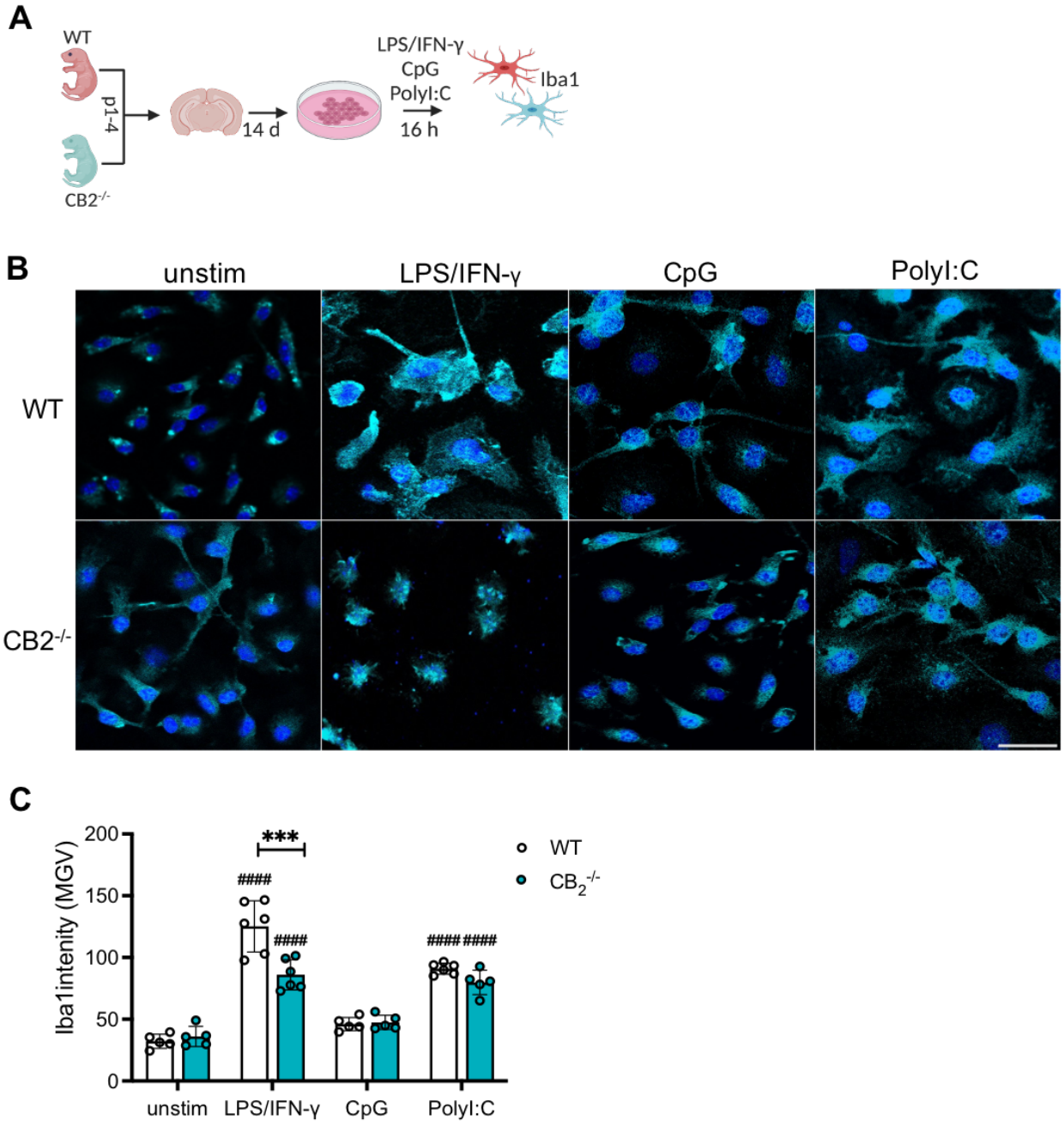

Figure 3.2: Iba1 staining intensity in WT and CB2$^{-/-}$ microglia after TLR stimulation. (**A**) Experimental setup. Iba1 intensity was analyzed in the stained slides of microglia stimulated with TLR ligands for 16 hr. (**B**) Representative confocal images of Iba1(cyan) and DAPI (blue) staining at 40x magnification, scale bar = 100 μm. (**C**) Quantification of Iba1intensity. N = 4-6 samples/genotype/stimulation (from two independent experiments). Data are presented as mean ± SEM. Two-way ANOVA followed by Sidak's multiple comparisons. Significant differences between WT and CB2$^{-/-}$ are indicated with *** $p < 0.001$. Significance to the unstimulated genotype control is as indicated with #### $p < 0.0001$.

IFN-γ stimulation. While there appeared to be a slight decrease in Iba1 intensity of CB2$^{-/-}$ microglia stimulated with PolyI:C, this effect was not significant (p = 0.6408) compared to the WT (**Figure 3.2B-C**). Again, CpG did not significantly alter Iba1 intensity in both WT and CB2$^{-/-}$ microglia ($p_{(WT)}$ = 0.7487, $p_{(CB2^{-/-})}$ = 0.9502) (**Figure 3.2C**).

Altogether, our results showed that CB2$^{-/-}$ microglia are less responsive to TLR3/4 stimulation, whereas TLR9 has little to no effect on WT and CB2$^{-/-}$ microglia regarding inflammatory cytokine secretion and Iba1 expression.

3.1.2 Protein analysis of MAPK, Akt and NF-κB phosphorylation in TLR-stimulated microglia

Next, we wanted to investigate the possible underlying mechanism by which CB2 deletion prevents TLR-induced microglial activation. Therefore, we measured the phosphorylation status of MAPK member proteins, ERK and p38 MAPK as well as survival-associated Akt and transcription factor NF-κB, which are commonly activated during inflammatory stimulation. We used the automated western blotting system (WES) to determine these proteins' phosphorylation levels in WT and CB2$^{-/-}$ microglia stimulated with TLR ligands at two time points (30 min and 16 hr). We tested two different time points because phosphorylation is an event that can either be short-lived or prolonged over a longer duration of inflammatory exposure (**Figure 3.3A**).

We found a significant increase in the phosphorylation of all the proteins tested after 30 min of LPS/IFN-γ stimulation (p = 0.0376 for pERK/ERK (**Figure 3.3B+D**), p = 0.0173 for pAkt/Akt (**Figure 3.4A+C**), p < 0.0001 for pp38/p38 (**Figure 3.5A+C**) and p = 0.0011 for pNF-κB/NF-κB (**Figure 3.5F+H**)) in WT microglia. This effect was sustained until 16 hr of LPS/IFN-γ stimulation in the WT microglia (p = 0.0001 for pERK/ERK (**Figure 3.3B+F**), p = 0.0082 for pAkt/Akt (**Figure 3.4A+E**), p < 0.0001 for pp38/p38 (**Figure 3.5A+E**) and p = 0.0073 for pNF-κB/NF-κB (**Figure 3.5F+J**)).

In CB2$^{-/-}$ microglia, we found a striking decrease, particularly in p38 phosphorylation after 16 hr of LPS/IFN-γ stimulation (p < 0.0001) compared to the WT (**Figure 3.5A+E**). Whereas other proteins tested showed no significant difference between WT and CB2$^{-/-}$ after 16 hr of LPS/IFN-γ stimulation. We only observed a stimulation effect which was generally increased ($p_{(16\ hr)}$ = 0.0001 for pERK/ERK (**Figure 3.3B+F**), $p_{(30\ min)}$

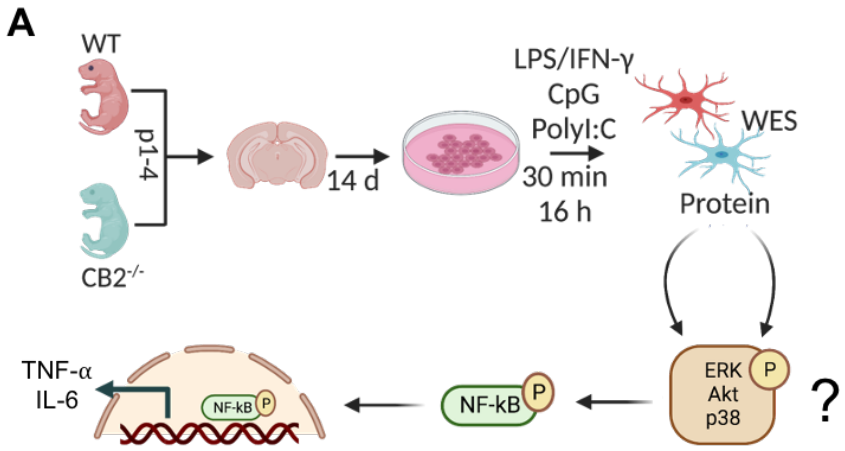
A
WT
p1-4
CB2-/-
14 d
LPS/IFN-γ
CpG
PolyI:C
30 min
16 h
WES
Protein
ERK
Akt
p38
P
?
NF-kB
TNF-α
IL-6

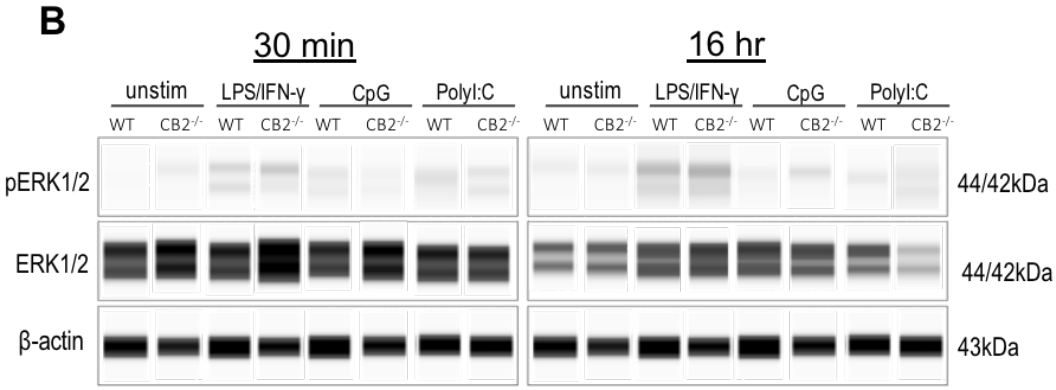
B
30 min
16 hr
unstim
LPS/IFN-γ
CpG
PolyI:C
WT
CB2-/-
pERK1/2
ERK1/2
β-actin
44/42kDa
44/42kDa
43kDa

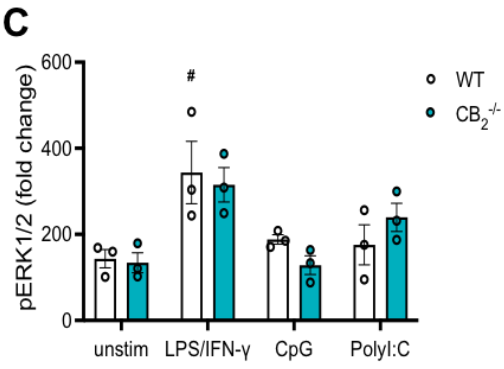
C
pERK1/2 (fold change)
WT
CB2-/-
unstim
LPS/IFN-γ
CpG
PolyI:C

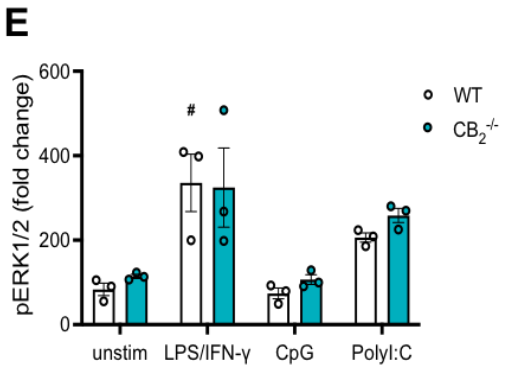
E
pERK1/2 (fold change)
WT
CB2-/-
unstim
LPS/IFN-γ
CpG
PolyI:C

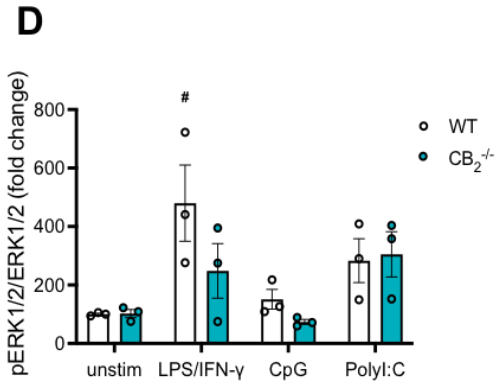
D
pERK1/2/ERK1/2 (fold change)
WT
CB2-/-
unstim
LPS/IFN-γ
CpG
PolyI:C

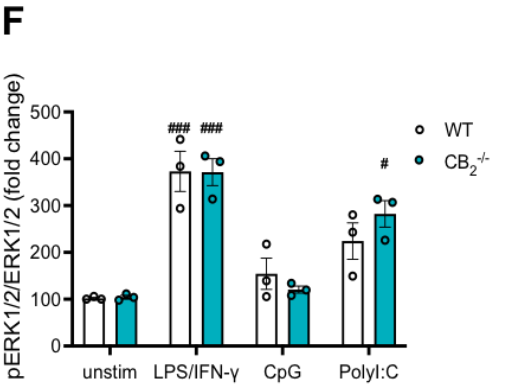
F
pERK1/2/ERK1/2 (fold change)
WT
CB2-/-
unstim
LPS/IFN-γ
CpG
PolyI:C

Figure 3.3: ERK1/2 phosphorylation activity shows no significant difference between WT and CB2$^{-/-}$ microglia stimulated with TLR ligands. (**A**) Experimental setup. The phosphorylation level of ERK1/2 was quantified in cell lysate of microglia stimulated with TLR ligands for 30 min and 16 hr (**B**) Representative WES blots of ERK1/2, pERK1/2 and β-actin after 30 min and 16 hr stimulation with TLR ligands, LPS/IFN-γ, CpG and PolyI:C. Quantitative analysis of (**C**) pERK1/2 and (**D**) pERK1/2/ERK1/2 after 30 min stimulation. Quantification of (**E**) pERK1/2 and (**F**) pERK1/2/ERK1/2 after 16 hr stimulation. N = 3 samples/genotype/stimulation. Data are presented as mean ± SEM. Two-way ANOVA followed by Sidak's multiple comparisons. Significance to the unstimulated genotype control is as indicated with ### p < 0.001, # p < 0.05.

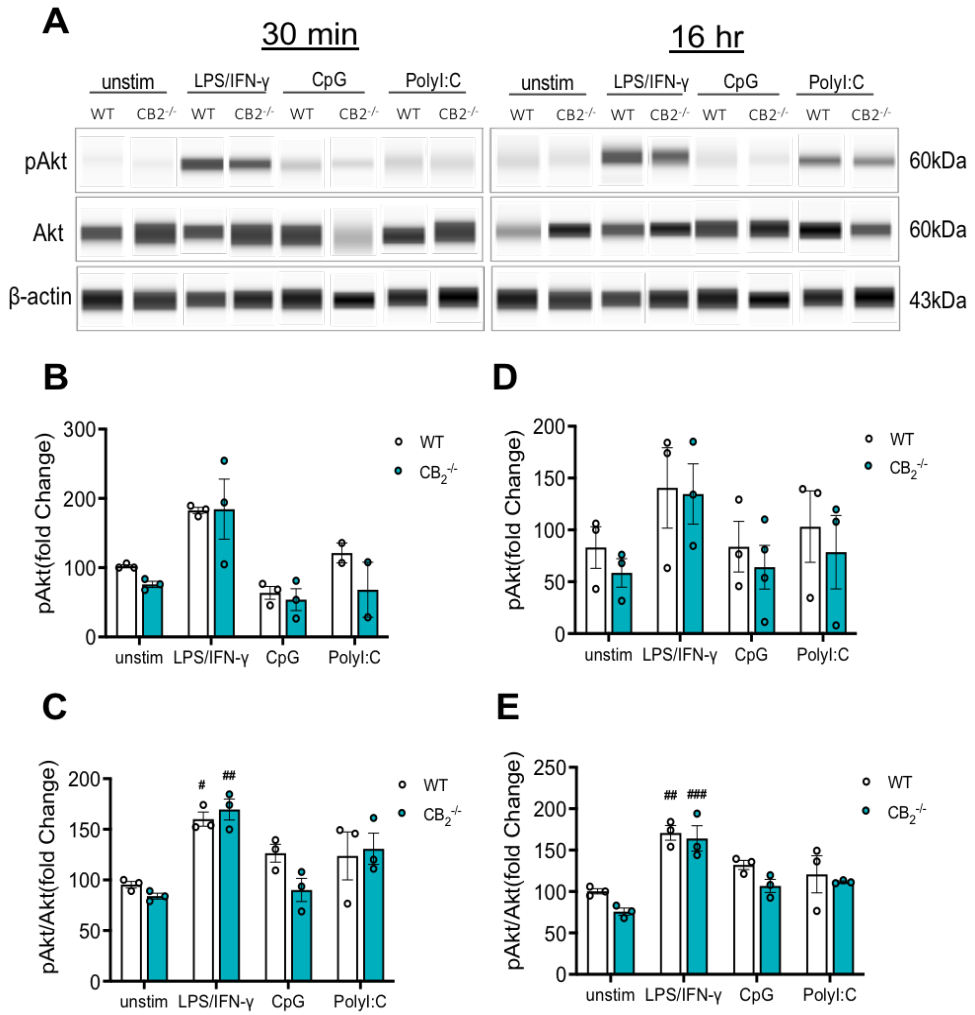

Figure 3.4: Akt phosphorylation activity shows no significant difference between WT and CB2$^{-/-}$ microglia after TLR stimulation. Phosphorylation level of Akt was quantified in cell lysate of microglia stimulated with TLR ligands for 30 min and 16 hr. (**A**) Representative WES blots of Akt, pAkt, and β-actin after 30 min and 16 hr stimulation with TLR ligands, LPS/IFN-γ, CpG and PolyI:C. Quantitative analysis of (**B**) pAkt and (**C**) pAkt/Akt after 30 min stimulation. Quantitative analysis of (**D**) pAkt and (**E**) pAkt/Akt after 16 hr stimulation. N = 3 samples/genotype/stimulation. Data are presented as mean ± SEM. Two-way ANOVA followed by Sidak's multiple comparisons. Significance to the unstimulated genotype control is as indicated with ### p < 0.001, ## p < 0.01, # p < 0.05.

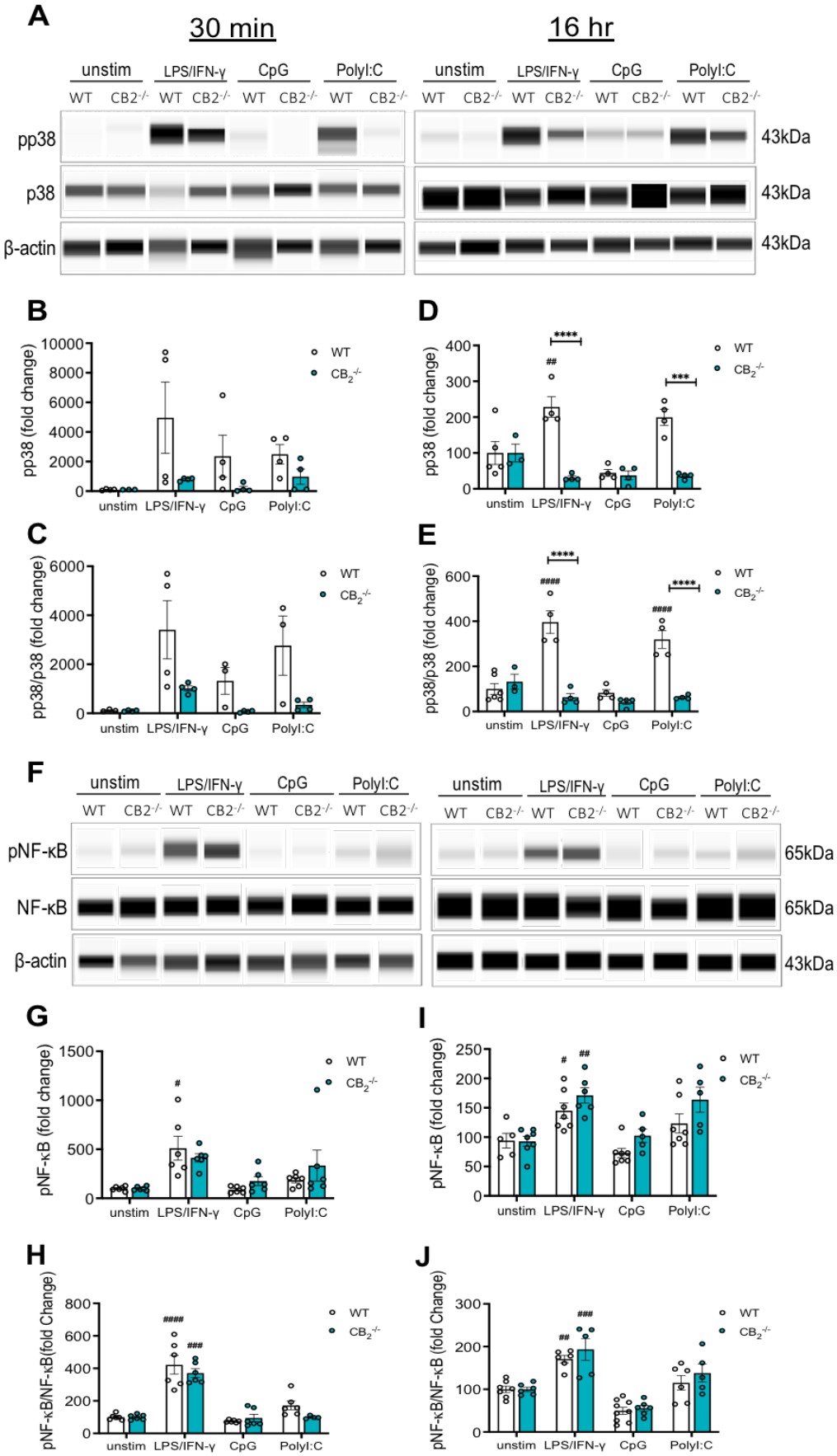
A
30 min
16 hr
unstim
LPS/IFN-γ
CpG
PolyI:C
WT
CB2-/-
pp38
p38
β-actin
43kDa
B
pp38 (fold change)
WT
CB2-/-
unstim
LPS/IFN-γ
CpG
PolyI:C
C
pp38/p38 (fold change)
D
E
F
pNF-κB
NF-κB
β-actin
65kDa
G
pNF-κB (fold change)
H
pNF-κB/NF-κB(fold Change)
I
J

Figure 3.5: p38 but not NF-κB phosphorylation activity decreased significantly in CB2$^{-/-}$ microglia compared to WT after TLR3/4 stimulation. Phosphorylation levels of p38 and NF-κB were quantified in cell lysates of microglia stimulated with TLR ligands for 30 min and 16 hr. (**A**) Representative WES blots of p38, pp38, and β-actin after 30 min and 16 hr stimulation with TLR ligands, CpG and PolyI:C. Quantitative analysis of (**B**) pp38 and (**C**) pp38/p38 after 30 min stimulation. Quantitative analysis of (**D**) pp38 and (**E**) pp38/p38 after 16 hr stimulation. (**F**) Representative WES blots of NF-κB, p NF-κB, and β-actin after 30 min and 16 hr stimulation with TLR ligands, CpG and PolyI:C. Quantitative analysis of (**G**) pNF-κB and (**H**) pNF-κB/ NF-κB after 30 min stimulation. Quantitative analysis of (**I**) p NF-κB and (**J**) pNF-κB / NF-κB after 16 hr stimulation. N = 3 -9 samples/genotype/stimulation (from 3 independent preparations). Data are presented as mean ± SEM. Two-way ANOVA followed by Sidak's multiple comparisons. Significant differences between WT and CB2$^{-/-}$ are indicated with **** $p < 0.0001$, *** $p < 0.001$. Significance to the unstimulated genotype control is as indicated with #### $p < 0.0001$, ### $p < 0.001$, ## $p < 0.01$, # $p < 0.05$.

= 0.0012, $p_{(16\ hr)}$ = 0.0008 for pAkt/Akt (**Figure 3.4A-E**), and $p_{(30\ min)}$ = 0.0001, $p_{(16\ hr)}$ = 0.0005 for pNF-κB/NF-κB (**Figure 3.5F-J**) in the CB2$^{-/-}$ microglia.

Similar to LPS/IFN-γ, PolyI:C stimulation for 16 hr also caused increased p38 phosphorylation in WT microglia ($p < 0.0001$), which was significantly reduced in CB2$^{-/-}$ microglia ($p < 0.0001$) (**Figure 3.5A+E**). However, we found no significant change in phosphorylation of other proteins ERK, Akt and NF-κB following 30 min or 16 hr PolyI:C stimulation between WT and CB2$^{-/-}$ microglia. (**Figures 3.3, 3.4, 3.5**). On the contrary, CpG does not significantly affect the phosphorylation status of the tested proteins in both WT and CB2$^{-/-}$ microglia. These data indicate that p38 phosphorylation is distinctly involved in CB2-mediated microglial activation following TLR3/4 stimulation.

Overall, p38 MAPK phosphorylation was particularly diminished in CB2$^{-/-}$ microglia compared to WT.

3.2 Role of CB2 in TLR-induced microglial activation (Pharmacological inhibition studies)

3.2.1 The CB2 antagonist SR144528 suppresses TLR-induced microglial cytokine secretion only at high concentration

We asked whether pharmacological inhibition of the CB2 has similar effects on TLR4-induced microglial activation as in the CB2 constitutive knockout model. Pharmacological validation is required for genetic constitutive knockout results, especially to rule out a possible compensatory mechanism that might have been triggered due to a permanent lack of CB2. Therefore, we tested the effects of SR144528, the most commonly used CB2 antagonist, on TLR-induced cytokine secretion. This time, we focused on TLR3 and TLR4 stimulation because TLR9 stimulation had no significant effect on microglial activation in $CB2^{-/-}$ mice. 15 min before TLR stimulation, we pre-treated WT microglia with increasing concentrations of SR144528, after which we stimulated with PolyI:C and LPS/IFN-γ for 16 hr. We did this SR144518 titration to identify the concentration at which we observed a significant difference in cytokine secretion between LPS/IFN-γ-stimulated microglia and those pre-treated with SR144528. We then measured cytokine levels in the supernatants of the stimulated microglia using ELISA (**Figure 3.6A**).

We observed that LPS/IFN-γ stimulation significantly increased the secretion of all cytokines tested ($p < 0.0001$ for TNF-α, IL-6, CCL2 and $p = 0.0099$ for IL-1β) (**Figure 3.6B-E**). This response was not affected by pre-treatment with SR144528 at nanomolar concentrations where the compound should be CB2 selective. Only a concentration of 1 μM significantly reduced LPS/IFN-γ-induced secretion of TNF-α ($p = 0.0009$), IL-6 ($p = 0.0094$) and CCL2 ($p = 0.0182$) (**Figure 3.6B-E**). Somewhat similar trend was observed in PolyI:C stimulated microglia pre-treated with SR144528. We found a significant increase in the cytokines TNF-α ($p < 0.001$), IL-6 ($p < 0.0001$), and CCL2 ($p = 0.049$) in PolyI:C stimulated microglia, which was not affected by SR144528 pre-treatment at the nanomolar concentrations (**Figure 3.7A-C**).

Taken together, we observed no significant change between TLR3/4-stimulated microglia and those pre-treated with SR144528 at nanomolar concentrations.

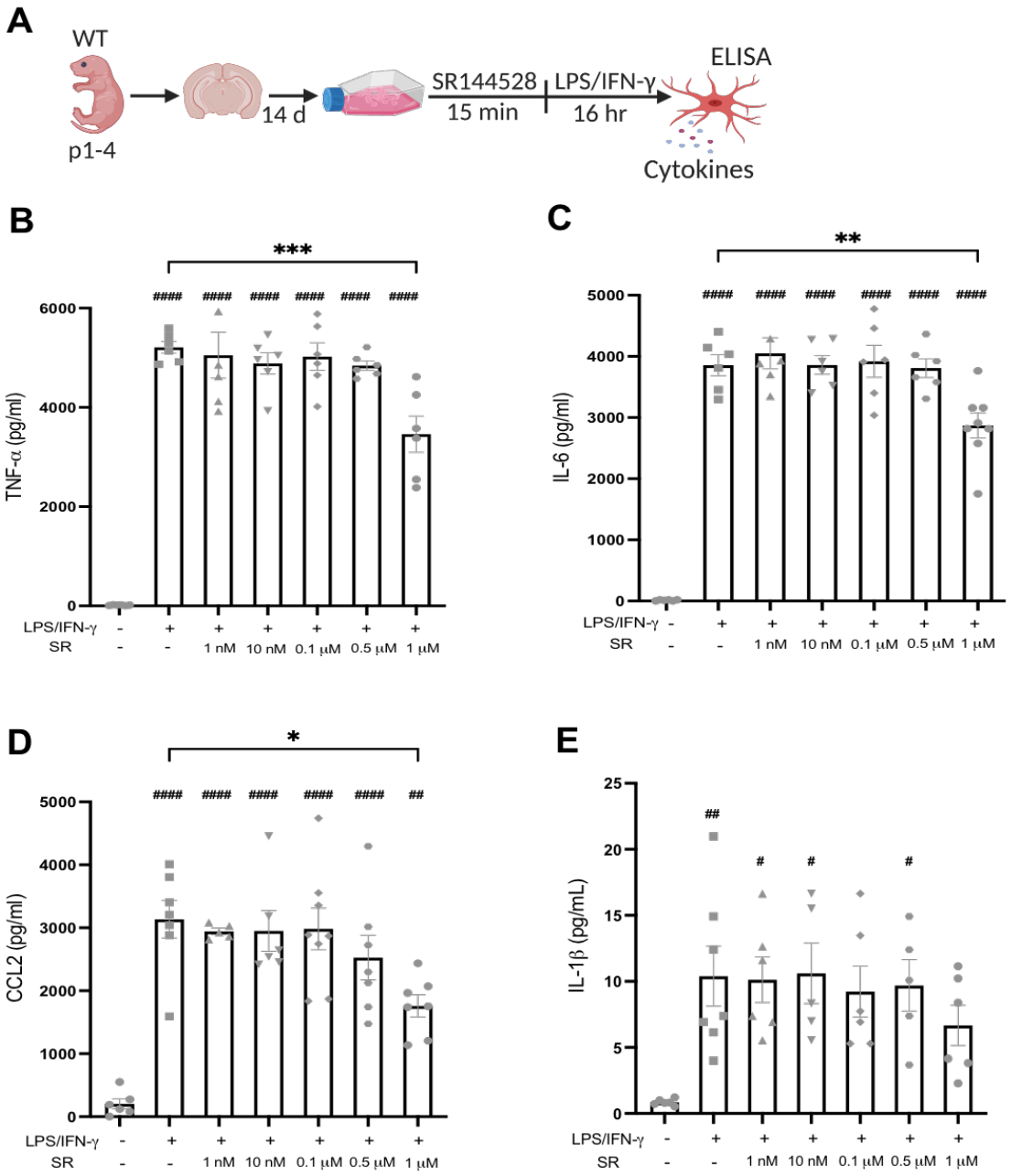

Figure 3.6: SR144528 reduced TLR4-mediated microglial cytokine/chemokine secretion only at 1 μM. (**A**) Experimental setup. Levels of cytokines/chemokines were measured in supernatants of microglia pre-treated with SR144528 (SR) at the indicated concentrations, followed by LPS/IFN-γ stimulation for 16 h. (**B**) TNF-α, (**C**) IL-6, (**D**) CCL2, and (**E**) IL-1β. N = 5 - 8 samples/stimulation from three independent preparations. Data are presented as mean ± SEM. One-way ANOVA followed by Sidak's multiple comparisons. #### $p < 0.0001$, ### $p < 0.001$, ## $p < 0.01$, # $p < 0.05$ indicate significance to the untreated control group. Significant differences between LPS/IFN-γ vs. LPS/IFN-γ pre-treated with SR144528 are indicated with *** $p < 0.001$, ** $p < 0.01$, * $p < 0.05$.

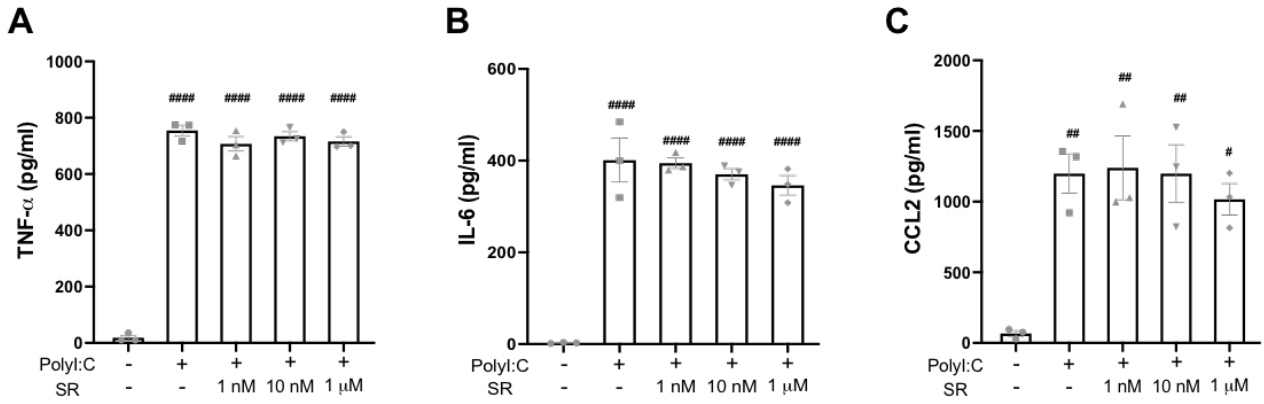

Figure 3.7: SR144528 has no effect on TLR3-mediated microglial cytokine/ chemokine secretion. Levels of cytokines/chemokines were quantified in supernatants of microglia pre-treated with SR144528 (SR) at the indicated concentrations, followed by PolyI:C stimulation for 16 hr. (**A**) TNF-α, (**B**) IL-6, and (**C**) CCL2. N = 3-4 samples/ stimulation (representative from two independent preparations). Data are presented as mean ± SEM. One-way ANOVA followed by Sidak's multiple comparisons. #### $p < 0.0001$, ## $p < 0.01$, # $p < 0.05$ indicate significance to the untreated control group.

3.2.2 SR144528 has no effect on cytokine secretion in unstimulated microglia

Next, we wondered if SR144528 has an effect on microglial secretion when treated alone without combination with TLR ligands. Here, we used SR144528 at the relevant nanomolar concentrations that should effectively block the CB2 receptors (1 nM - 100 nM). Again, SR144528 did not produce any significant change in the tested cytokine secretion between control and those treated with SR144528 alone, indicating that SR144528 does not affect cytokine secretion in unstimulated conditions (**Figure 3.8A-C**).

This finding, together with the previous result clearly showed that SR144528 has no effect on microglial cytokine secretion with or without TLR stimulation.

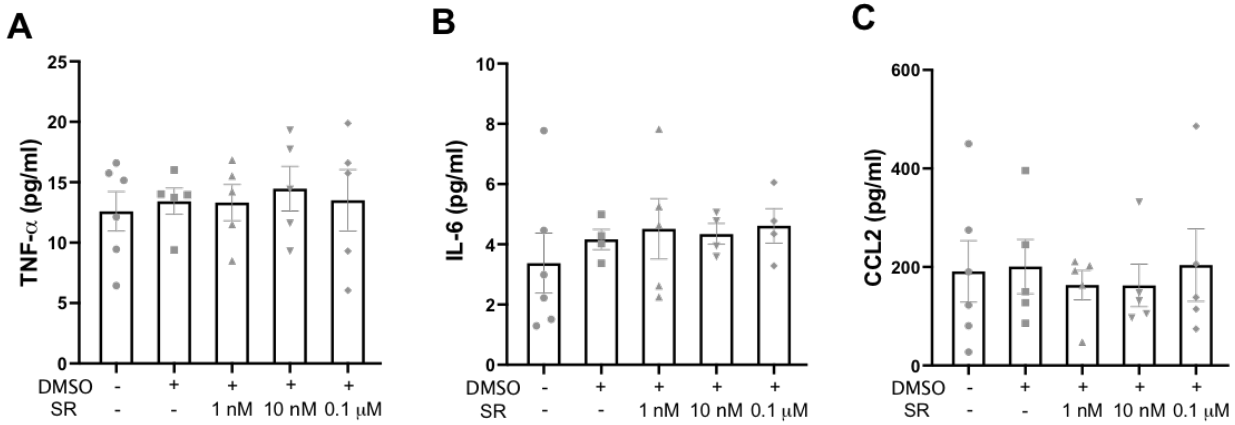

Figure 3.8: SR144528 has no affect cytokine/chemokine secretion in unstimulated control microglia. Levels of cytokines/chemokines were quantified in supernatants of SR144528 (SR)-treated microglia at the indicated concentrations using ELISA. (**A**) TNF-α, (**B**) IL-6, and (**C**) CCL2 N = 4 - 6 samples/treatment from two independent preparations. Data are presented as mean ± SEM. One-way ANOVA followed by Sidak's multiple comparisons.

3.2.3 SR144528 (at nM) does not affect CD68 intensity in the CA1 region of OHSCs before and after TLR stimulation

We further investigated the effect of SR144528 on another endpoint of inflammatory stimulation, namely CD68 (a lysosomal marker for phagocytosis). For this purpose, we used OHSCs, a model that supports the physiological maintenance of all hippocampal cell types in culture to assess CD68 intensity. We pre-treated OHSCs with SR144528 (1 nM and 10 nM) for 15 min, followed by TLR3/4 stimulation for 16 hr (**Figure 3.9A**). We then stained the OHSCs for CD68, after which we acquired z stack images using the confocal microscope. An example OHSCs staining is shown in (**Figure 3.9B**). After that, we analyzed the area covered by CD68 and the density of CD68 particles in the CA1 pyramidal/radiatum layer of the treated OHSCs (**Figure 3.10, 3.11**).

Our results showed that the area covered by CD68 significantly increased in the CA1 region after LPS/IFN-γ ($p = 0.0009$, (**Figure 3.10A+B**)) and PolyI:C stimulation ($p = 0066$, {**Figure 3.11A+B**}). This effect was not significantly affected upon SR144528 pre-treatment. We also showed a similar trend for CD68 particle density; TLR3/4 stimulation caused an increase in particle density of CD68 ($p < 0.0001$ for LPS/IFN-γ {**Figure 3.10C** and $p = 0.0411$ for PolyI:C {**Figure 3.11C**}) which was not significantly altered upon SR144528 pre-treatment.

This data revealed no influence of SR144528 on CD68 intensity in CA1 region of the hippocampal slices after LPS/IFN-γ or PolyI:C stimulation.

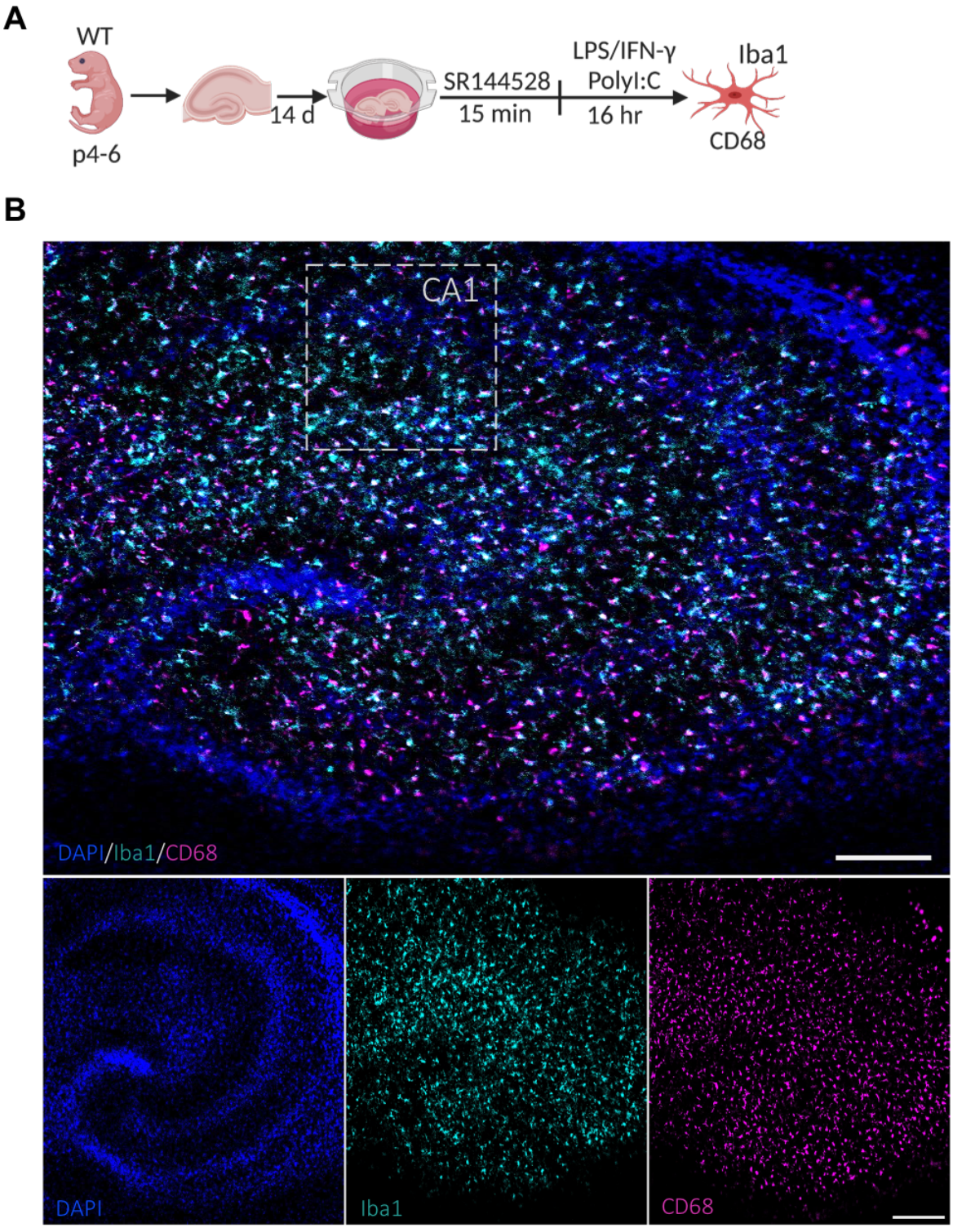

Figure 3.9: Overview of Iba1 and CD68 stainings in LPS/IFN-γ-stimulated OHSCs. (**A**) Experimental setup. (**B**) Example confocal images of LPS/IFN-γ-stimulated OHSCs showing DAPI (blue), Iba1 (cyan), and CD68 (magenta). Scale bar: 100 μm, 10x magnification. The white dotted box indicates the section from which representative CA1 region shown in Figure 3.10/3.11 and microglia shown in Figure 3.13/3.14 were obtained.

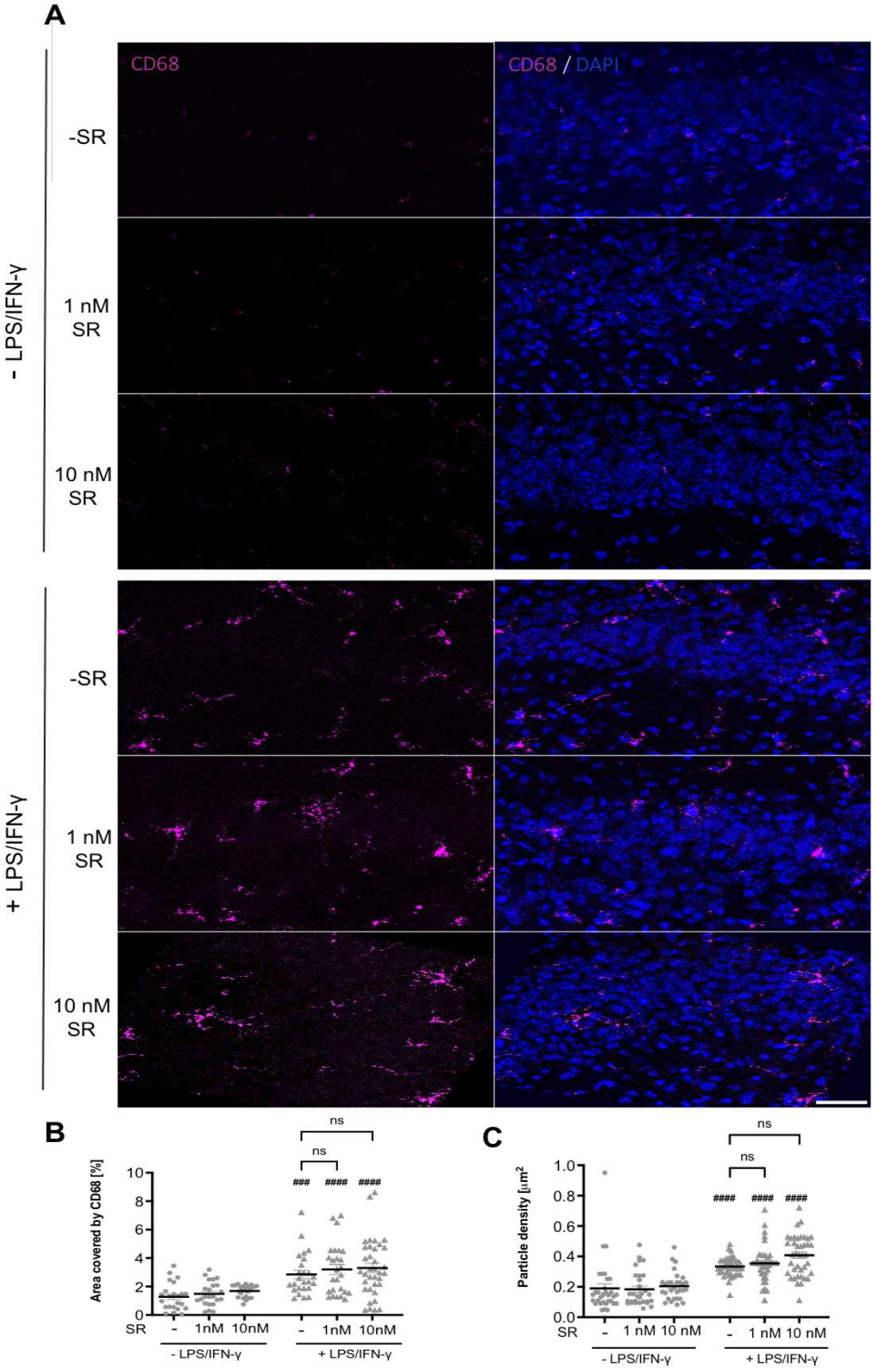
A
CD68
CD68 / DAPI
- LPS/IFN-γ
-SR
1 nM SR
10 nM SR
+ LPS/IFN-γ
-SR
1 nM SR
10 nM SR
B
Area covered by CD68 [%]
ns
ns
####
SR - 1nM 10nM - 1nM 10nM
- LPS/IFN-γ
+ LPS/IFN-γ
C
Particle density [µm²]
ns
ns
####
SR - 1 nM 10 nM - 1 nM 10 nM
- LPS/IFN-γ
+ LPS/IFN-γ

Figure 3.10: SR144528 does not affect CD68 activity in the CA1 region of TLR4-stimulated OHSCs. CD68 level was analyzed in the CA1 region of LPS/IFN-γ stimulated OHSCs pre-treated with SR144528 (SR). (**A**) Representative confocal images of CD68 (magenta) and DAPI (blue) staining at 40x magnification, scale bar = 50 μm. Quantification of (**B**) Area covered by CD68 and (**C**) Particle density. N ≥ 40 microglia from z stacks /stimulation (representative data from 2 independent OHSCs preparations). Data are presented as mean ± SEM. Two-way ANOVA followed by Sidak's multiple comparisons was used for normally distributed data. For data that were not normally distributed, Kruskal –Wallis test followed by Dunn's multiple comparisons tests was used. #### $p < 0.0001$, ### $p < 0.001$ indicate significance to the untreated control group.

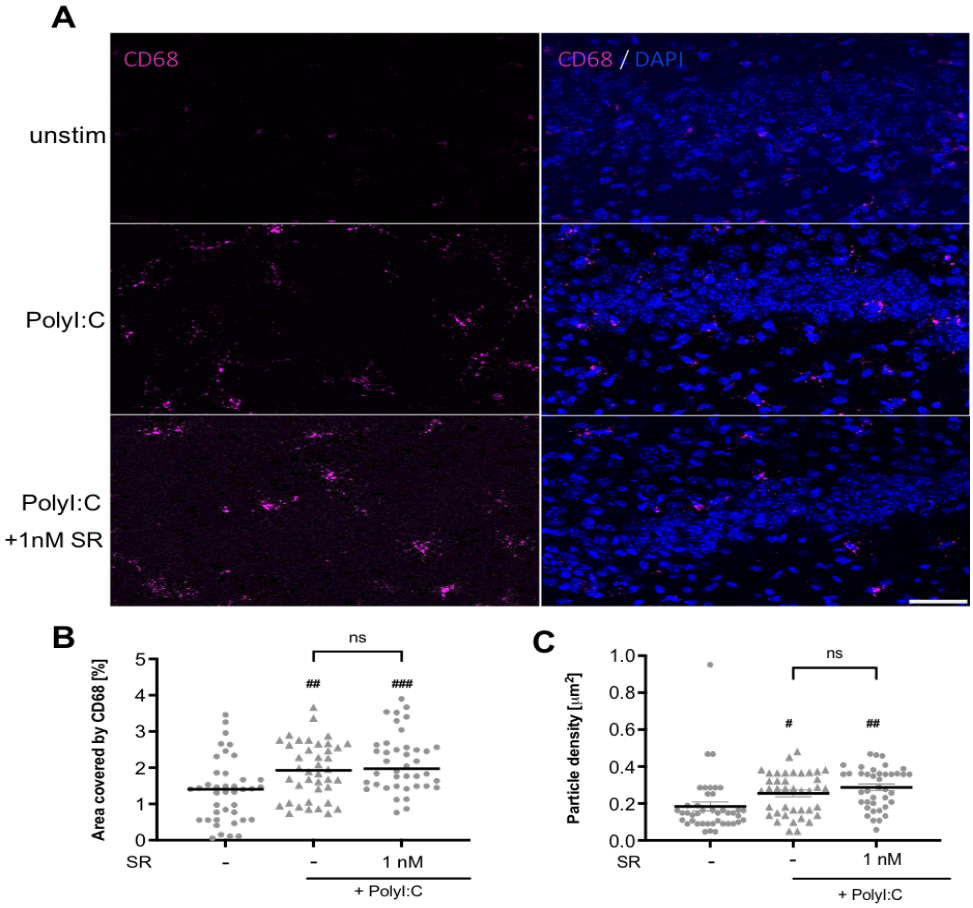

Figure 3.11: SR144528 does not affect CD68 activity in the CA1 region of TLR3-stimulated OHSCs. CD68 level was analyzed in the CA1 region of PolyI:C stimulated OHSCs pre-treated with 1nM SR144528 (SR). (**A**) Representative confocal images of CD68 (magenta) and DAPI (blue) staining at 40x magnification, scale bar = 50 μm. Quantification of (**B**) Area covered by CD68 and (**C**) Particle density. N ≥ 40 microglia from z stacks /stimulation (representative data from 2 independent OHSCs preparations). Data are presented as mean ± SEM. One-way ANOVA followed by Sidak's multiple comparisons was used for normally distributed data. For data that were not normally distributed, Kruskal –Wallis test followed by Dunn's multiple comparisons tests was used. #### $p < 0.0001$, ### $p < 0.001$, ## $p < 0.01$, # $p < 0.05$ indicate significance to the untreated control group.

3.2.4 SR144528 (at nM) does not affect microglial Iba1 and CD68 intensities in TLR-stimulated OHSCs

To further determine the effect of SR144528 on TLR-induced activation specifically in microglia, we assessed the intensity of the microglial marker Iba1 (ionized calcium-binding adapter molecule 1) as well as the immunoreactivity of CD68 in Iba1 positive cells of stimulated OHSCs. We pre-treated OHSCs with SR144528 for 15 min, followed by LPS/IFN-γ or PolyI:C stimulation for 16 hr (**Figure 3.9A**). We measured the Iba1 and CD68 staining intensities within the Iba1 positive region of interest (ROI) of the OHSCs CA1 region.

We found that both Iba1 and CD68 intensities were significantly increased ($p < 0.0001$) after LPS/IFN-γ stimulation. However, pre-treatment with SR144528 (1 nM, 10 nM) did not considerably change Iba1 or CD68 intensities (**Figure 3.13**). In accordance with the LPS/IFN-γ stimulation, PolyI:C also increased Iba1 and CD68 intensities in the CA1 region of the OHSCs ($p_{(Iba1)} = 0.0050$, $p_{(CD68)} < 0.0001$), whereas 1 nM SR144528 failed to produce a significant change upon its pre-treatment (**Figure 3.14**).

In summary, we showed that nanomolar concentrations of SR144528 did not affect microglial Iba1 and CD68 staining intensities after TLR stimulation.

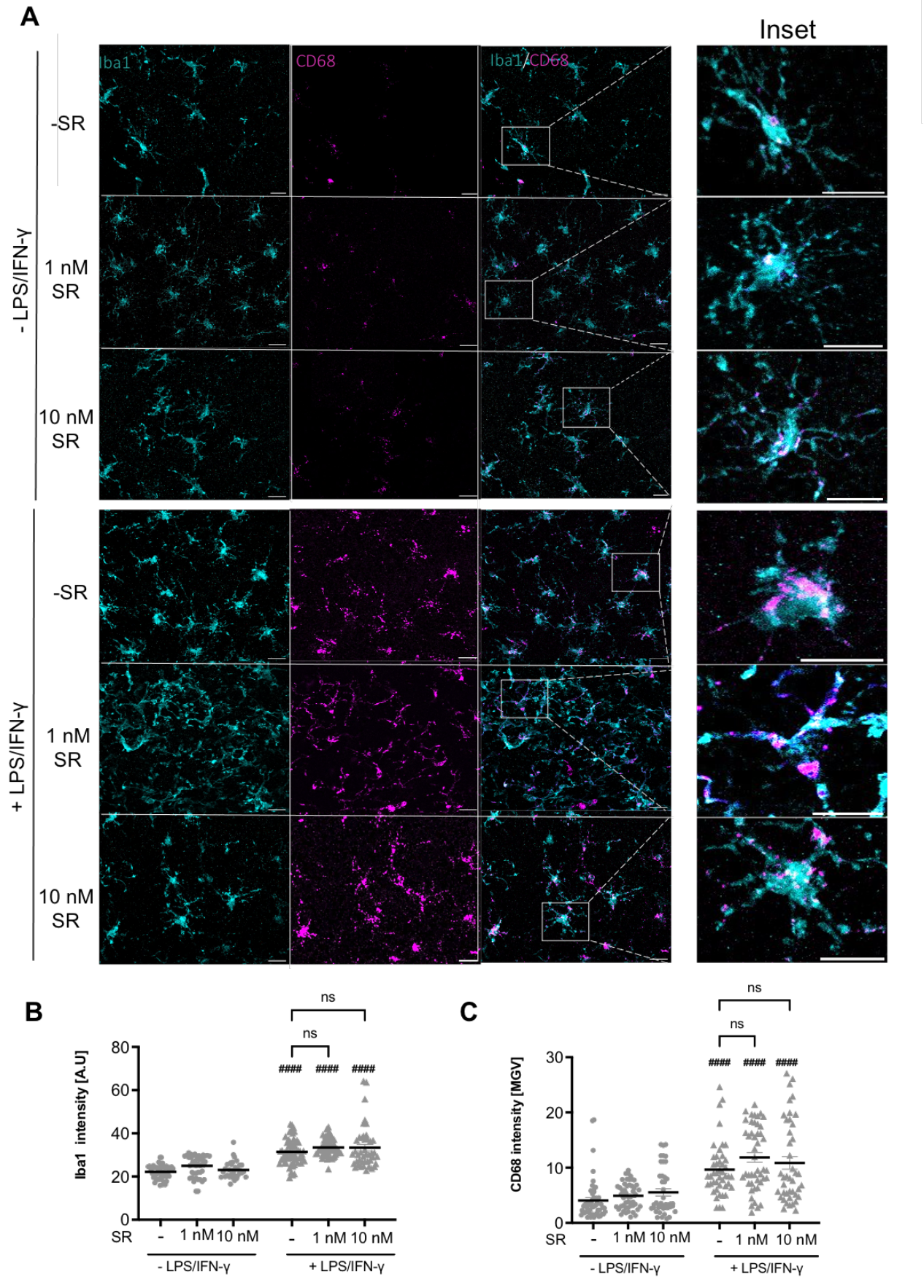
A
Inset
Iba1
CD68
Iba1/CD68
-SR
1 nM SR
10 nM SR
- LPS/IFN-γ
+ LPS/IFN-γ
B
Iba1 intensity [A.U]
ns
ns
####
SR
- 1 nM 10 nM
- LPS/IFN-γ
+ LPS/IFN-γ
C
CD68 intensity [MGV]

Figure 3.12: SR144528 does not affect microglial Iba1 and CD68 intensities in TLR4-stimulated OHSCs. Iba1 and CD68 intensities were analyzed in the Iba1+ CA1 region of OHSCs pre-treated with SR144528 (SR) at the indicated concentrations, followed by LPS/IFN-γ stimulation for 16 hr. (**A**) Representative microscopy images of Iba1(cyan) and CD68 (magenta) staining at 40 x magnification, scale bar = 30 μm. Quantification of (**B**) Iba1 and (**C**) CD68 intensities. N ≥ 40 microglia from z stacks /stimulation (representative data from 2 independent OHSCs preparations). Data are presented as mean ± SEM. Two-way ANOVA followed by Sidak's multiple comparisons was used for normally distributed data. For data that were not normally distributed, Kruskal –Wallis test followed by Dunn's multiple comparisons tests was used. #### $p < 0.0001$ indicates significance to the untreated control group.

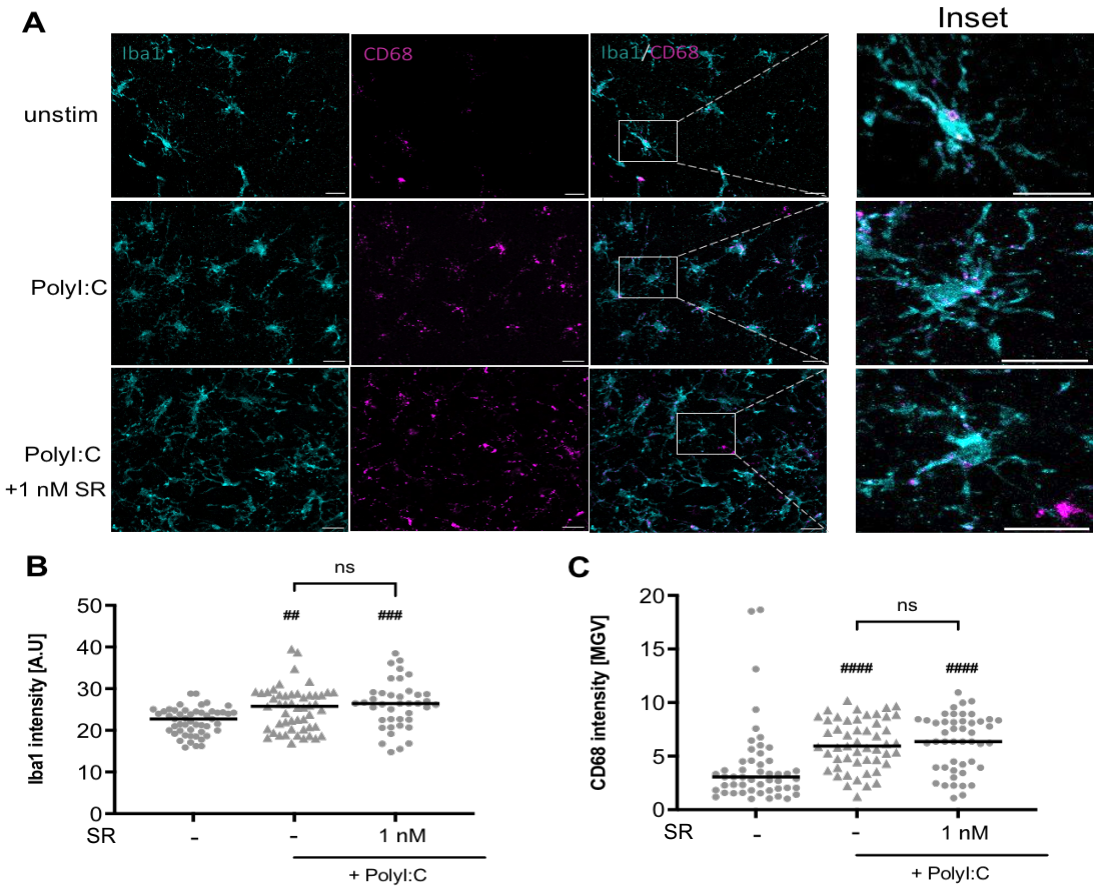

Figure 3.13: SR144528 does not affect microglial Iba1 and CD68 intensities in TLR3-stimulated OHSCs. Iba1 and CD68 intensities were analyzed in the Iba1 positive CA1 region of PolyI:C stimulated OHSCs pre-treated with 1 nM SR144528 (SR). (**A**) Representative microscopy images of Iba1(cyan) and CD68 (magenta) staining at 40 x magnification, scale bar = 30 μm. Quantification of (**B**) Iba1 and (**C**) CD68 intensities. N ≥ 40 microglia from z stacks /stimulation (representative data from 2 independent OHSCs preparations). Data are presented as mean ± SEM. One-way ANOVA followed by Sidak's multiple comparisons was used for normally distributed data. For data that were not normally distributed, Kruskal –Wallis test followed by Dunn's multiple comparisons tests was used. #### $p < 0.0001$, ### $p < 0.001$, ## $p < 0.01$ indicate significance to the untreated control group.

3.2.5 SR144528 (at nM) does not considerably alter microglial morphology in TLR stimulated OHSCs

We next determined microglial morphology as another readout of microglial activation in TLR-stimulated OHSCs pre-treated with SR144528 (**Figure 3.14A**). Since microglia transition to a less ramified state during activation, we used the MotiQ plugin (Hansen et al., 2022) to characterize 3D morphometric parameters of microglia in the treated OHSCs (see section **2.14.3**).

We observed that LPS/IFN-γ-stimulated microglia exhibited ameboid-like features such as fewer branches (**Figure 3.14 B+C**), shorter tree lengths (**Figure 3.14B+D**), lower surface (**Figure 3.14F**), and lower cell volume (**Figure 3.14G**). However, these parameters were not altered by SR144528 (1 nM and 10 nM). On the contrary, polarity and ramification index- a measure of the overall complexity of cell shape and primed microglia significantly increased with 10 nM of SR144528 pre-treatment (**Figure 3.14E, Figure 3.14H**).

In PolyI:C-stimulated microglia, we found a significant decrease in all the analyzed morphological parameters except volume, which was unaffected by 1 nM SR144528 pre-treatment (**Figure 3.15B-H**).

These findings further show that SR144528 does not alter the ameboid-like features of activated microglia after TLR3/4 stimulation.

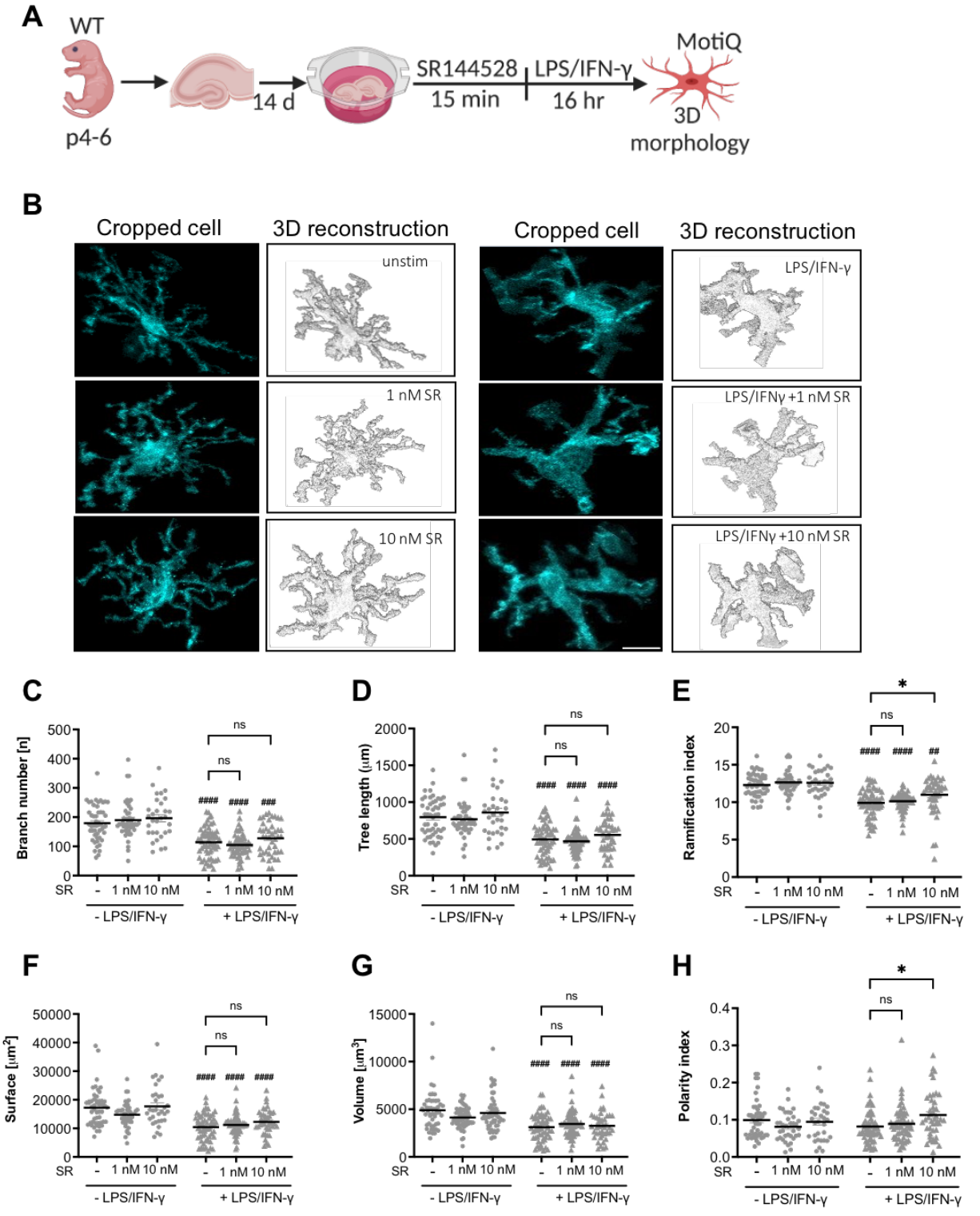

Figure 3.14: SR144528 does not alter 3D microglial morphology in LPS/IFN-γ stimulated OHSCs. Microglia morphology was analyzed using MotiQ plugin in Iba1 positive cells of OHSCs pre-treated with SR144528 (SR) at the indicated concentrations, followed by LPS/IFN-γ stimulation for 16 hr. (**A**) Experimental setup. (**B**) Representative images of 3D reconstructed microglia. Scale bar = 30 µm. (**C-H**) Quantification of

morphological parameters of reconstructed microglia. (**C**) Branch number, (**D**) Tree length, (**E**) Ramification index, (**F**) Surface, (**G**) Volume, and (**H**) Polarity index. N ≥ 40 microglia from z stacks /stimulation (representative data from 2 independent OHSCs preparations). Data are presented as mean ± SEM. Two-way ANOVA followed by Sidak's multiple comparisons. #### p < 0.0001, ### p < 0.001, ## p < 0.01 indicate significance to the untreated control group. Significant differences between LPS/IFN-γ vs. LPS/IFN-γ pre-treated with SR144528 is indicated as * p < 0.01.

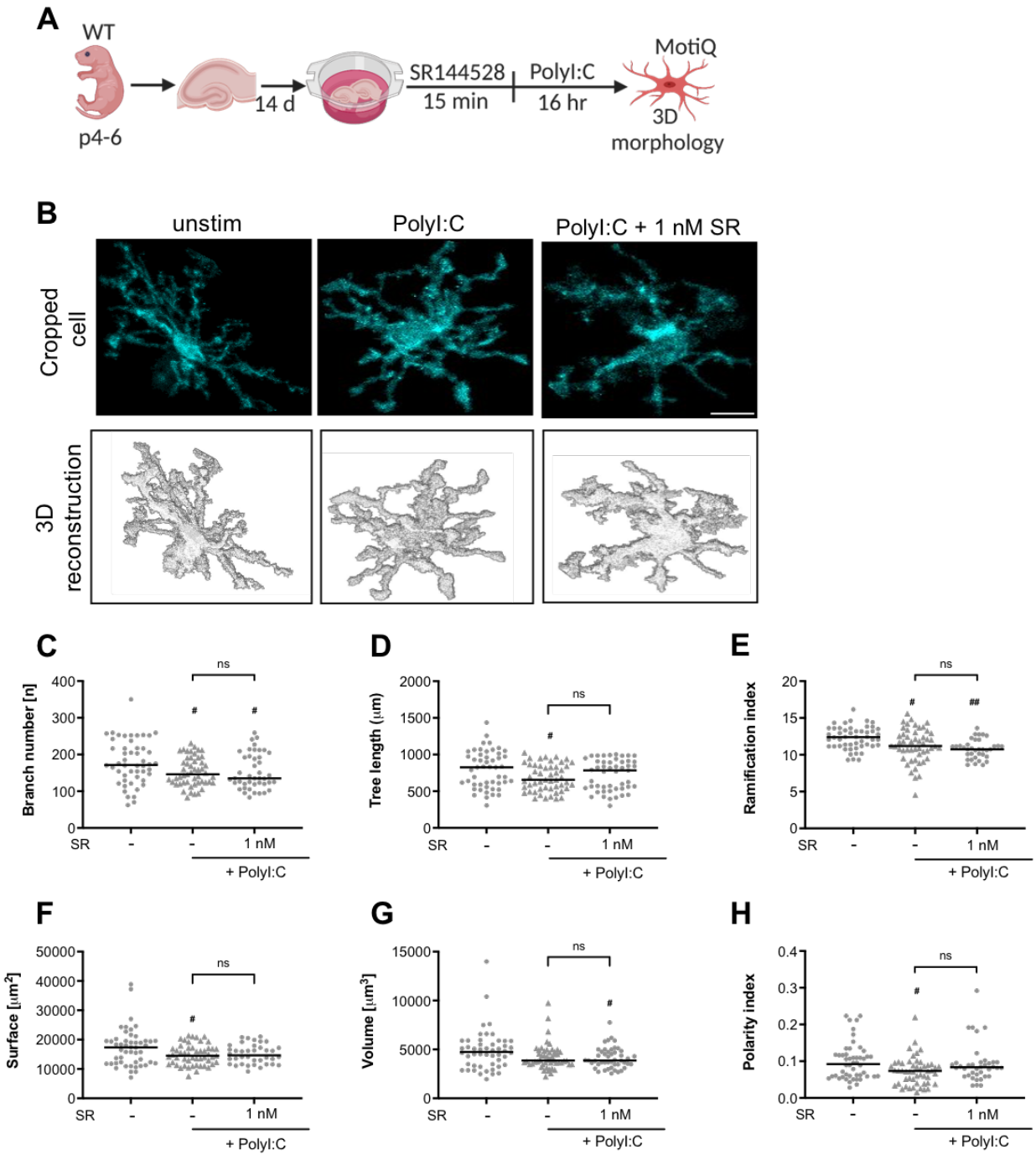

Figure 3.15: SR144528 does not alter 3D microglial morphology in PolyI:C stimulated OHSCs. Microglia morphology was analyzed using MotiQ plugin in Iba1 positive cells of OHSCs pre-treated with SR144528 (SR) at the indicated concentration, followed by PolyI:C stimulation for 16 hr. (**A**) Experimental setup. (**B**) Representative images of 3D reconstructed microglia. Scale bar = 30 μm. (**C-G**) Quantification of morphological parameters of reconstructed microglia. (**C**) Branch number, (**D**) Tree length, (**E**) Ramification index, (**F**) Surface, (**G**) Volume, and (**H**) Polarity index. N ≥ 40 microglia from z stacks/stimulation (representative data from 2 independent OHSCs preparations). Data are presented as mean ± SEM. One-way ANOVA followed by Sidak's multiple comparisons. ## $p < 0.01$, # $p < 0.05$ indicate significance to the untreated control group.

3.2.6 SR144528 (at nM) does not influence cytokine secretion in TLR4-stimulated Bone marrow-derived macrophages

To test whether SR144528 has an effect on other myeloid cells outside the brain resident microglia, we pre-treated BMDMs with increasing concentrations of SR144528 for 15 min followed by LPS/IFN-γ stimulation for 16 hr (**Figure 3.16A**). We then measured cytokine levels in the supernatants of the stimulated macrophages using ELISA. Here, we focused on only TLR4 activation because this is where we observed the most pronounced effect of inflammatory stimulation.

In line with the microglia data, we confirmed that SR144528 has no effect on TLR4-induced cytokine secretion in the BMDMs also. Indeed, we observed that LPS/IFN-γ stimulation significantly increased the secretion of all cytokines tested ($p < 0.0001$ for TNF-α (**Figure 3.16B**), IL-6 (**Figure 3.16C**), CCL2 (**Figure 3.16D**), and $p = 0.0278$ for IL-10 (**Figure 3.16E**)). However, this effect was not affected by SR144528 pre-treatment at the relevant nanomolar concentrations in the BMDMs. Similar but less pronounced as in the microglia, only a concentration of 1 μM significantly reduced LPS/IFN-γ-induced secretion of TNF-α ($p = 0.0226$), IL-6 ($p = 0.0287$), and IL-10 ($p = 0.0354$) in the BMDMs (**Figure 3.16B-E**).

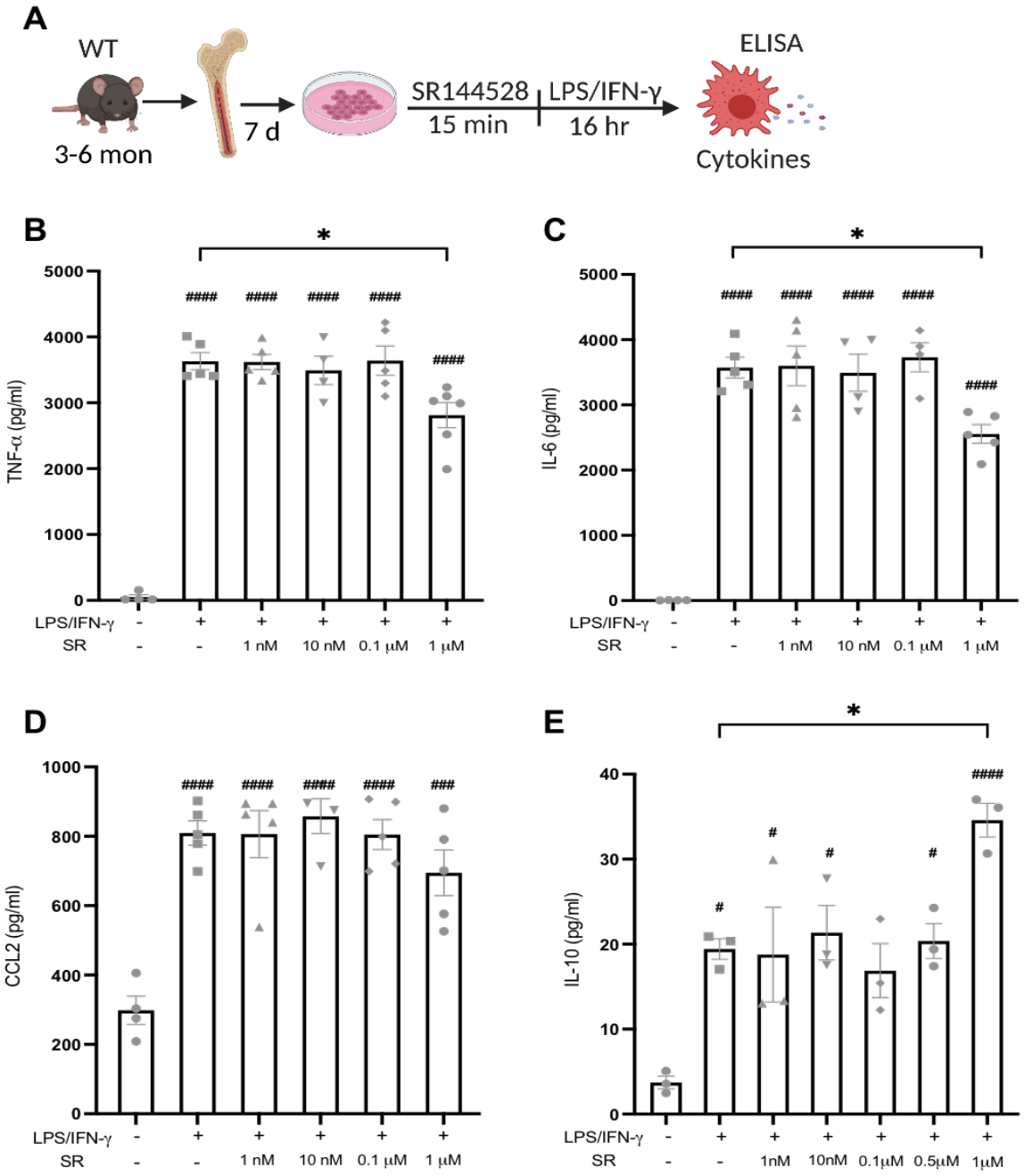

Figure 3.16: SR144528 reduced TLR4-mediated BMDM cytokine/chemokine secretion only at 1 μM. (**A**) Experimental setup. Levels of cytokines/chemokines were quantified in supernatants of BMDMs pre-treated with SR144528 (SR) at the indicated concentrations, followed by LPS/IFN-γ stimulation for 16 hr. (**B**) TNF-α, (**C**) IL-6, (**D**) CCL2, and (**E**) IL-10. N = 3 - 6 samples/stimulation from two independent preparations. Data are presented as mean ± SEM. One-way ANOVA followed by Sidak's multiple comparisons. #### $p < 0.0001$, ### $p < 0.001$, # $p < 0.05$ indicate significance to the untreated control group. Significant difference between LPS/IFN-γ vs. LPS/IFN-γ pre-treated with SR144528 is indicated with * $p < 0.05$.

3.2.7 SR144528 (at 1 μM) reduced TLR4-induced microglial inflammatory cytokine secretion independent of CB2 receptors

Since we found the most prominent decrease in cytokine secretion in LPS/IFN-γ stimulated microglia pre-treated with 1 μM SR144528, we wanted to test whether the anti-inflammatory effect of SR144528 at this concentration is CB2 dependent or not. Therefore, we pre-treated both WT and $CB2^{-/-}$ microglia with 1 μM SR144528 for 15 min followed by LPS/IFN-γ-stimulation for 16 hr. Then, we measured cytokine release in the supernatants of stimulated microglia using ELISA (**Figure 3.17A**).

Indeed, SR144528 at 1 μM significantly reduced TNF-α ($p_{(WT)}$ = 0.0006, $p_{(CB2^{-/-})}$ = 0.0156 (**Figure 3.17B**)) and IL-6 ($p_{(WT)}$ = 0.0030, $p_{(CB2^{-/-})}$ = 0.0029 (**Figure 3.17C**)) secretion in both WT and also $CB2^{-/-}$ microglia after LPS/IFN-γ- stimulation. The reduction in CCL2 secretion did not reach statistical significance in $CB2^{-/-}$ microglia ($p_{(WT)}$ = 0.0110, $p_{(CB2^{-/-})}$ = 0.8022, likely due to their generally lower CCL2 secretion capacity (**Figure 3.17D**).

3.2.8 SR144528 (at 1 μM) decreased CD68 activity in the CA1 region of TLR4-stimulated OHSCs in a CB2 independent manner

We next investigated the effect of 1 μM SR144528 on phagocytosis marker in TLR-stimulated OHSCs. We pre-treated both WT and $CB2^{-/-}$ OHSCs with 1 μM SR144528 for 15 min followed by LPS/IFN-γ stimulation for 16 hr. We then stained the OHSCs with CD68 and acquired z stack images using the confocal microscope. The area covered by CD68 and density of CD68 particles were analyzed in the CA1 pyramidal/radiatum layer of the stimulated OHSCs (**Figure 3.18A**).

In line with the cytokine secretion data, 1 μM of SR144528 decreased the area covered by CD68 in both WT and $CB2^{-/-}$ OHSCs CA1 region ($p_{(WT)}$ = 0.0094, $p_{(CB2^{-/-})}$ = 0.0364 (**Figure 3.18B+C**)). Particle density also seems to decrease slightly in LPS/IFN-γ stimulated WT and $CB2^{-/-}$ OHSCs pre-treated with 1 μM SR144528 (**Figure 3.18D**). However, this effect was not significant ($p_{(WT)}$ = 0.0556, $p_{(CB2^{-/-})}$ = 0.9767).

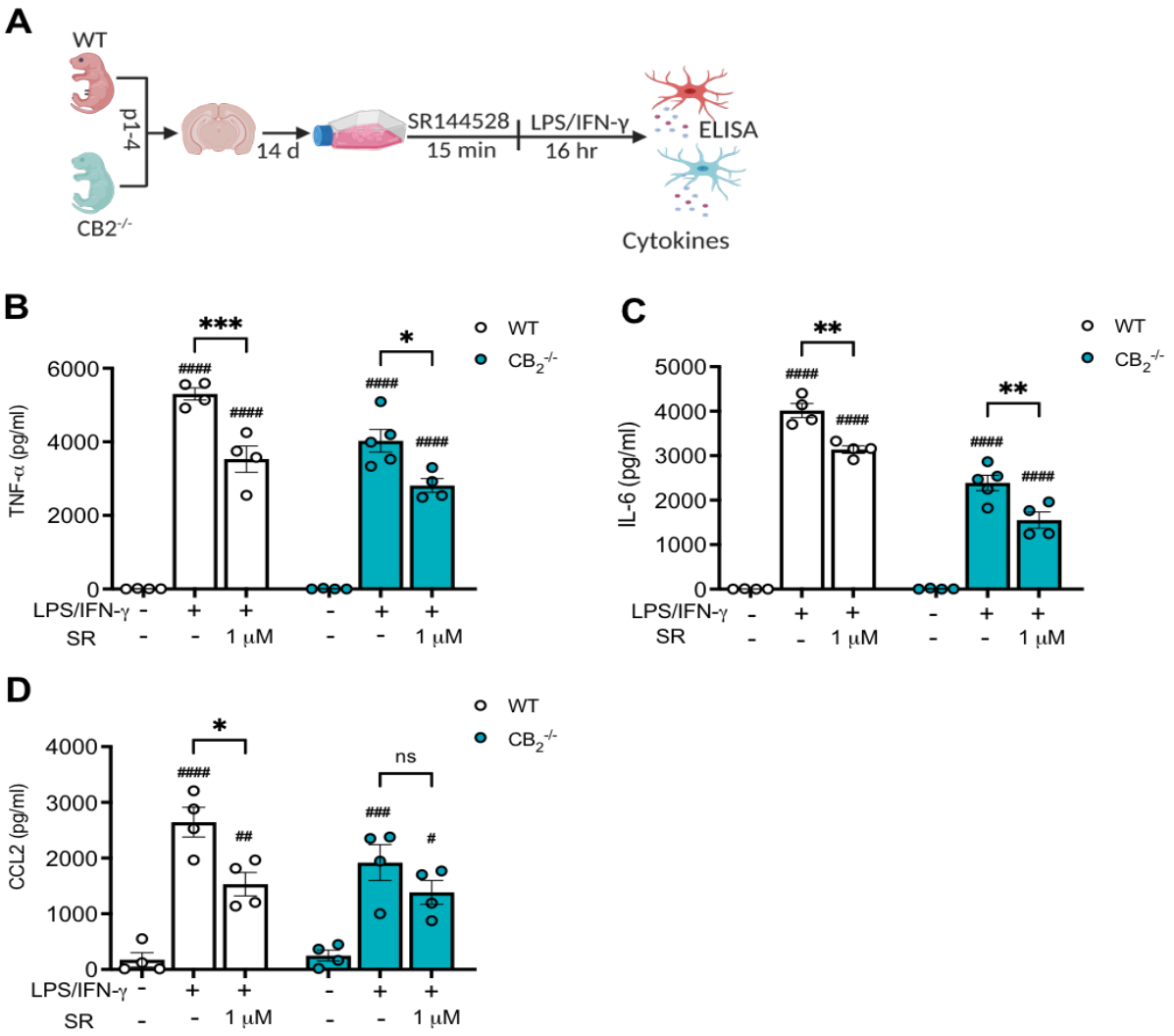

Figure 3.17: 1 μM of SR144528 supressed TLR4-induced microglial inflammatory cytokine secretion independent of CB2 receptor. (**A**) Experimental setup. Levels of cytokines/chemokines were quantified in the supernatants of microglia pre-treated with 1 μM SR144528 (SR), followed by LPS/IFN-γ stimulation for 16 hr using ELISA. (**B**) TNF-α, (**C**) IL-6, and (**D**) CCL2. N = 4-5 samples/genotype/stimulation (representative data from two independent microglia preparations). Data are presented as mean ± SEM. Two-way ANOVA followed by Sidak's multiple comparisons. #### $p < 0.0001$, ### $p < 0.001$, ## $p < 0.01$, # $p < 0.05$ indicate significance to the untreated control group. Significant differences between LPS/IFN-γ vs. LPS/IFN-γ pre-treated with 1 μM SR144528 are indicated as *** $p < 0.001$, ** $p < 0.01$, * $p < 0.05$.

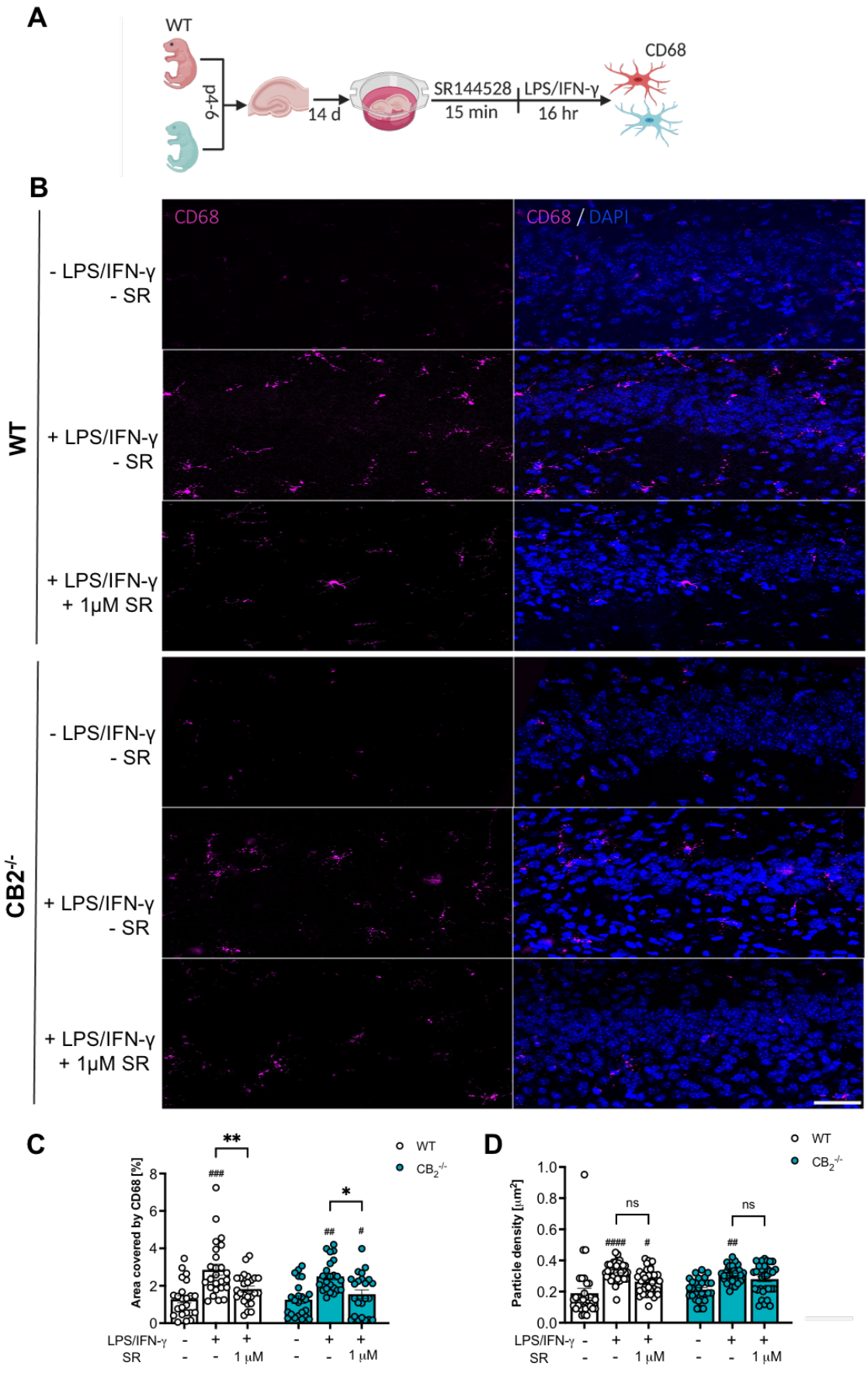
A
WT
p4-6
14 d
SR144528
15 min
LPS/IFN-γ
16 hr
CD68
B
CD68
CD68 / DAPI
WT
- LPS/IFN-γ
- SR
+ LPS/IFN-γ
- SR
+ LPS/IFN-γ
+ 1µM SR
CB2-/-
- LPS/IFN-γ
- SR
+ LPS/IFN-γ
- SR
+ LPS/IFN-γ
+ 1µM SR
C
Area covered by CD68 [%]
WT
CB2-/-
LPS/IFN-γ
SR
1 µM
D
Particle density [µm²]
ns
WT
CB2-/-
LPS/IFN-γ
SR
1 µM

Figure 3.18: 1 μM of SR144528 reduced TLR4-induced CD68 activity in the CA1 region independent of CB2. (**A**) Experimental setup. CD68 activity was analyzed in the CA1 region of LPS/IFN-γ stimulated WT and $CB2^{-/-}$ OHSCs pre-treated with 1 μM SR144528 (SR) using ImageJ. (**B**) Representative confocal images of CD68 (cyan) and DAPI (blue) staining at 40x magnification, scale bar = 50 μm. Quantification of (**C**) Area covered by CD68 and (**D**) Particle density. N ≥ 36 microglia from z stacks /stimulation (representative data from 2 independent OHSCs preparations). Data are presented as mean ± SEM. Two-way ANOVA followed by Sidak's multiple comparisons. #### $p < 0.0001$, ### $p < 0.001$, ## $p < 0.01$, # $p < 0.05$ indicate significance to the untreated control group. Significant differences between LPS/IFN-γ vs. LPS/IFN-γ pre-treated with 1 μM SR144528 are indicated as *** $p < 0.001$, ** $p < 0.01$, * $p < 0.05$.

3.2.9 SR144528 (at 1 μM) does not act via CB2 to modulate TLR4-induced microglial Iba1 and CD68 intensities in OHSCs

We further tested the effect of 1 μM of SR144528 on TLR4-induced microglial Iba1 and CD68 intensities, specifically in the Iba1-positive cells of WT and $CB2^{-/-}$ OHSCs. We pre-treated OHSCs with SR144528 for 15 min, followed by LPS/IFN-γ stimulation for 16 hr (**Figure 3.19A**). We then stained the OHSCs with Iba1 and CD68, after which we analyzed their staining intensities in Iba1 positive ROI of the microglia in the CA1 region (See **3.2.3**).

In agreement with the area covered by CD68 in the CA1 region, we also found that 1 μM of SR144528 significantly reduced microglial Iba1 ($p_{(WT)} = 0.0319$, $p_{(CB2^{-/-})} = 0.0187$ (**Figure 3.19B+C**)) and CD68 ($p_{(WT)} = 0.0207$, $p_{(CB2^{-/-})} = 0.0456$ (**Figure 3.19B+D**)) intensities in both WT and $CB2^{-/-}$ OHSCs.

Overall, this data revealed that 1 μM of SR144528 reduced microglial Iba1 and CD68 intensities in WT as well as $CB2^{-/-}$ OHSCs after TLR4 stimulation.

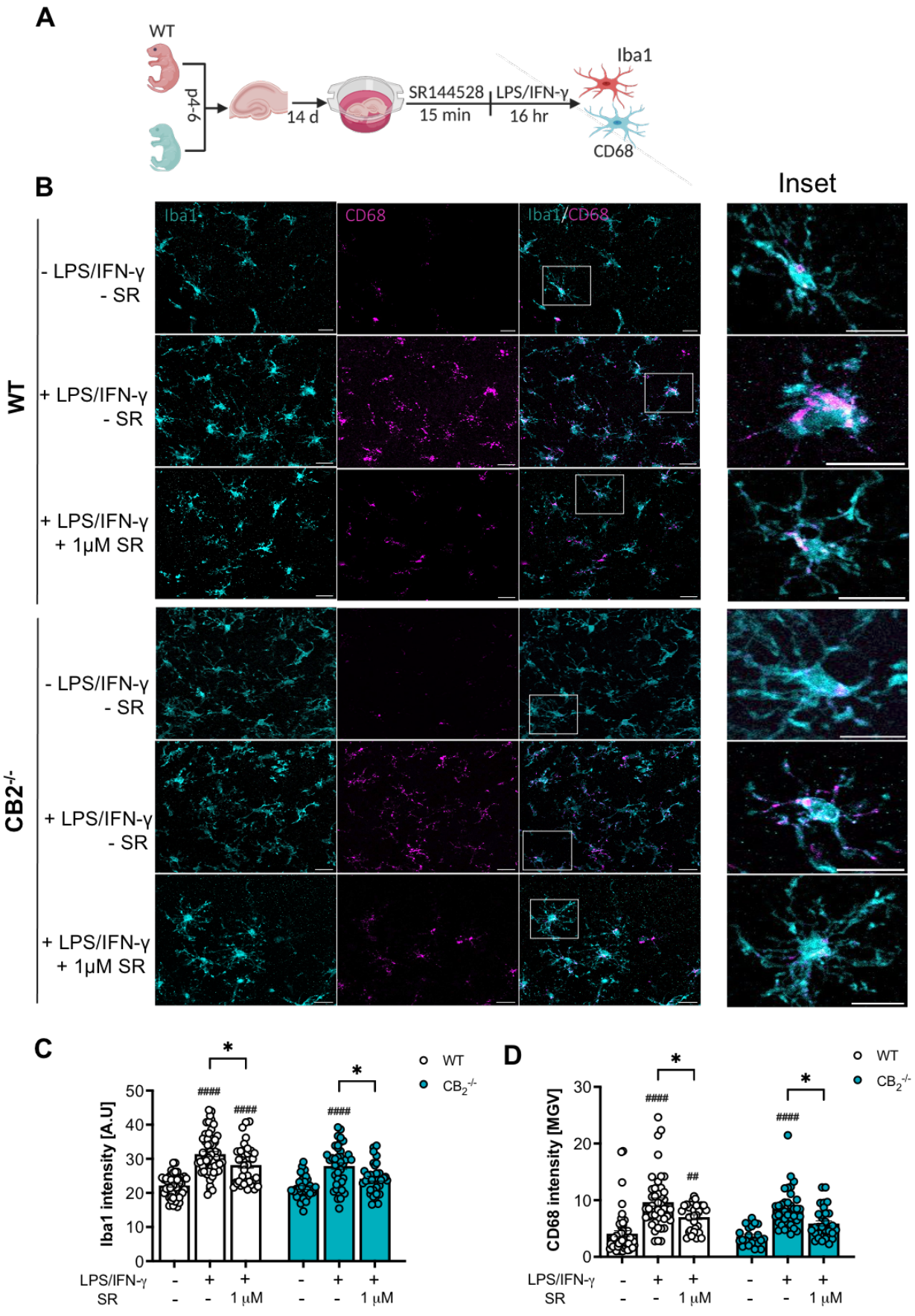
A
WT
p4-6
14 d
SR144528
15 min
LPS/IFN-γ
16 hr
Iba1
CD68
B
Inset
Iba1
CD68
Iba1/CD68
WT
- LPS/IFN-γ
- SR
+ LPS/IFN-γ
- SR
+ LPS/IFN-γ
+ 1μM SR
CB2-/-
- LPS/IFN-γ
- SR
+ LPS/IFN-γ
- SR
+ LPS/IFN-γ
+ 1μM SR
C
Iba1 intensity [A.U]
WT
CB2-/-
LPS/IFN-γ
SR
1 μM
D
CD68 intensity [MGV]
WT
CB2-/-
LPS/IFN-γ
SR
1 μM

Figure 3.19: 1 μM of SR144528 decreased TLR4-induced microglial Iba1 and CD68 intensities in CB2 independent manner. (**A**) Experimental setup. Iba1 and CD68 intensities were analyzed in the CA1 region of WT and $CB2^{-/-}$ OHSCs pre-treated with 1 μM SR144528 (SR), followed by LPS/IFN-γ stimulation for 16 hr. (**B**) Representative microscopy images of Iba1 (cyan) and CD68 (magenta) staining at 40x magnification, scale bar = 30 μm. Quantification of (**C**) Iba1 and (**D**) CD68 intensities. N ≥ 36 microglia from z stacks /stimulation (representative data from 2 independent OHSCs preparations). Data are presented as mean ± SEM. Two-way ANOVA followed by Sidak's multiple comparisons was used for normally distributed data. For data that were not normally distributed, Kruskal –Wallis test followed by Dunn's multiple comparisons tests was used. #### $p < 0.0001$, ### $p < 0.001$, ## $p < 0.01$, # $p < 0.05$ indicate significance to the untreated control group. Significant differences between LPS/IFN-γ vs. LPS/IFN-γ pre-treated with 1 μM SR144528 are indicated as *** $p < 0.001$, ** $p < 0.01$, * $p < 0.05$.

3.2.10 SR144528 (at 1 μM) alters microglial morphology in TLR4 stimulated OHSCs independent of CB2

We went ahead to analyze microglial morphology in LPS/IFN-γ-stimulated OHSCs pre-treated with 1 μM SR144528 using the MotiQ plugin as described in (sections **3.2.4** and **2.14.3**) (**Figure 3.20A**).

Our results confirm that 1 μM of SR144528 significantly improves LPS/IFN-γ-induced ameboid-like microglial features in both WT and $CB2^{-/-}$ OHSCs. We found that 1 μM SR144528 increased branch number ($p_{(WT)}$ = 0.0019, $p_{(CB2^{-/-})}$ = 0.0277 (**Figure 3.20B+C**)), tree length ($p_{(WT)}$ = 0.0007, $p_{(CB2^{-/-})}$ = 0.0425 (**Figure 3.20B+D**))**,** ramification index ($p_{(WT)} < 0.001$, $p_{(CB2^{-/-})}$ = 0.0202 (**Figure 3.20B+E**)), surface ($p_{(WT)}$ = 0.0024, $p_{(CB2^{-/-})}$ = 0.0272 (**Figure 3.20B+F**)), and volume ($p_{(WT)}$ = 0.0015, $p_{(CB2^{-/-})}$ = 0.0451 (**Figure 3.19B+G**)) in both WT and $CB2^{-/-}$ OHSCs following LPS/IFN-γ stimulation. The polarity index did not change across groups.

This finding shows that 1 μM of SR144528 changes microglial morphology in both WT and $CB2^{-/-}$ OHSCs after LPS/IFN-γ stimulation

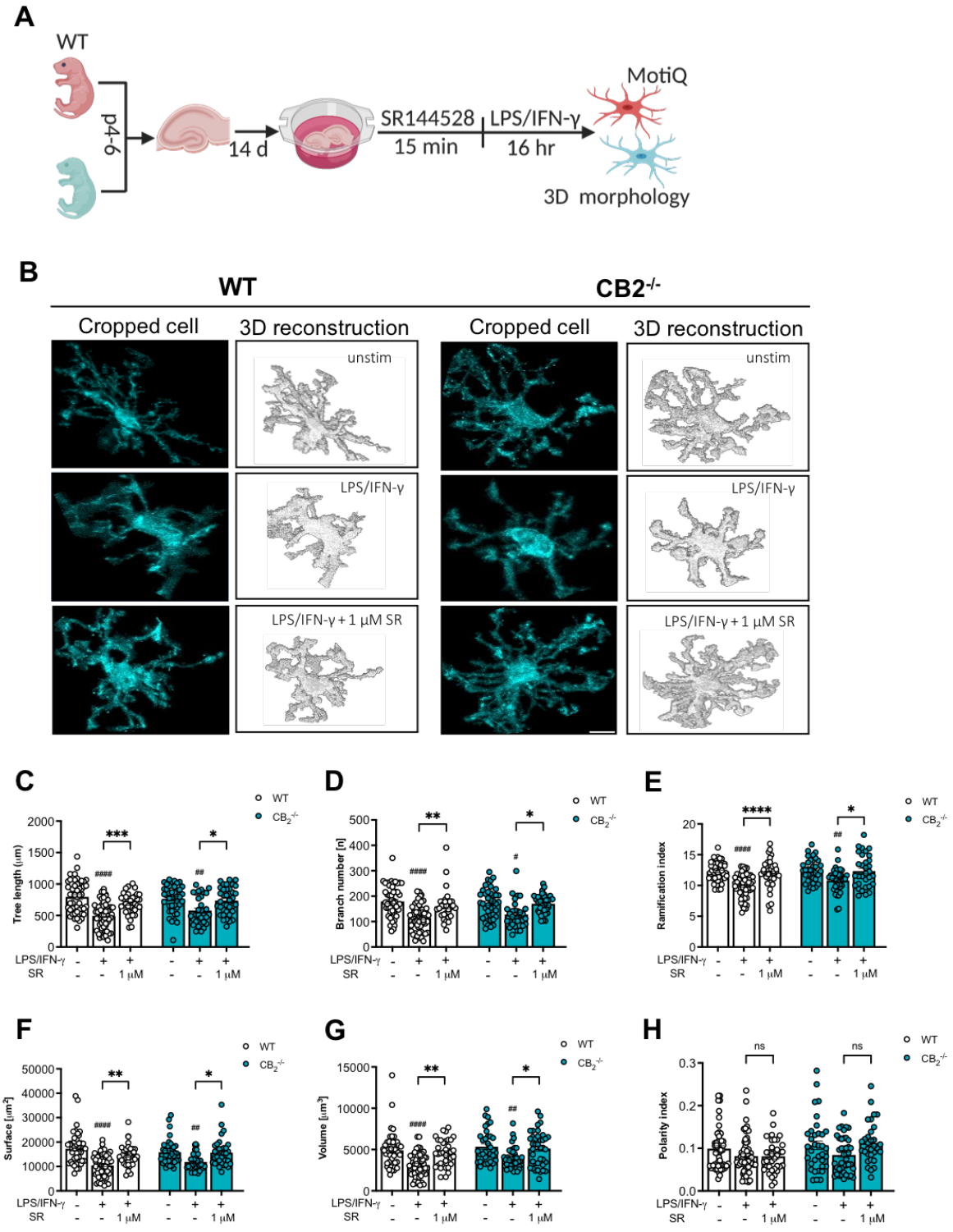

Figure 3.20: 1 μM of SR144528 altered TLR4-induced microglial morphology in a CB2 independent manner. (**A**) Experimental setup. Microglia morphology was analyzed using MotiQ plugin in Iba1 positive cells of WT and CB2$^{-/-}$ OHSCs pre-treated with 1 μM SR144528 (SR) for 15 min, followed by LPS/IFN-γ stimulation for 16 hr. (**B**) Representative images of cropped and 3D reconstructed microglia. Scale bar = 30 μm. (**C-H**) Quantification of morphological parameters of reconstructed microglia. (**C**) Branch

number, (**D**) Tree length, (**E**) Ramification index, (**F**) Surface, (**G**) Volume, and (**H**) Polarity index. N ≥ 40 microglial cells /stimulation (representative data from 2 independent OHSCs preparations). Data are presented as mean ± SEM. Two-way ANOVA followed by Sidak's multiple comparisons was used for normally distributed data. For data that were not normally distributed, Kruskal –Wallis test followed by Dunn's multiple comparisons tests was used. #### $p < 0.0001$, ## $p < 0.01$, # $p < 0.05$ indicate significance to the untreated control group. Significant differences between LPS/IFN-γ vs. LPS/IFN-γ pre-treated with 1 μM SR144528 are indicated as **** $p < 0.0001$, *** $p < 0.001$, ** $p < 0.01$, * $p < 0.05$.

3.2.11 SR144528 (at 1 μM) has no effect on cell death and cell surface maker expression in TLR4 stimulated microglia

Having established that 1 μM of SR144528 modulates LPS/IFN-γ-induced microglial cytokine secretion, activity and morphology independent of CB2 receptors, we next asked the following questions. On the one hand, we wanted to test whether the suppression of microglial activation by 1 μM SR144528 results from cell death in the microglial population. On the other hand, we asked if 1 μM of SR144528 influenced inflammatory cell surface marker expression in LPS/IFN-γ-stimulated primary microglia as observed in cytokine secretion. To investigate this, we pre-treated WT microglia with 1 μM SR144528 for 15 min followed by LPS/IFN-γ-stimulation for 16 hr. Using flow cytometry, dead cells were stained with DRAQ7™ and the percentage of live microglial cells was quantified. Cell surface markers expression was additionally analyzed in the stimulated microglia as geometric mean fluorescence intensity (gMFI) (**Figure 3.21A**).

LPS/IFN-γ stimulation caused a significant reduction ($p = 0.0019$) in the percentage of live microglial cells, which was not altered by 1 μM SR144528 pre-treatment (**Figure 3.21B+D**). We also observed a significant increase ($p < 0.0001$) in the expression of cell surface makers CD40 (cluster of differentiation 40, (**Figure 3.21C+E**)) and ICAM-1 (intercellular adhesion molecule 1 (**Figure 3.21C+F**)) in the LPS/IFN-γ-stimulated microglia. However, pre-treatment with 1 μM SR144528 failed to produce any significant change in the tested surface marker expressions.

Taken together, 1 μM SR144528 did not alter inflammatory cell surface marker expression in LPS/IFN-γ-stimulated microglia. More so, the significant cytokine decrease observed in LPS/IFN-γ-stimulated microglia pre-treated with 1 μM SR144528 was not caused by cell death.

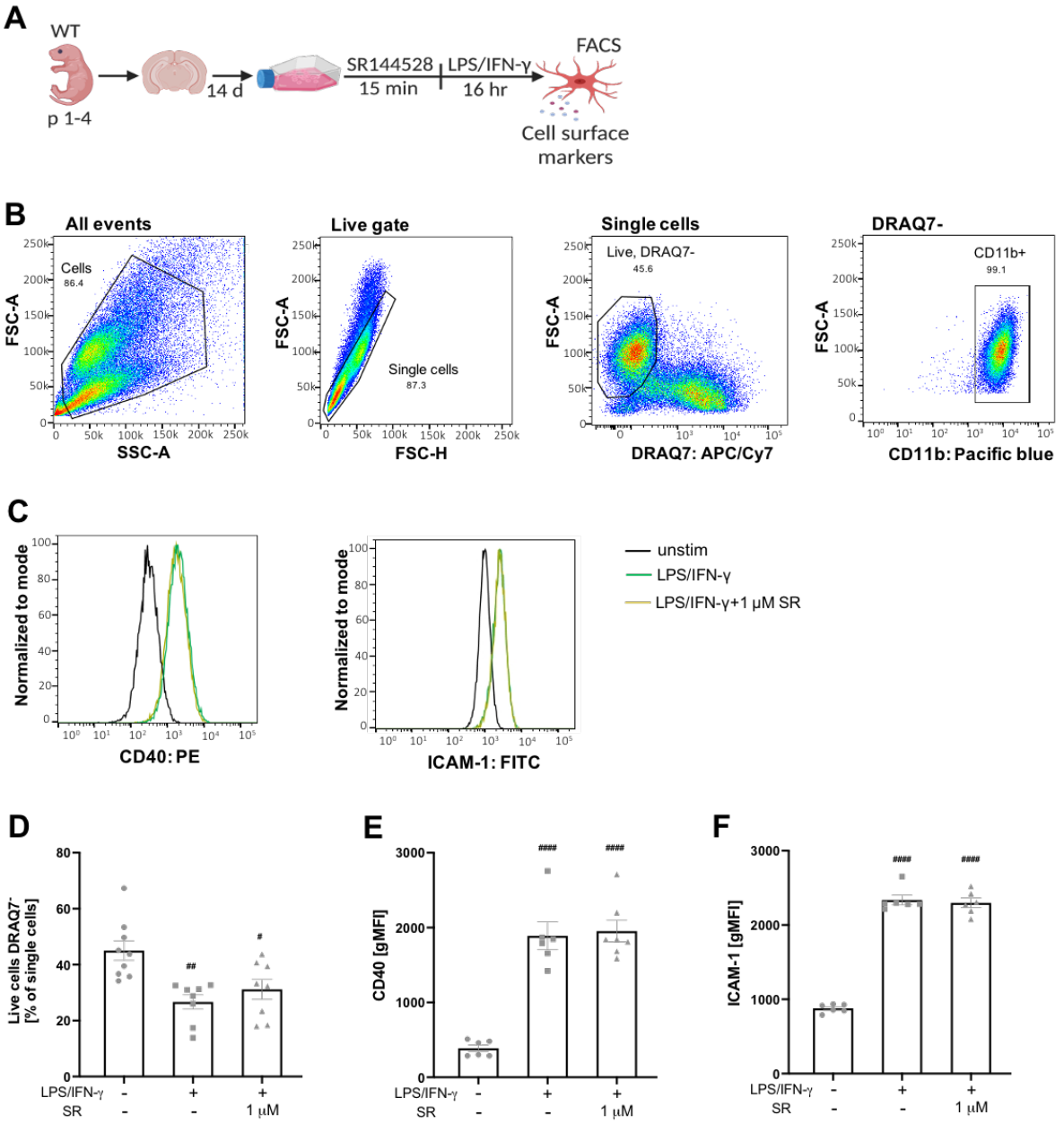

Figure 3.21: 1 μM of SR144528 neither affects cell death nor cell surface markers expression in TLR4 stimulated microglia. (**A**) Experimental setup. Flow cytometry analysis was performed in WT microglia pre-treated with 1 μM SR144528 (SR) for 15 min, followed by LPS/IFN-γ stimulation for 16 hr. (**B**) Gating strategy for stimulated microglia. DRAQ7™ was used to stain dead cells. $CD11b^+$ were identified as microglia (**C**) Representative histograms of cell surface markers on $CD11b^+$ stimulated microglia. (**D**) % live microglia cells. gMFI (Geometric mean fluorescent intensity) of (**E**) CD40 (**F**) ICAM-1. N = 6 - 9 samples/stimulation (representative from at least two independent preparations. Data are presented as mean ± SEM. One-way ANOVA followed by Sidak's multiple comparisons. #### $p < 0.0001$, ## $p < 0.01$, # $p < 0.05$ indicate significance to the untreated control group.

3.2.12 Effect of CB2 activation on LPS/IFN-γ-induced microglial cytokine secretion

The next direction we followed in this project was to determine the influence of CB2 activation on LPS/IFN-γ-mediated microglial cytokine secretion. Since numerous studies have reported CB2 agonists also exhibit an anti-inflammatory effect during microglial activation, we wondered if this effect occurred at nanomolar concentrations in our hands. To investigate this, we used the CB2-specific agonist JWH-133 with Ki of 3.4 nM. We pre-treated WT microglia with increasing concentrations of JWH-133 (10 nM – 1 μM) for 15 min, after which we stimulated with LPS/IFN-γ for 16 hr. We then measured cytokine levels in the supernatants of the stimulated microglia using ELISA (**Figure 3.22A**).

As expected, we observed that JWH-133 decreased LPS/IFN-γ-induced TNF-α ($p_{(10\ nM)}$ = 0.0299, $p_{(100\ nM)}$ = 0.0064, $p_{(1\ \mu M)}$ = 0.0021) and IL-6 ($p_{(10\ nM)}$ = 0.0497, $p_{(100\ nM)}$ = 0.0161, $p_{(1\ \mu M)}$ = 0.0027) secretion in all the tested concentrations. CCL2 on the hand was significantly decreased only at 100 nM (p = 0.0229) and 1 μM (p = 0.0038).

These findings showed the efficacy of JWH-133 at nanomolar concentrations.

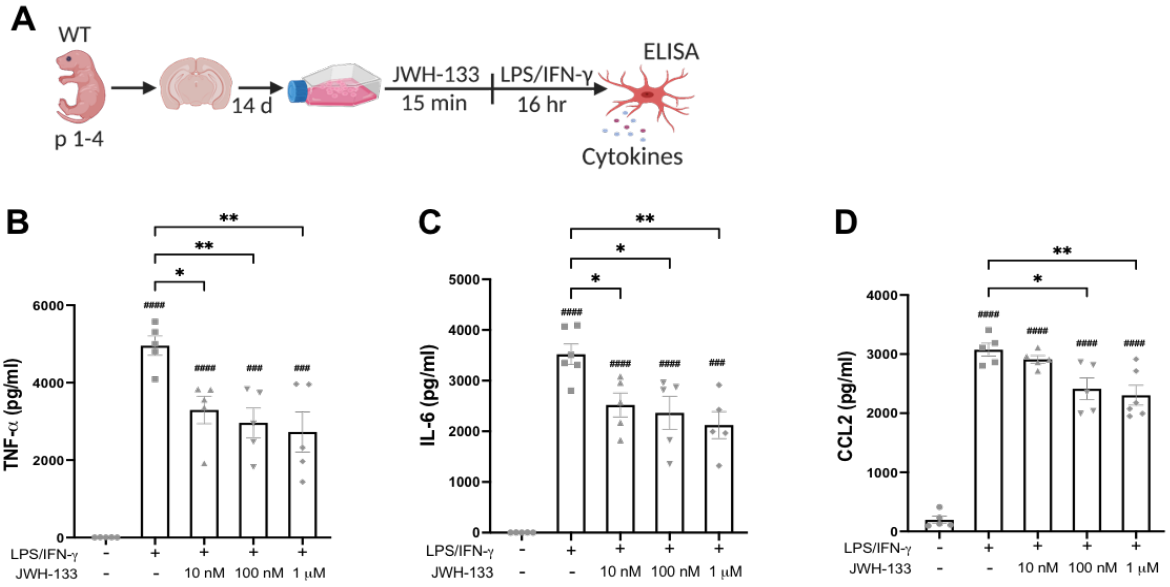

Figure 3.22: JWH-133 reduced LPS/IFN-γ-induced microglial cytokine/chemokine secretion only at nanomolar concentrations. (**A**) Experimental setup. Levels of cytokines/chemokines were measured in supernatants of microglia pre-treated with JWH-133 at the indicated concentrations, followed by LPS/IFN-γ stimulation for 16 hr. (**B**) TNF-α, (**C**) IL-6, and (**D**) CCL2. N = 5 - 6 samples/stimulation from two independent preparations. Data are presented as mean ± SEM. One-way ANOVA followed by Sidak's multiple comparisons. #### p < 0.0001, ### p < 0.001 indicate significance to the untreated control group. Significant differences between LPS/IFN-γ vs. LPS/IFN-γ pre-treated with JWH-133 are indicated with ** p < 0.01, * p < 0.05.

3.3 Role of CB2 in LPS/IFN-γ-induced metabolic reprogramming in microglia (Pharmacological inhibition vs CB2 knockout studies)

3.3.1 CB2$^{-/-}$ microglia show improved maximal respiration before and after LPS/IFN-γ stimulation

The last set of hypotheses tested in this project aimed to investigate the effect of CB2 on metabolic changes in LPS/IFN-γ-stimulated microglia. During inflammatory stimulation, immune cells are known to undergo a metabolic shift from oxidative phosphorylation (mitochondria) to glycolysis (cytosol). Therefore, we first assessed seahorse metabolic parameters in WT and CB2$^{-/-}$ microglia after 16 hr of LPS/IFN-γ stimulation using XFe96 analyzer (**Figure 3.23A**). Overview of metabolic analysis is displayed in **Figure 3.23B.** Detailed experimental protocol is explained in (section **2.23**).

After glucose injection, we observed an increased extracellular acidification rate (ECAR) in both WT ($p = 0.0224$) and CB2$^{-/-}$ ($p = 0.0221$) microglia stimulated with LPS/IFN-γ (**Figure 3.23C+E**), suggesting that glycolytic switch generally occurs in inflammatory microglia with or without CB2. Interestingly, oxygen consumption rate was increased in unstimulated CB2$^{-/-}$ microglia ($p = 0.0454$) as well as LPS/IFN-γ stimulated CB2$^{-/-}$ microglia ($p = 0.0421$) after sequential addition of FCCP in comparison to the WT (**Figure 3.23D+H**). This data suggests that the CB2 deletion improves maximal respiratory capacity in both unstimulated and activated microglia. Furthermore, we found a significant increase in basal respiration of CB2$^{-/-}$ microglia ($p = 0.0357$) when compared to the WT after LPS/IFN-γ stimulation (**Figure 3.23D+F**). We report no significant difference in ATP-linked respiration across all the groups (**Figure 3.23D+G**).

Altogether, CB2 deletion has no significant effect on ECAR in LPS/IFN-γ stimulated microglia, but enhances maximal respiration capacity in unstimulated LPS/IFN-γ stimulated microglia.

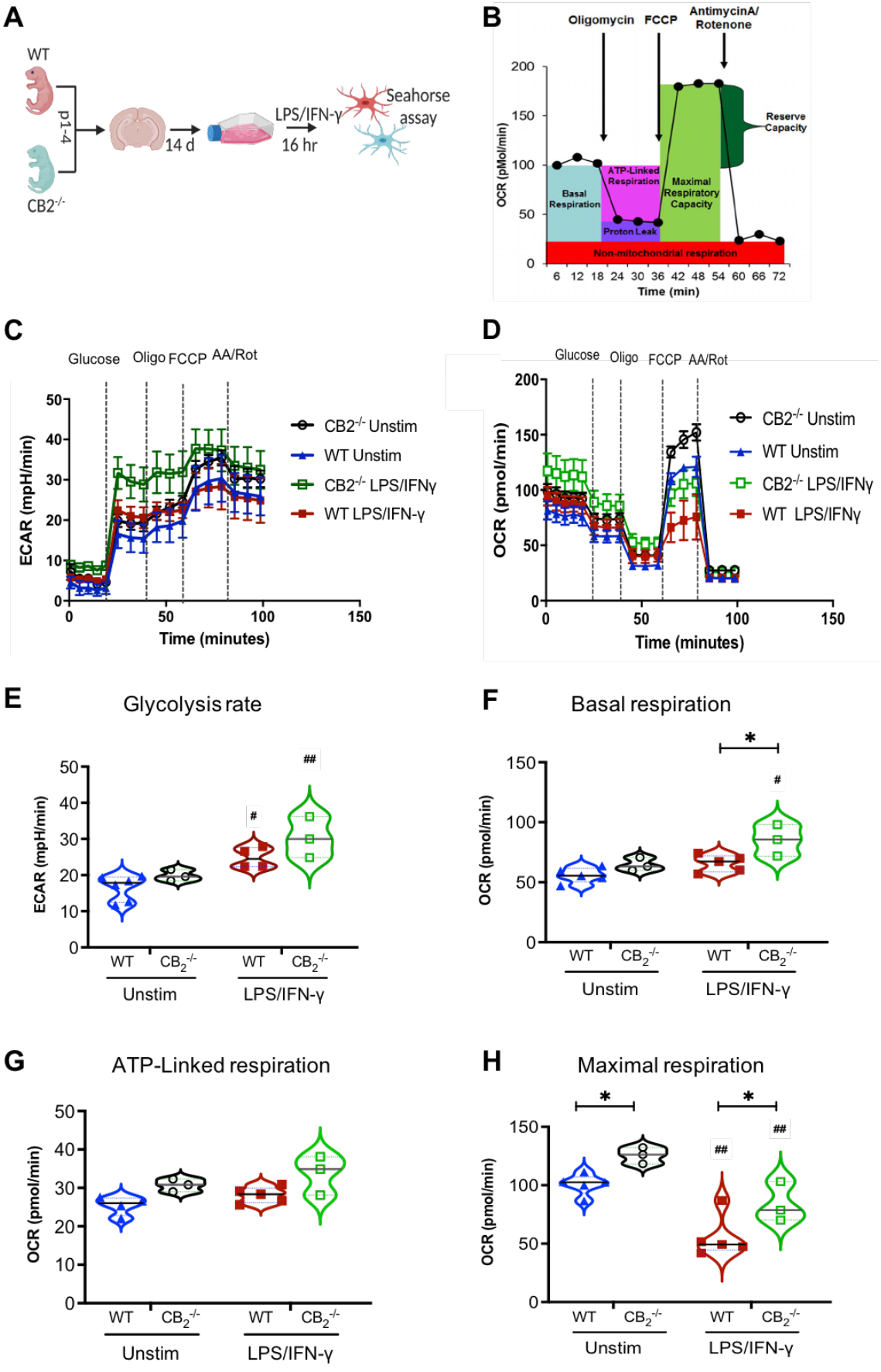
A
WT
p1-4
CB2-/-
14 d
LPS/IFN-γ
16 hr
Seahorse assay
B
Oligomycin
FCCP
AntimycinA/ Rotenone
OCR (pMol/min)
Basal Respiration
ATP-Linked Respiration
Proton Leak
Maximal Respiratory Capacity
Reserve Capacity
Non-mitochondrial respiration
Time (min)
C
Glucose
Oligo
FCCP
AA/Rot
ECAR (mpH/min)
CB2-/- Unstim
WT Unstim
CB2-/- LPS/IFNγ
WT LPS/IFN-γ
Time (minutes)
D
Glucose
Oligo
FCCP
AA/Rot
OCR (pmol/min)
CB2-/- Unstim
WT Unstim
CB2-/- LPS/IFNγ
WT LPS/IFNγ
Time (minutes)
E
Glycolysis rate
ECAR (mpH/min)
WT
CB2-/-
Unstim
LPS/IFN-γ
F
Basal respiration
OCR (pmol/min)
G
ATP-Linked respiration
H
Maximal respiration

Figure 3.23: Seahorse metabolic analysis from WT and CB2$^{-/-}$ microglia after LPS/IFN-γ stimulation. (**A**) Experimental setup. Seahorse metabolic parameters were measured in WT and CB2$^{-/-}$ microglia stimulated with LPS/IFN-γ for 16 hr. (**B**) Overview of seahorse mitochondrial respiration analysis after the sequential addition of mitochondrial component inhibitors; oligomycin, FCCP and antimycin & rotenone {AA/Rot} (Agilent Seahorse XFe96 analyzer). (**C**) Extracellular acidification rate, ECAR measurement in stimulated microglia after the sequential addition of glucose, oligomycin, FCCP and AA/Rot (**D**) Oxygen consumption rate, OCR measurement in stimulated microglia after the sequential addition of inhibitors as in C. Quantification of (**E**) ECAR after glucose injection, (**F**) Basal respiration before glucose injection, (**G**) ATP-linked respiration after oligomycin injection and (**H**) Maximal respiration after FCCP injection. N = 3 - 6 samples /genotype/ stimulation (representative from two independent experiments). Data are displayed as median (full line) with 25 and 75 percentiles (dotted lines). Two-way ANOVA followed by Sidak's multiple comparisons. Significant differences between WT and CB2$^{-/-}$ are indicated with * $p < 0.05$. Significance to the unstimulated genotype control are indicated as ## $p < 0.01$, # $p < 0.05$.

3.3.2 CB2$^{-/-}$ macrophages show similar metabolic activity as in WT macrophages after LPS/IFN-γ stimulation

After observing CB2-specific metabolic signatures in the primary microglia, we also assessed the influence of CB2 on metabolic changes in BMDMs. We carried out seahorse analysis as described in 3.3.1 in LPS/IFN-γ stimulated BMDMs (**Figure 3.24A**).

Our ECAR results revealed a marked increase in glycolysis rate after LPS/IFN-γ stimulation in WT BMDMs ($p = 0.0339$), which was not significantly affected in CB2$^{-/-}$ BMDMs (**Figure 3.24B+D**). All OCR data similarly showed no significant difference between WT and CB2$^{-/-}$ BMDMs after LPS/IFN-γ stimulation (**Figure 3.24E-G**). We only observed a decreased stimulation effect in both WT ($p < 0.001$ for all parameters) and CB2$^{-/-}$ ($p_{(basal\ respiration)} = 0.0006$, $p_{(ATP\text{-}linked\ respiration)} = 0.0005$, $p_{(maximal\ respiration)} < 0.001$) BMDMs during the inflammatory stimulation (**Figure 3.24B+D**).

These data summarily pinpoint that the peripheral BMDMs from CB2$^{-/-}$ mice did not show improved maximal respiration with or without LPS/IFN-γ stimulation compared to the WT BMDMs.

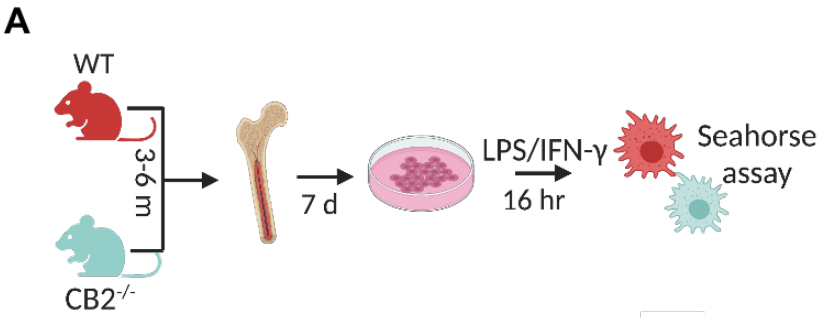
A
WT
3-6 m
CB2-/-
7 d
LPS/IFN-γ
16 hr
Seahorse
assay

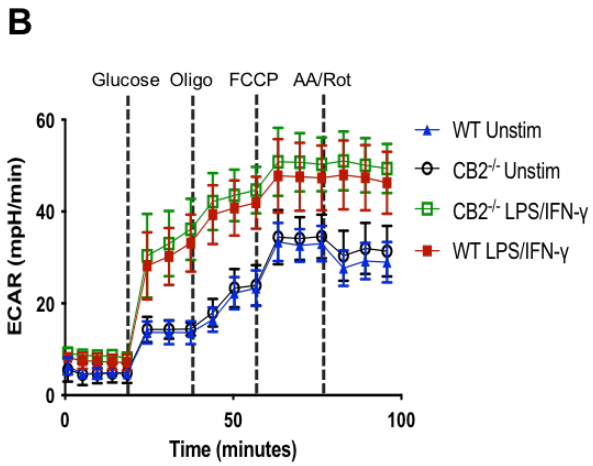
B
Glucose
Oligo
FCCP
AA/Rot
ECAR (mpH/min)
Time (minutes)
WT Unstim
CB2-/- Unstim
CB2-/- LPS/IFN-γ
WT LPS/IFN-γ

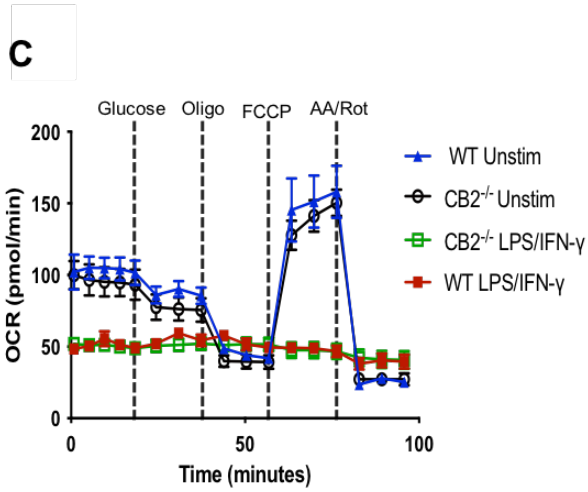
C
Glucose
Oligo
FCCP
AA/Rot
OCR (pmol/min)
Time (minutes)
WT Unstim
CB2-/- Unstim
CB2-/- LPS/IFN-γ
WT LPS/IFN-γ

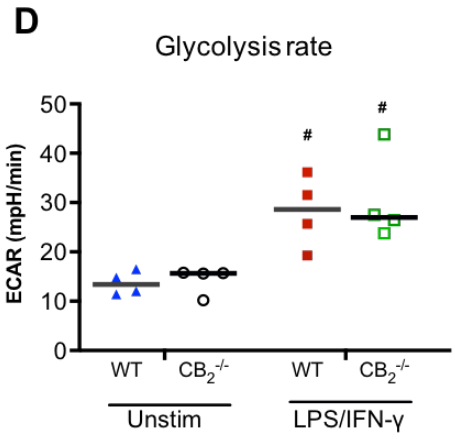
D
Glycolysis rate
ECAR (mpH/min)
WT
CB2-/-
WT
CB2-/-
Unstim
LPS/IFN-γ

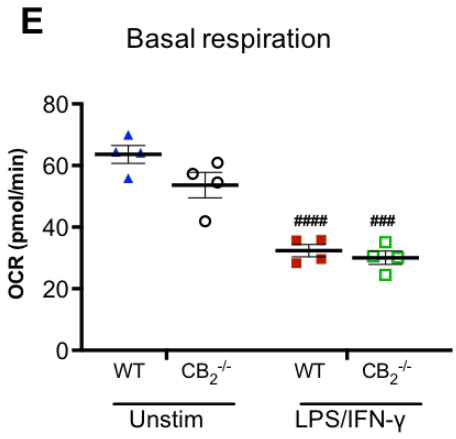
E
Basal respiration
OCR (pmol/min)
WT
CB2-/-
WT
CB2-/-
Unstim
LPS/IFN-γ

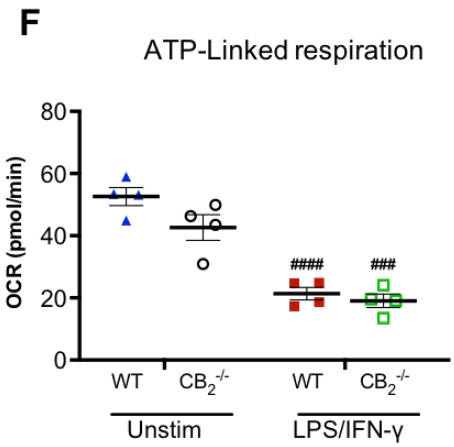
F
ATP-Linked respiration
OCR (pmol/min)
WT
CB2-/-
WT
CB2-/-
Unstim
LPS/IFN-γ

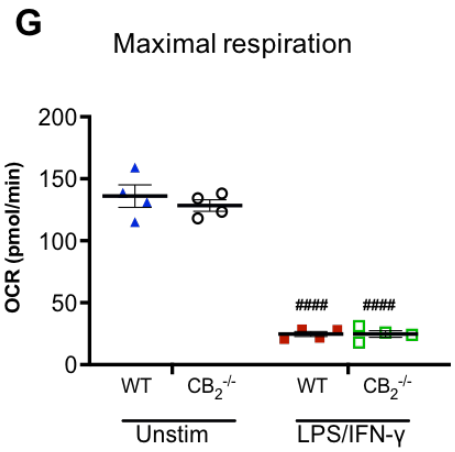
G
Maximal respiration
OCR (pmol/min)
WT
CB2-/-
WT
CB2-/-
Unstim
LPS/IFN-γ

Figure 3.24: Seahorse metabolic analysis from WT and CB2$^{-/-}$ Bone marrow-derived macrophages after LPS/IFN-γ stimulation. (**A**) Experimental setup. Seahorse metabolic parameters were measured in WT and CB2$^{-/-}$ BMDMs stimulated with LPS/IFN-γ for 16 hr. ECAR and OCR measurements were recorded in BMDMs after the sequential addition of mitochondrial component inhibitors; oligomycin, FCCP and antimycin & rotenone (AA/Rot) using Agilent Seahorse XFe96 analyzer. (**B**) Extracellular acidification rate, ECAR measurement in stimulated BMDMs after the sequential addition of the inhibitors stated in A (**C**) Oxygen consumption rate, OCR measurement in stimulated BMDMs after the sequential addition of inhibitors as in A. Quantification of (**D**) ECAR after glucose injection, (**E**) Basal respiration before glucose injection, (**F**) ATP-linked respiration after oligomycin injection and (**G**) Maximal respiration after FCCP injection. N = 4 samples /genotype/ stimulation (representative from two independent experiments). Data are presented as mean ± SEM. Two-way ANOVA followed by Sidak's multiple comparisons. Significance to the unstimulated genotype control are indicated as #### $p < 0.0001$, ### $p < 0.001$, # $p < 0.05$.

3.3.3 SR144528 (at 1 μM) marginally influences seahorse metabolic activity in LPS/IFN-γ stimulated microglia

To compare the metabolic effect of CB2 knockout to CB2 antagonist in LPS/IFN-γ induced metabolic reprogramming, we next pre-treated WT primary microglia with 1 μM SR144528 for 15 min, with or without LPS/IFN-γ stimulation for 16 hr (**Figure 3.25A**). Afterward, we performed seahorse metabolic analysis as in **3.3.2**.

1 μM SR144528 significantly decreased ECAR in LPS/IFN-γ microglia after glucose injection ($p < 0.0001$, **Figure 3.25B+D**), whereas OCR was not affected (**Figure 3.25C+E-G**). We report a significant decrease ($p < 0.0001$) in basal respiration, maximal respiration and ATP-linked respiration in LPS/IFN-γ stimulated microglia, which was not altered by 1 μM SR144528 pre-treatment. (**Figure 3.25E-D**).

Our data revealed that pre-treating primary microglia with 1 μM SR144528 did not alter OCR parameters during inflammatory stimulation with LPS/IFN-γ. It however decreased ECAR in LPS/IFN-γ stimulated microglia.


A
WT
p 1-4
14 d
SR144528
15 min
LPS/IFN-γ
16 hr
Seahorse
assay

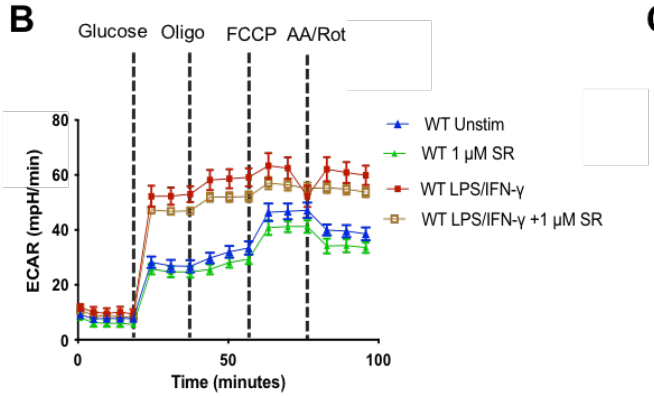
B
Glucose
Oligo
FCCP
AA/Rot
ECAR (mpH/min)
Time (minutes)
WT Unstim
WT 1 μM SR
WT LPS/IFN-γ
WT LPS/IFN-γ +1 μM SR

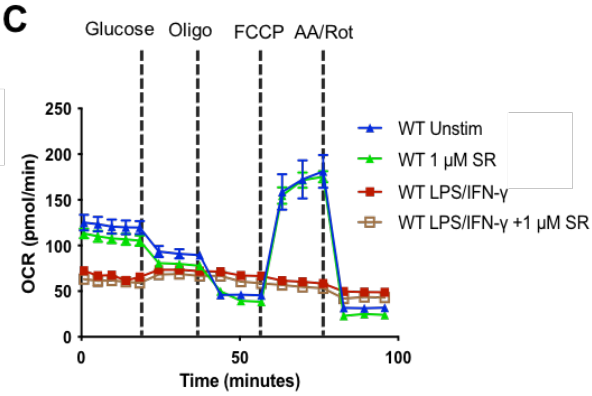
C
Glucose
Oligo
FCCP
AA/Rot
OCR (pmol/min)
Time (minutes)
WT Unstim
WT 1 μM SR
WT LPS/IFN-γ
WT LPS/IFN-γ +1 μM SR

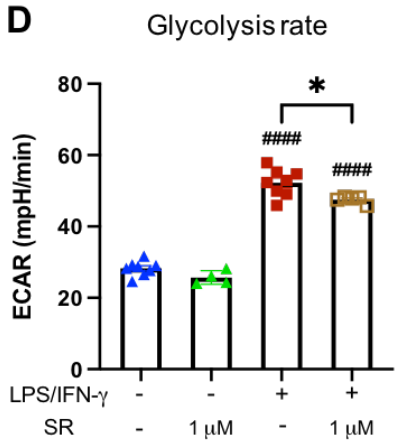
D
Glycolysis rate
ECAR (mpH/min)
*
####
####
LPS/IFN-γ
SR
1 μM
1 μM

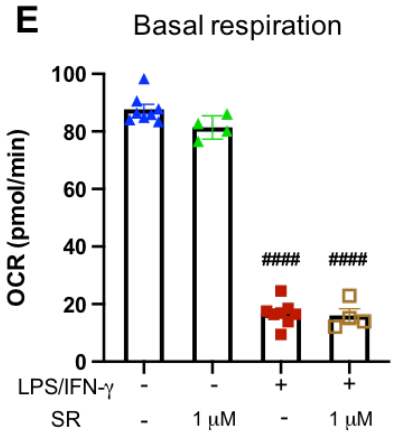
E
Basal respiration
OCR (pmol/min)
####
####
LPS/IFN-γ
SR
1 μM
1 μM

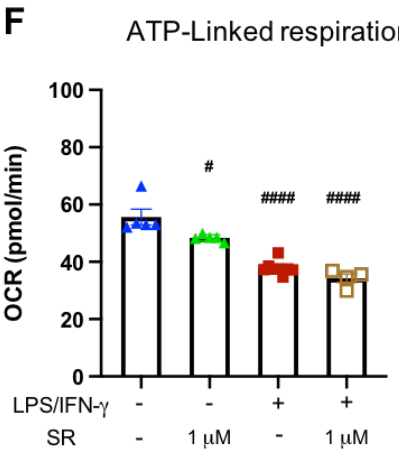
F
ATP-Linked respiration
OCR (pmol/min)
#
####
####
LPS/IFN-γ
SR
1 μM
1 μM

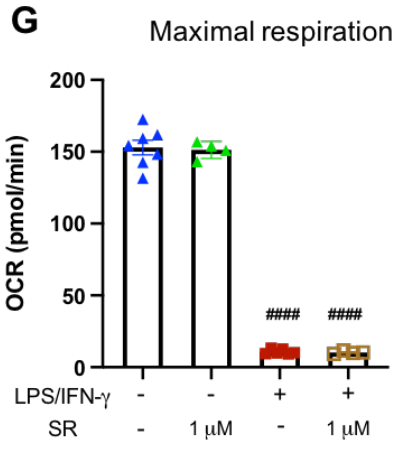
G
Maximal respiration
OCR (pmol/min)
####
####
LPS/IFN-γ
SR
1 μM
1 μM

Figure 3.25: Seahorse metabolic analysis from LPS/IFN-γ-stimulated WT microglia pre-treated with 1 μM SR144528. (**A**) Experimental setup. Seahorse metabolic parameters were measured in WT microglia pre-treated with 1 μM SR144528 (SR) for 15 min, followed by LPS/IFN-γ stimulation for 16 hr. ECAR and OCR measurements were recorded in microglia after the sequential addition of mitochondrial component inhibitors; oligomycin, FCCP and antimycin & rotenone (AA/Rot) using Agilent Seahorse XFe96 analyzer. (**B**) Extracellular acidification rate, ECAR measurement in stimulated microglia after the sequential addition of the inhibitors stated in A (**C**) Oxygen consumption rate, OCR measurement in stimulated microglia after the sequential addition of inhibitors as in A. Quantification of (**D**) ECAR after glucose injection, (**E**) Basal respiration before glucose injection, (**F**) ATP-linked respiration after oligomycin injection and (**G**) Maximal respiration after FCCP injection. N = 4-8 samples/genotype/stimulation (representative from two independent experiments). Data are presented as mean ± SEM. Two-way ANOVA followed by Sidak's multiple comparisons. Significance to the unstimulated control are indicated as #### $p < 0.0001$, ### $p < 0.001$, # $p < 0.05$. Significant difference between LPS/IFN-γ vs. LPS/IFN-γ pre-treated with 1 μM SR144528 is indicated as * $p < 0.05$.

3.3.4 SR144528 (at 1 μM) does not influence seahorse metabolic activity in LPS/IFN-γ stimulated Bone marrow-derived macrophages

Finally, we tested the effect 1 μM SR144528 pre-treatment on seahorse metabolic activity in LPS/IFN-γ-stimulated BMDMs. We pre-treated WT BMDMs with 1 μM SR144528 for 15 min, followed by LPS/IFN-γ stimulation for 16 hr. Experimental setup (**Figure 3.26A**). Seahorse metabolic analysis was performed as described in **3.3.1**.

Our ECAR data showed that glycolysis rate was significantly increased in LPS/IFN-γ-stimulated BMDMs after glucose injection ($p = 0.0006$, **Figure 3.26B+D**). However, pre-treatment with 1 μM SR144528 did not affect ECAR measurement in LPS/IFN-γ-stimulated BMDMs. In line with the ECAR result, OCR result revealed a significant decrease in basal respiration ($p < 0.0001$, **Figure 3.26C+E**), ATP-linked respiration ($p < 0.0001$, **Figure 3.26C+F**) and maximal respiration in LPS/IFN-γ-stimulated BMDMs ($p < 0.0001$, **Figure 3.26C+G**). This effect was not significantly altered by 1 μM SR144528 pretreatment. Additionally, we report no significant difference in the tested seahorse parameters between unstimulated BMDMs and those treated with 1 μM SR144528 alone (**Figure 3.26B-G**).

Taken together, we showed that the SR144528 did not significantly alter OCR and ECAR parameters in LPS/IFN-γ-stimulated BMDMs.

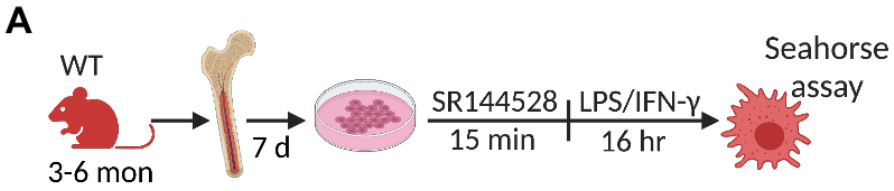
A
WT
3-6 mon
7 d
SR144528
15 min
LPS/IFN-γ
16 hr
Seahorse
assay

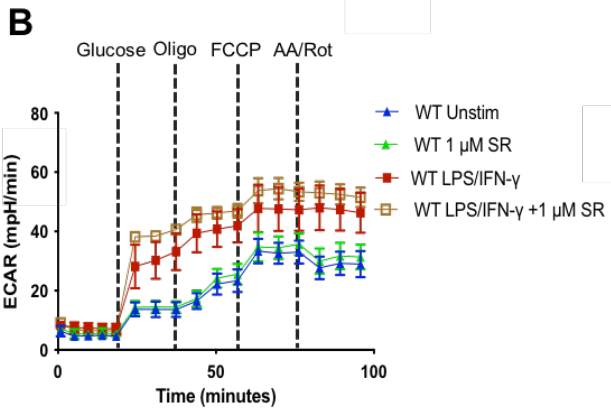
B
Glucose
Oligo
FCCP
AA/Rot
ECAR (mpH/min)
Time (minutes)
WT Unstim
WT 1 μM SR
WT LPS/IFN-γ
WT LPS/IFN-γ +1 μM SR

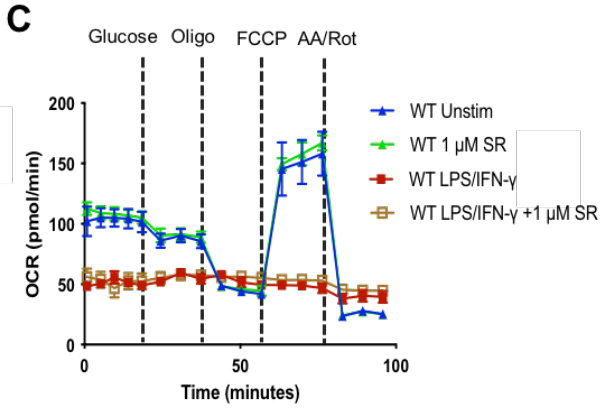
C
Glucose
Oligo
FCCP
AA/Rot
OCR (pmol/min)
Time (minutes)
WT Unstim
WT 1 μM SR
WT LPS/IFN-γ
WT LPS/IFN-γ +1 μM SR

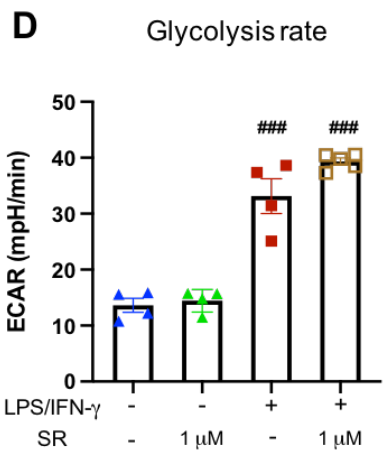
D
Glycolysis rate
ECAR (mpH/min)
###
###
LPS/IFN-γ
SR
1 μM
1 μM

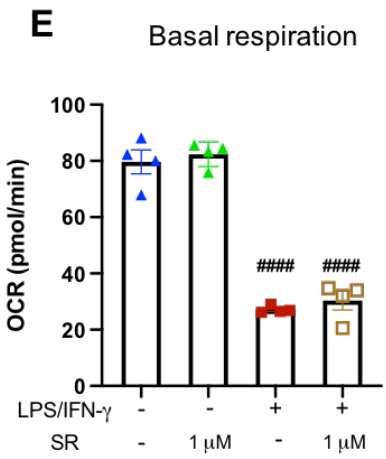
E
Basal respiration
OCR (pmol/min)
####
####
LPS/IFN-γ
SR
1 μM
1 μM

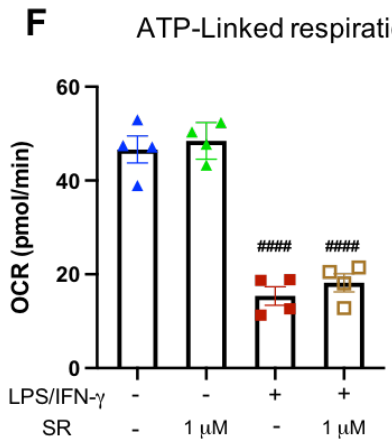
F
ATP-Linked respiration
OCR (pmol/min)
####
####
LPS/IFN-γ
SR
1 μM
1 μM

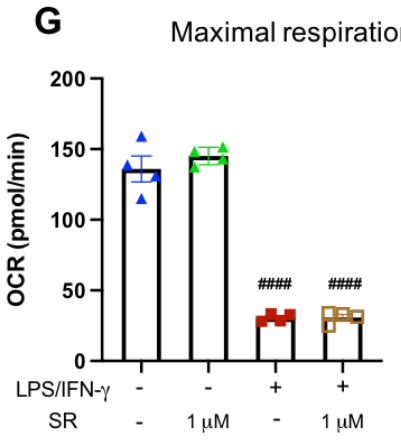
G
Maximal respiration
OCR (pmol/min)
####
####
LPS/IFN-γ
SR
1 μM
1 μM

Figure 3.26: Seahorse metabolic analysis from LPS/IFN-γ-stimulated WT BMDMs pre-treated with 1 μM SR144528. (**A**) Experimental setup. Seahorse metabolic parameters were measured in WT BMDMs pre-treated with 1 μM SR144528 (SR) for 15 min, followed by LPS/IFN-γ stimulation for 16 hr. ECAR and OCR measurements were recorded in BMDMs after the sequential addition of mitochondrial component inhibitors; oligomycin, FCCP and antimycin & rotenone {AA/Rot} using Agilent Seahorse XFe96 analyzer. (**B**) Extracellular acidification rate, ECAR measurement in stimulated BMDMs after the sequential addition of the inhibitors stated in A (**C**) Oxygen consumption rate, OCR measurement in stimulated BMDMs after the sequential addition of inhibitors as in A. Quantification of (**D**) ECAR after glucose injection, (**E**) Basal respiration before glucose injection, (**F**) ATP-linked respiration after oligomycin injection and (**G**) Maximal respiration after FCCP injection. N = 4 samples/genotype/stimulation (representative from two independent experiments). Data are presented as mean ± SEM. Two-way ANOVA followed by Sidak's multiple comparisons. Significance to the unstimulated control are indicated as #### $p < 0.0001$, ### $p < 0.001$.

4. Discussion

In this study, we aimed to deepen our understanding of the previously reported effects of CB2 receptors on TLR-induced microglial activation. Past studies from our lab demonstrated that CB2 deletion ($CB2^{-/-}$) suppresses microglial activation during inflammatory stimulation of TLRs or in neurodegenerative conditions (Schmöle et al., 2018; Schmöle, Lundt, Ternes, et al., 2015). Here, we demonstrated dampened inflammatory profile in $CB2^{-/-}$ microglia after TLR3/4 stimulation in a p38-dependent manner. We further compared the effects of genetic deletion of CB2 with acute pharmacological inhibition in response to TLR stimulation in microglia (**Figure 4.1**). We performed a secretory, mechanistic, metabolic, and morphological analysis of several aspects of microglial activation in primary microglia and OHSCs to investigate the goals mentioned above.

Our results showed that while $CB2^{-/-}$ microglia inhibits TLR3/4-induced microglial activation via p38 MAPK signaling, the pharmacological inhibition of CB2 with CB2-specific antagonist SR144528 did not recapitulate these results. We further showed that maximal respiration was already enhanced in $CB2^{-/-}$ microglia even before inflammatory stimulation. Thus, it is likely that the permanent lack of CB2 receptors initiated a compensatory mechanism that affects microglia metabolism and functions, making them less responsive to TLR stimulation. In addition, our data emphasize the potential off-target effects of SR144528 at micromolar concentrations.

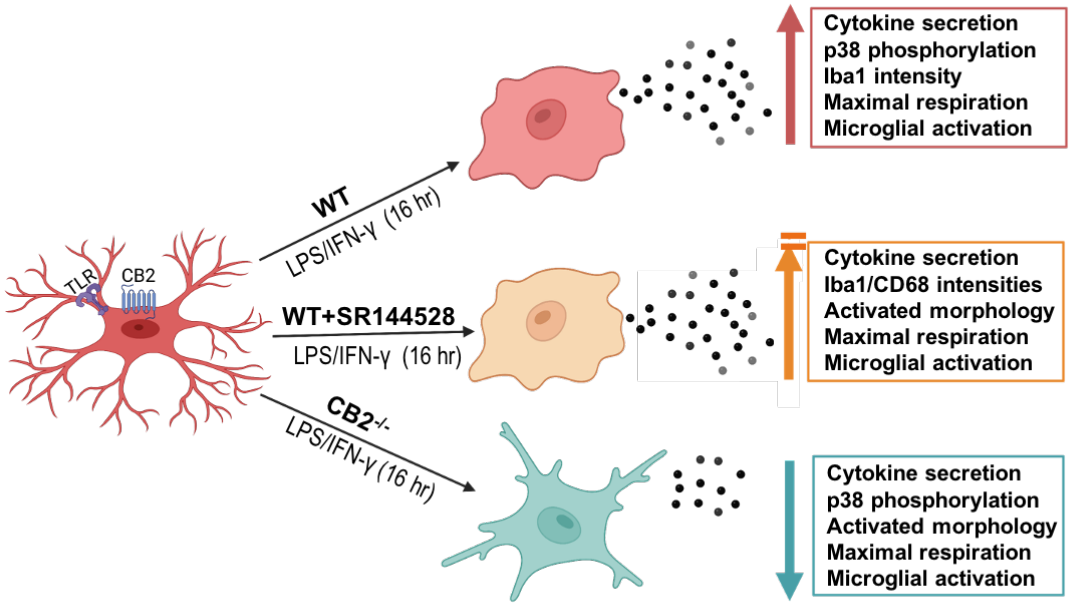

Figure 4.1: Overview of the differential effects of CB2 genetic deletion and pharmacological inhibition in TLR4-induced microglial activation.

↑ – increase parameters after LPS/IFN-γ stimulation

T – no effect of SR144528 on parameters in LPS/IFN-γ stimulated microglia

↓ – decrease parameters after LPS/IFN-γ stimulation compared to WT microglia

4.1 CB2 deletion decreases inflammatory profile in TLR-stimulated microglia

After stimulating WT microglia with TLR 3 (PolyI:C) and TLR 4 (LPS/IFN-γ) ligands, we observed a significant increase in the secretion of pro-inflammatory cytokines, which was significantly reduced in $CB2^{-/-}$ microglia. This finding is consistent with our previous *in vitro* and *in vivo* studies, which demonstrated that microglia from $CB2^{-/-}$ mice displayed lower inflammatory responses to LPS/IFN-γ and less activated microglia in APP/PS1 mouse model of AD (Schmöle et al., 2018; Schmöle, Lundt, Ternes, et al., 2015). However, in contrast to TLR3/4, TLR 9 stimulation with CpG did not significantly affect cytokine secretion in both WT and $CB2^{-/-}$ microglia. This situation could be partly attributed to the distinct MyD88 signaling pathway that CpG activates, which differs from the TRIF-dependent signaling that TLR3/4 pathways have in common (Duan et al., 2022a; Fiebich, Ribeiro et al., 2018).

Furthermore, Iba1 intensity notably increased after LPS/IFN-γ stimulation in WT microglia and was significantly reduced in $CB2^{-/-}$. This result provides additional evidence of dampened microglial activation in $CB2^{-/-}$ during inflammatory stimulation, which is in line with previous reports from $CB2^{-/-}$ OHSCs with decreased Iba1 levels (Reusch et al., 2022). Conversely, CB2 activation has also been shown to attenuate microglial activation during inflammation (Merighi et al., 2012; Molina-Holgado et al., 2003; Ma et al., 2015). For instance, CB2 agonists JWH-015 and AM1241 suppressed inflammatory responses to IFN-γ or LPS/IFN-γ stimulation in primary and N9 microglia respectively (Ma et al., 2015; Ehrhart et al., 2005). The less inflammatory effects of CB2 activation suggest that the absence of CB2 should lead to exacerbated microglial activation, which is not the case in our study.

Our findings of reduced microglial activation in $CB2^{-/-}$ microglia raised the question of whether acute pharmacological inhibition of CB2 differs from CB2 deletion with respect to modulating TLR-induced microglial activation. More so, we cannot draw a concrete conclusion without understanding the molecular mechanism by which CB2 deletion mediates the dampened inflammatory phenotype in TLR-stimulated microglia.

4.2 Molecular mechanism by which CB2 induce TLR-mediated microglial activation

The downstream pathways of CB2 signaling often involve the MAPK family members, ERK1/2, p38 MAPK, and PI3K/AKT or JAK/STAT signaling pathways (Bouaboula I et al., 1996; Capozzi et al., 2022; Montecucco et al., 2008). Here, we uncovered a possible underlying mechanism of suppressed microglial activation in $CB2^{-/-}$ microglia after TLR stimulation. We showed that p38 MAPK phosphorylation significantly increased after TLR3/TLR4 stimulation in WT microglia. However, we found a striking decrease in $CB2^{-/-}$ microglia compared to WT. This decreased phosphorylation was specific to p38 as the other MAPK member, ERK1/2 and additionally Akt and NF-κB were not significantly changed between WT and $CB2^{-/-}$ microglia stimulated with Poly I:C and LPS/IFN-γ. These data align with the previous study that showed that CB2 activation causes the induction of p38 MAPK in human leukaemia cells (Herrera et al., 2005).

Although a few studies reported that CB2 activation induces MAPK-phosphatase, which in turn dephosphorylates p38 MAPK (Zhou et al., 2007) and ERK1/2 (Romero-Sandoval et al., 2009), it is apparent from our study that p38 MAPK is necessary for CB2 signaling. Moreover, it has been widely reported that p38 MAPK is involved in LPS-induced cytokine release: IL-6 and TNF-α (Falcicchia et al., 2020; Shi et al., 2015). This data further corroborates our findings that CB2 indeed modulates TLR-induced microglial activation via p38 MAPK, as we found decreased phosphorylation and decreased cytokine production in the absence of CB2.

Taken together, our study places p38 MAPK at the crossroad between suppressed TLR3/4-induced microglial activation and CB2 deletion. Nevertheless, we cannot exclude the developmental effects of constitutive CB2 knockout, which might have triggered compensatory outcome in microglia. Hence, the need for pharmacological validation with CB2-specific antagonists.

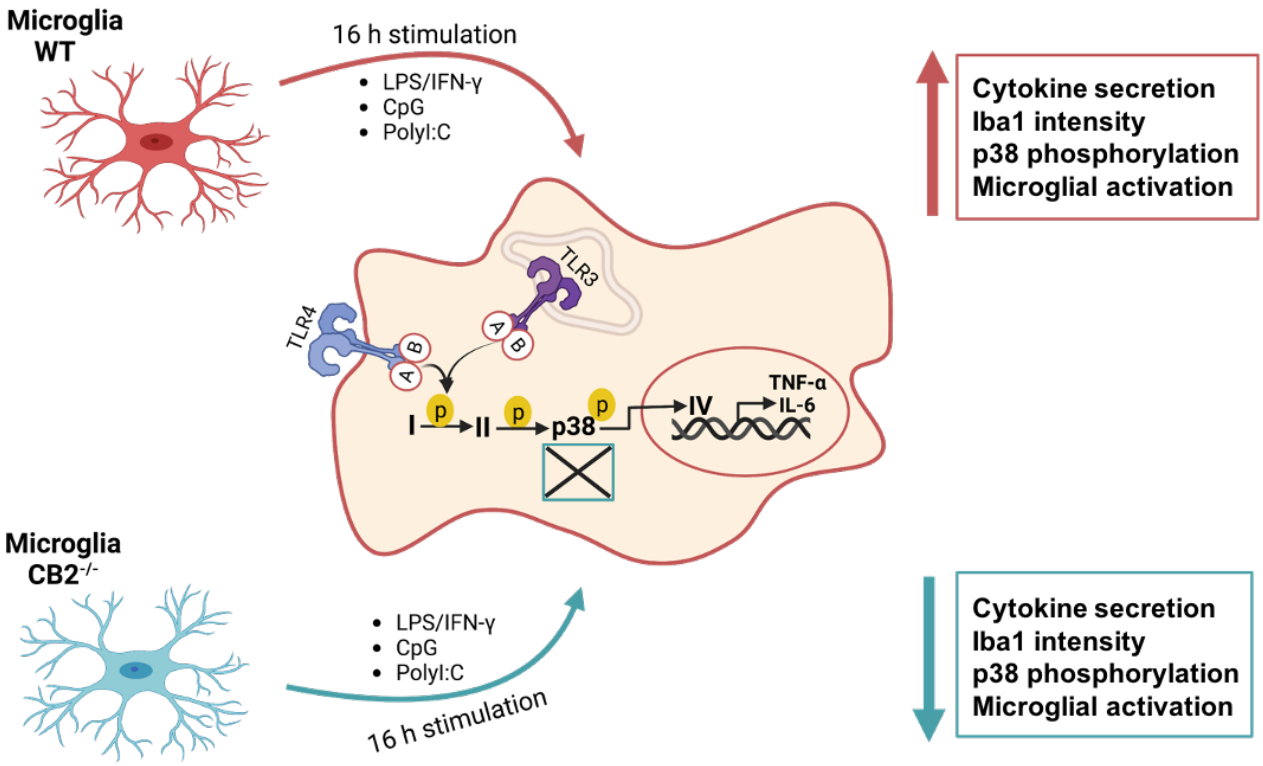

Figure 4.2: Interim summary of effects of CB2 deletion on TLR-induced microglial activation.

↑ – increase parameters after LPS/IFN-γ stimulation

↓ – decrease parameters after LPS/IFN-γ stimulation compared to WT

4.3 Pharmacological blockade of CB2 receptor does not affect TLR-induced microglial activation

We went ahead to assess the effect of pharmacological inhibition of CB2 on TLR-induced microglial activation. We analyzed several aspects of TLR-induced microglial activation in primary microglia and OHSCs pre-treated with SR144528. SR144528 is the most widely-used CB2 antagonist for pharmacological studies due to its high potency and selectivity for both mouse and human CB2 receptors (Rinaldi-Carmona et al., 1998; Soethoudt et al., 2017). It has been employed in numerous studies, often to block the effects of CB2 agonists (Correa et al., 2005, 2010a; Sacerdote et al., 2000). The required concentration to produce half its maximum inhibition (Ki) is 0.6 nM (Rinaldi-Carmona et al., 1998). This compound thus blocks CB2 receptors at low nanomolar concentrations.

In this study, we found that stimulation of WT microglia with TLR3/4 ligands increased production of inflammatory cytokines IL-6, TNF-α and CCL2. However, pre-treatment with 1 nM – 100 nM of SR144528 did not affect the secretion of these cytokines. This indicates that acute pharmacological inhibition of CB2 signaling does not modulate microglial response to LPS/IFN-γ and PolyI:C. This result was unexpected because our previous data from $CB2^{-/-}$ microglia showed a dampened inflammatory response to inflammatory stimuli (Reusch et al., 2022; Schmöle, Lundt, Ternes, et al., 2015).

Furthermore, SR144528 did not alter the staining intensities of microglial activation markersIba1 and CD68 in OHSCs. Iba1 is a microglia marker that is often increased during microglial activation (Reusch et al., 2022; Yousif et al., 2018), while CD68 is a lysosomal indicator of phagocytosis which is also enhanced during inflammation (Komorowska-Müller et al., 2021). The lack of SR144528 effect on these markers further suggests that acute inhibition of CB2 signaling does not modulate microglial activation.

Additionally, we employed a 3D reconstruction analysis (Hansen et al., 2022) to assess the microglial morphological changes in response to TLR3/TLR4 stimulation in OHSCs. It is of common notion that the shape of microglia can provide helpful information about their activation status; microglia transform from ramified to ameboid form during activation (Fernández-Arjona et al., 2019; He et al., 2021; Reusch et al., 2022; Yousif et al., 2018). Our results revealed that TLR3/4 stimulation of OHSCs resulted in activated morphological features characterized by fewer microglial branch number, shorter tree length, reduced ramification index, and decreased surface in the stimulated OHSCs, as

reported before (Reusch et al., 2022). However, pre-treatment with SR144528 did not produce a significant difference in all but one of these parameters, supporting its inability to prevent TLR3/4-induced microglial activation generally. Only the ramification index increased by 10 nM SR144528 from the parameters mentioned above. Besides the ramification index, we also observed that while the polarity index was not changed between untreated and LPS/IFN-γ stimulated OHSCs, the pre-treatment of SR144528 at 10 nM increased polarity index in LPS/IFN-γ stimulated OHSCs. The changes in these two parameters may indicate that either CB2 signaling has a distinct influence on these parameters or may reflect a particularly off-target effect.

Altogether, these results strongly indicate that acute pharmacological inhibition of CB2 signaling does not modulate microglial responses to TLR3/TLR4 stimulation. This was not what we assumed from our earlier data which showed that genetic deletion of CB2 suppresses TLR-induced microglial activation (Reusch et al., 2022; Schmöle, Lundt, Ternes, et al., 2015). Notwithstanding, it is important to note that it is not surprising that pharmacological inhibition and constitutive deletion of receptors can exhibit certain differences. One possible explanation for this discrepancy is that constitutive deletion is a long-term genetic alteration that can induce compensatory developmental changes (El-Brolosy & Stainier, 2017). Whereas pharmacological validation is mainly based on the specificity and selectivity of the pharmacological compound. Indeed, a few studies have reported differential effects of genetic deletion and pharmacological inhibition of proteins (Li et al., 2014; Román Darío et al., 2018). For example, soluble epoxide hydrolase inhibition and genetic deletion were shown to have opposing effects on cardiac fibrosis (Li et al., 2014), while another study demonstrated that the lysophosphatidate LPA_1 receptor antagonist Ki16425 did not totally mimic the results of the constitutive lack of LPA1 receptors on depression-like behavioral tests in mice (Román Darío et al., 2018).

Summarily, the findings from this study have important implications for the use of CB2 antagonists in pharmacological studies involving microglial activation. While SR144528 is considered the best CB2 antagonist available (Soethoudt et al., 2017), its lack of effect on TLR-induced microglial activation at nanomolar concentrations suggests that caution should be exercised when interpreting the results of studies that used this compound. Besides the points mentioned above, this study's findings highlight the

importance of using multiple endpoints and assays to assess microglial activation for better understanding the effect of CB2 on microglial response to inflammatory stimulation.

4.4 Pharmacological blockade of CB2 receptor does not affect TLR4-induced cytokine secretion in bone marrow-derived macrophages

We additionally examined the effects of SR144528 on LPS/IFN-γ-induced cytokine secretion in BMDMs, to determine whether the inability of SR144528 to modulate TLR-induced microglial activation is specific to microglia or is present in myeloid cells in general. Microglia originate from the yolk sac whereas BMDMs differentiate from the hematopoietic stem cells, so cell-specific effects may differ (Ginhoux & Prinz, 2015). We found that BMDMs from WT mice showed increased but less pronounced inflammatory cytokine secretion after TLR4 stimulation, as previously observed (Reusch et al., 2022). This effect was not affected by SR144528 pre-treatment at nanomolar concentrations. This finding further implies that the lack of influence from SR144528 on TLR4-induced microglial activation is at least in part, conserved in cells from the myeloid lineage. Moreover, the less pronounced effect of TLR-mediated cytokine secretion in WT BMDMs compared to microglia was already shown in our earlier study (Reusch et al., 2022), where we additionally reported reduced inflammatory phenotype in $CB2^{-/-}$ BMDMs.

To sum up, our data from BMDMs adds to the body of knowledge that SR144528 fails to modulate inflammatory responses to LPS/IFN-γ in brain resident microglia and peripheral macrophages. Hence, a general caution should be extended to these myeloid cells when using the SR144528 compound. Moreover, further investigation of SR144528's effect on other lymphocytes is required to fully understand the role of SR144528 in immune cells.

4.5 SR144528 (at 1 μM) reduced TLR4-induced microglial inflammatory cytokine secretion independent of the CB2 receptor

One interesting finding from this study is that with a higher concentration of SR144528 (at 1 μM), we found a significant reduction in LPS/IFN-γ-induced microglial activation in WT microglia. This is relevant because many pharmacological studies used SR144528 at 1 μM or higher to reverse the anti-inflammatory effect of CB2 agonists in inflammatory settings (Chiurchiù et al., 2014; Capozzi et al., 2022; Correa et al., 2005, 2010; Kishimoto

et al., 2004; Sacerdote et al., 2000). For instance, JWH-133 increased IL-10 secretion in macrophages stimulated with LPS/IFN-γ, which was blocked by SR144528 (Correa et al., 2005). While it seems conflicting that both agonists and antagonists of CB2 would suppress inflammatory activation of microglia, these findings would be in line with the observation of decreased TLR-induced inflammatory responses in $CB2^{-/-}$ microglia as earlier reported in this study and previous studies from our group (Reusch et al., 2022; Schmöle, Lundt, Ternes, et al., 2015). Nonetheless, 1 μM of SR144528 is relatively high compared to the concentration required for the blockade of 50 % CB2 receptors (0.6 nM). This led us to wonder whether the suppression of TLR4-induced microglial activation by 1 μM SR144528 was indeed CB2-independent.

Therefore, we pre-treated both WT and $CB2^{-/-}$ microglia with 1 μM of SR144528 followed by LPS/IFN-γ-stimulation. We found that 1 μM of SR144528 significantly reduced LPS/IFN-γ-induced release of TNF-α and IL-6 in both WT and $CB2^{-/-}$ microglia, and although the decrease in CCL2 secretion was not statistically significant in $CB2^{-/-}$ microglia, it is still indicative of the potential effect of SR144528. In addition, 1 μM of SR144528 significantly reduced activated microglial morphology, decreased Iba1 and CD68 intensities in both WT and $CB2^{-/-}$ OHSCs following LPS/IFN-γ stimulation. These results confirm that high concentrations of the CB2 antagonist SR144528 (at 1 μM) indeed suppressed TLR4-induced inflammatory cytokine production through a CB2-independent mechanism. Furthermore, we asked whether the reduced inflammatory responses to 1 μM SR144528 resulted from cell death in stimulated microglia since we used SR144528 at a high micromolar concentration. Our results revealed that although the amount of live cells reduced significantly in LPS/IFN-γ stimulated microglia, as reported by (Kacimi et al., 2011), this was not affected by 1 μM SR144528 pre-treatment. This finding indicates that cell death was not involved in 1 μM SR144528-mediated suppression of inflammatory profile in LPS/IFN-γ stimulated microglia. We further showed that, while 1 μM of SR144528 reduced inflammatory cytokine secretion and mimics the $CB2^{-/-}$ results in LPS/IFN-γ stimulated microglia, 1 μM of SR144528 seems not to alter inflammatory cell surface markers CD40 and ICAM-1 which contrast the $CB2^{-/-}$ data (Schmöle, Lundt, Ternes, et al., 2015). Nevertheless, the main focus here is that 1 μM of SR144528 reduced at least three aspects of microglial activation in a CB2 independent manner.

Even though SR144528 is considered an excellent CB2-specific antagonist, some off-target effects have been described at micromolar concentrations (Soethoudt et al., 2017). A CB2 ligand profiling study revealed some off-target activities of SR144528 on other proteins, namely adenosine A3 receptor (A_3AR) and phosphodiesterase 5 (Soethoudt et al., 2017). Moreover, SR144528 has been shown to inhibit the enzyme acyl CoA: cholesterol acyltransferase (ACAT) (Thewke et al., 2009). While our study did not explore the CB2-independent mechanisms of 1 μM SR144528 in microglia, it is possible that these off-targets might be involved. Previous studies have shown that the A_3AR agonist CI-IB-MECA has a pro-inflammatory effect on LPS-induced TNF-α secretion in peritoneal macrophages (Forte et al., 2011) and that inhibiting ACAT1 in macrophages overloaded with cholesterol produced a lower inflammatory profile (Melton et al., 2019). Together with our results, these findings emphasize that potential off-target effects of SR144528 could influence immune-modulatory functions at micromolar concentration. Therefore, these off-target effects should be taken into account when using SR14428 to inhibit CB2 signaling under inflammatory settings. Furthermore, future studies are needed to investigate how SR144528 (in terms of structural modification, type of inhibitions and mode of action) interacts with other targets to modulate immune processes.

Overall, the results presented so far in the study demonstrated that while low nanomolar concentrations of SR144528 do not modulate microglial responses to LPS/IFN-γ and PolyI:C, a high concentration at 1 μM suppressed LPS/IFN-γ-induced microglial activation in a CB2 independent manner. Conversely, our results from the CB2 knockout model suggested that CB2 deletion dampened microglial activation to TLR stimulation via the p38 MAPK signaling. However, this may be due to compensatory mechanism in $CB2^{-/-}$ microglia making them less responsive to inflammatory stimulation. We previously reported about 200 genes (including gene ontology terms for response to bacteria and viruses) that are differentially expressed between unstimulated WT and $CB2^{-/-}$ microglia (Reusch et al., 2022). Some of these genetic changes probably make $CB2^{-/-}$ microglia less sensitive to inflammatory stimulation.

4.6 Differential effects of CB2$^{-/-}$ and pharmacological inhibition on glucose metabolic parameters in TLR4-induced microglial activation

Based on the relationship between microglial activation and metabolic reprogramming, a metabolic shift occurs in activated microglia from mitochondrial oxidative phosphorylation to glycolysis (Lauro & Limatola, 2020; O'Neill et al., 2016). We hypothesized that CB2 modulates LPS/IFN-γ-induced microglial activation via the metabolic-inflammatory axis. We assessed the effect of CB2 deletion and CB2 antagonist SR144528 on seahorse metabolic parameters ECAR (extracellular acidification rate) and OCR (oxygen consumption rate) in TLR4-induced microglial activation as reported (Lauterbach et al., 2019). We observed a glycolytic switch after LPS/IFN-γ stimulation in WT microglia, as reported (Nair et al., 2019), characterized by increased ECAR. Yet, we found no difference in ECAR between WT and CB2$^{-/-}$ microglia. Interestingly, our OCR data showed that CB2 deletion specifically improved mitochondrial maximal respiration in unstimulated and LPS/IFN-γ stimulated microglia, suggesting that CB2$^{-/-}$ microglia have distinct respiration pattern even before exposure to LPS/IFN-γ.

The improved respiratory capacity in CB2$^{-/-}$ microglia in the absence of inflammatory stimuli is sustained in CB2$^{-/-}$ microglia stimulated with LPS/IFN-γ compared to their WT counterparts. While this improved maximal respiration would indicate a less inflammatory state that aligns with our previous results (Reusch et al., 2022; Schmöle, Lundt, Ternes, et al., 2015), the critical point here is that unstimulated microglia already have this pattern even before the stimulation. This finding suggests that CB2$^{-/-}$ microglia are metabolically wired differently, making them somewhat resistant to metabolic reprogramming during inflammatory stimulation.

On the other hand, pharmacological inhibition of CB2 with SR144528 did not significantly affect maximal respiration or OCR parameters tested after LPS/IFN-γ stimulation. This corroborates our results from the inflammatory cell surface markers where SR144528 did not alter inflammatory response after LPS/IFN-γ stimulation. Although 1μM SR144528 decreased ECAR measurement in LPS/IFN-γ stimulated microglia, this may be attributed to a particularly off-target effect of 1 μM SR144528.

Overall, this finding and the earlier results from this study reveal discrepancies between the effects of constitutive CB2 knockout and CB2 pharmacological inhibition in both TLR4-induced microglial activation and metabolic reprogramming, a phenomenon

associated with activated microglia. However, in this case, $CB2^{-/-}$ microglia evidently show a different metabolic pattern in the naïve state, suggesting that CB2 deletion might have induced some developmental changes in microglia, making them exhibit a different metabolic response to LPS/IFN-γ stimulation.

4.7 $CB2^{-/-}$ or pharmacological inhibition does not affect glucose metabolic parameters in TLR4-induced bone marrow-derived macrophages

Finally, we compared the effects of $CB2^{-/-}$ and SR144528 on glucose metabolic parameters in LPS/IFN-γ stimulated BMDMs. Previous observation showed a suppressed-inflammatory trend in $CB2^{-/-}$ microglia and $CB2^{-/-}$ BMDMs after LPS/IFN-γ stimulation (Reusch et al., 2022; Schmöle, Lundt, Ternes, et al., 2015), leading us to assume that this might also be true for seahorse metabolic parameters. However, our finding indicates that, unlike the $CB2^{-/-}$ microglia, maximal respiration in $CB2^{-/-}$ macrophages remain the same as WT before and after LPS stimulation. Furthermore, we found no significant difference between ECAR and other tested metabolic parameters: ATP-linked respiration and basal respiration between WT and $CB2^{-/-}$ before and after LPS stimulation. We only observed the glycolytic switch (Nair et al., 2019), evident by increased ECAR after LPS/IFN-γ stimulation with no genotype effect. The data indicate that the increased maximal respiration in $CB2^{-/-}$ microglia is specific to microglia and not in BMDMs.

In parallel with the pharmacological data from microglia, SR144528 did not affect maximal respiration or other seahorse parameters in LPS/IFN-γ stimulated macrophages. This result suggests that the lack of influence of SR144528 on LPS/IFN-γ-induced metabolic reprogramming also extends to BMDMs. Altogether, our findings indicate that both genetic deletion or pharmacological inhibition of CB2 does not affect LPS/IFN-γ-induced metabolic rewiring in BMDMs.

To summarize the seahorse metabolic data from both microglia and BMDMs, our data provide important insights into the role of CB2 in metabolic regulation and developmental changes, particularly in microglia than previously thought. On the other hand, our findings caution against the use of SR144528 as it may not be a promising compound for investigating the role of CB2 inhibition on LPS/IFN-γ-induced metabolic reprogramming in an inflammatory context.

4.8 Conclusions

This study revealed differential effects of constitutive CB2 knockout and pharmacological inhibition of CB2 in TLR-induced microglial activation. Where constitutive knockout models are important tools for understanding specific roles of genes and their underlying mechanisms in neuropathological or inflammatory conditions, the permanent lack of a protein can initiate adaptive developmental changes. It can thus be difficult to distinguish between direct effects due to the targeted gene deletion and indirect effects, requiring other means of functional gene or protein invalidation, such as pharmacological agonists and antagonists.

Here, we found that $CB2^{-/-}$ microglia produced lower inflammatory cytokines and decreased Iba1 intensity in response to TLR3/4-induced microglial activation. These data corroborates our previous studies, which showed that CB2 deletion suppressed microglial activation during inflammatory stimulation of TLRs or in APP/PS1 model of AD (Schmöle et al., 2018; Schmöle, Lundt, Ternes, et al., 2015). We further identified in this study a possible molecular mechanism by which CB2 deletion dampened inflammatory response to TLR stimulation via the p38 MAPK signaling. In contrast to $CB2^{-/-}$, pharmacological inhibition of CB2 with SR144528 at nanomolar concentration did not significantly change PolyI:C and LPS/IFN-γ-induced microglial cytokine secretion, Iba1/CD68 intensities or morphology in this study. These findings suggest that the former is not caused by an acute lack of CB2 signaling during stimulation, instead, perhaps $CB2^{-/-}$ microglia are primed differently, making them somewhat resistant to LPS/IFN-γ stimulation.

Although we reported a significant reduction in LPS/IFN-γ-induced microglial activation at 1 μM SRR144528, this effect was not CB2 dependent. Moreover, this concentration is relatively high compared to the Ki of SR144528, which is 0.6 nM. Therefore, caution should be exercised when using SR144528 in an inflammatory context, as its specificity for CB2 might have been lost at micromolar concentrations. Somewhat contradictory to our observations from $CB2^{-/-}$, CB2 activation with CB2 agonists also exhibited anti-inflammatory effects on microglia in during inflammatory stimulation (Ehrhart et al., 2005; Ma et al., 2015). Based on all these findings, it is evident that pharmacological activation/inactivation of CB2 and genetic manipulations can have different outcomes. Our $CB2^{-/-}$ results are most likely due to compensatory mechanisms, as we found a distinct metabolic pattern in unstimulated $CB2^{-/-}$ microglia compared to the

WT. The summary of the overall results obtained in this study is presented in **Figure 4.3**.

In conclusion, these findings point to a complex role of CB2 receptors in microglial development and function that goes beyond momentarily modulating TLR signaling and provide an explanation for the seeming contradiction of similar findings in $CB2^{-/-}$ mice and CB2 agonist treatments. Hence, future studies including cell type-specific models/ conditional knockout models are needed to comprehensively investigate the pharmacology and genetics of CB2 receptors in an inflammatory context.

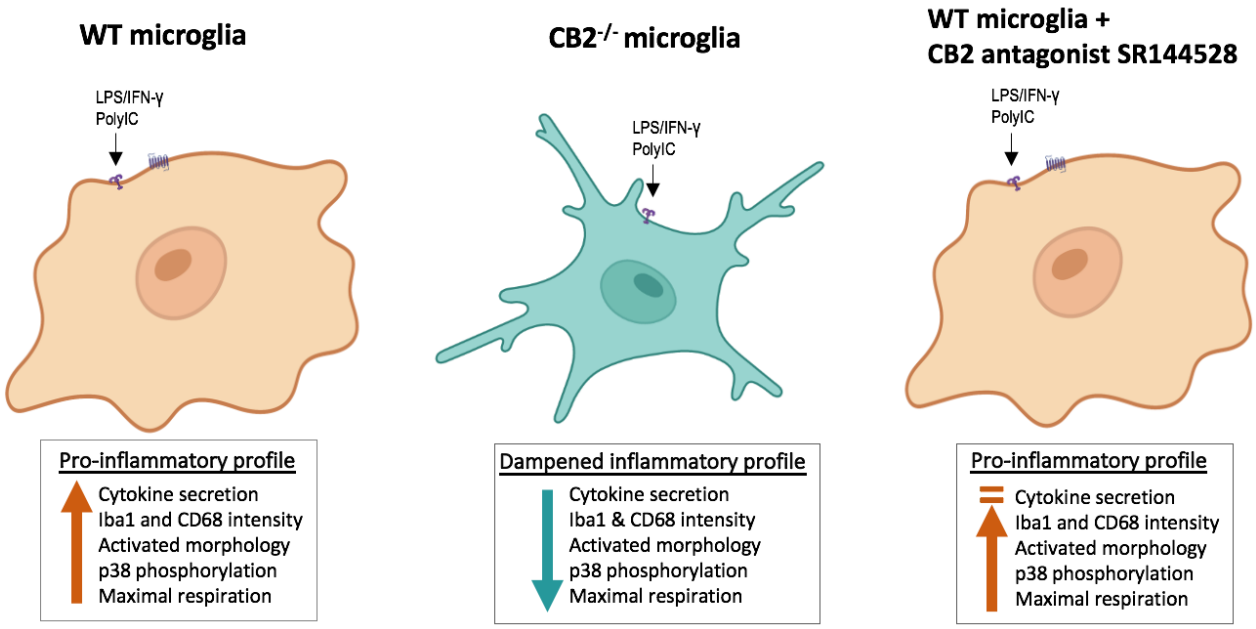

Figure 4.3: Summary of the comparative study between CB2 deletion and pharmacological inhibition in TLR4-induced microglial activation.

– increase parameters after LPS/IFN-γ stimulation

– decrease parameters after LPS/IFN-γ stimulation compared to WT

– no effect of SR144528 on parameters in LPS/IFN-γ stimulated microglia

5. Abstract

Cannabinoid receptor 2 (CB2) modulates microglial responses to inflammatory stimuli. Expression of CB2 is known to increase during chronic inflammation and thus exacerbate neurodegeneration. Results from previous studies in our lab demonstrated that genetic deletion of CB2 inhibits microglial activation during inflammatory stimulation of toll-like receptors (TLRs) or in neurodegenerative conditions. However, the molecular mechanism is unclear. More so, we cannot rule out the developmental effects of constitutive CB2 knockout, which could have triggered a compensatory outcome in $CB2^{-/-}$ mice. Therefore, in this study, we aimed to investigate, on the one hand, the molecular mechanism by which CB2 mediates TLR-induced microglial activation and on the other hand, to compare the effects of acute pharmacological inhibition of CB2 to $CB2^{-/-}$ in response to inflammatory stimulation of TLRs.

Our data showed that after TLR3 and TLR4 stimulation with PolyI:C and LPS/IFN-γ respectively in microglia, CB2 deletion caused decreased inflammatory cytokine secretion and reduced Iba1 intensity, whereas TLR9 stimulation with CpG did not affect the tested parameters in $CB2^{-/-}$ microglia compared to WT. We showed a striking decrease in p38 phosphorylation in $CB2^{-/-}$ microglia compared to WT after TLR3/4 stimulation. The pharmacological findings revealed that in contrast to $CB2^{-/-}$, CB2-specific antagonist SR144528 had little or no effect on TLR3/4-induced activation in primary microglia or organotypic hippocampal slice cultures at nanomolar concentrations (1 nM and 10 nM). We showed that SR144528 did not alter TLR-mediated microglial cytokine secretion, Iba1/CD68 staining intensities or morphology at nanomolar concentrations. Although SR144528 suppressed LPS/IFN-γ-induced microglial activation at 1 μM, this anti-inflammatory effect was not dependent on CB2 receptors and exceeded the Ki on CB2 receptors by more than a thousand-fold. Finally, our seahorse metabolic analysis indicated that $CB2^{-/-}$ alters metabolic rewiring in unstimulated and LPS/IFN-γ stimulated microglia, whereas CB2 blockade does not affect the metabolic effects.

Taken together, our findings suggest that pharmacological blockade of CB2 does not mimic the anti-inflammatory effects observed in the $CB2^{-/-}$ microglia after TLR stimulation. Therefore, we propose that the lack of CB2 receptors probably triggered an adaptive mechanism, making microglia less responsive to TLR stimulation.

6. List of figures

Figure 1.1: Origin of microglia from yolk sac progenitors

Figure 1.2: Microglia morphology in homeostatic and activated states

Figure 1.3: Toll-like receptor signaling pathway

Figure 1.4: Metabolic reprogramming during immune cell activation

Figure 1.5: CB2 receptor signaling pathway

Figure 1.6: Interplay between CB2 and TLR signaling

Figure 2.1: Overview of automated WES assay (proteinsimple)

Figure 2.2: Workflow of MotiQ morphology analysis of microglia

Figure 2.3: Overview of Seahorse mitochondrial respiration analysis

Figure 3.1: Inflammatory cytokine secretion from WT and $CB2^{-/-}$ microglia after TLR stimulation

Figure 3.2: Iba1 staining intensity in WT and $CB2^{-/-}$ microglia after TLR stimulation

Figure 3.3: ERK1/2 phosphorylation activity shows no significant difference between WT and $CB2^{-/-}$ microglia stimulated with TLR ligands

Figure 3.4: Akt phosphorylation activity shows no significant difference between WT and $CB2^{-/-}$ microglia after TLR stimulation

Figure 3.5: p38 but not NF-κB phosphorylation activity decreased significantly in $CB2^{-/-}$ microglia compared to WT after TLR3/4 stimulation

Figure 3.6: SR144528 reduced TLR4-mediated microglial cytokine/chemokine secretion only at 1 μM

Figure 3.7: SR144528 has no effect on TLR3-mediated microglial cytokine/ chemokine secretion

Figure 3.8: SR144528 has no effect on cytokine/chemokine secretion in unstimulated control microglia

Figure 3.9: Overview of Iba1 and CD68 stainings in LPS/IFN-γ-stimulated OHSCs

Figure 3.10: SR144528 does not affect CD68 activity in the CA1 region of TLR4-stimulated OHSCs

Figure 3.11: SR144528 does not affect CD68 activity in the CA1 region of TLR3-stimulated OHSCs

Figure 3.12: SR144528 does not affect microglial Iba1 and CD68 intensities in TLR4-stimulated OHSCs

Figure 3.13: SR144528 does not affect microglial Iba1 and CD68 intensities in TLR3-stimulated OHSCs

Figure 3.14: SR144528 does not alter 3D microglial morphology in LPS/IFN-γ stimulated OHSCs

Figure 3.15: SR144528 does not alter 3D microglial morphology in PolyI:C stimulated OHSCs

Figure 3.16: SR144528 reduced TLR4-mediated BMDM cytokine/chemokine secretion only at 1 μM

Figure 3.17: 1 μM of SR144528 suppressed TLR4-induced microglial inflammatory cytokine secretion independent of CB2 receptor

Figure 3.18: 1 μM of SR144528 reduced TLR4-induced CD68 activity in the CA1 region independent of CB2

Figure 3.19: 1 μM of SR144528 decreased TLR4-induced microglial Iba1 and CD68 intensities in CB2 independent manner

Figure 3.20: 1 μM of SR144528 altered TLR4-induced microglial morphology in a CB2 independent manner

Figure 3.21: 1 μM of SR144528 neither affects cell death nor cell surface markers expression in TLR4 stimulated microglia

Figure 3.22: JWH-133 reduced LPS/IFN-γ-induced microglial cytokine/ chemokine secretion only at nanomolar concentrations

Figure 3.23: Seahorse metabolic analysis from WT and $CB2^{-/-}$ microglia after LPS/IFN-γ stimulation

Figure 3.24: Seahorse metabolic analysis from WT and $CB2^{-/-}$ Bone marrow-derived macrophages after LPS/IFN-γ stimulation

Figure 3.25: Seahorse metabolic analysis from LPS/IFN-γ-stimulated WT microglia pre-treated with 1 μM SR144528

Figure 3.26: Seahorse metabolic analysis from LPS/IFN-γ-stimulated WT BMDMs pre-treated with 1 μM SR144528

Figure 4.1: Overview of the differential effects of CB2 genetic deletion and pharmacological inhibition in TLR4-induced microglial activation

Figure 4.2: Interim summary of effects of CB2 deletion on TLR-induced microglial activation

Figure 4.3: Summary of the comparative study between CB2 deletion and pharmacological inhibition in TLR4-induced microglial activation

7. List of tables

Table 1.1: List of synthetic CB2 agonists/antagonists

Table 2.1: Different microglia protocols and media components

Table 2.2: OHSCs dissection medium composition

Table 2.3: OHSCs culture medium composition

Table 2.4: BMDMs culture medium composition

Table 2.5: List of primary antibodies used for immunocytochemistry

Table 2.6: List of secondary antibodies used for immunocytochemistry

Table 2.7: List of antibodies used for simple western assay

Table 2.8: List of antibodies used for flow cytometry

Table 2.9: List of primary antibodies used for immunohistochemistry

Table 2.10: List of secondary antibodies used for immunohistochemistry

Table 2.11: ELISA Kit and reagents used for cytokine measurement

Table 2.12: ELISA Standards

Table 2.13: Seahorse assay injected compounds

Table 2.14: Seahorse program for assay measurement

Table 2.15: Calculation of mitochondrial respiration parameters

8. References

Aderem A, Ulevitch RJ. Toll-like receptors in the induction of the innate immune response. Nature 2000; 406(6797): 782–787

Akira S, Takeda K. Toll-like receptor signalling. Nature Reviews Immunology 2004; 4(7): 499–511

Arcuri C, Mecca C, Bianchi R, Giambanco I, Donato R. The Pathophysiological Role of Microglia in Dynamic Surveillance, Phagocytosis and Structural Remodeling of the Developing CNS. Frontiers in Molecular Neuroscience 2017; 10: 191

Aso E, Juvés S, Maldonado R, Ferrer I. CB2 cannabinoid receptor agonist ameliorates alzheimer-like phenotype in AβPP/PS1 mice. Journal of Alzheimer's Disease 2013; 35(4): 847–858.

Badal S, Smith KN, Rajnarayanan R. Analysis of natural product regulation of cannabinoid receptors in the treatment of human disease. Pharmacology and Therapeutics 2017; 180: 24–48

Baik SH, Kang S, Lee W, Choi H, Chung S, Kim JI, Mook-Jung I. A Breakdown in Metabolic Reprogramming Causes Microglia Dysfunction in Alzheimer's Disease. Cell Metabolism 2019; 30(3): 493-507

Barton GM, Medzhitov R. Toll-like receptor signaling pathways. Science 2003; 300(5625): 1524–1525

Basavarajappa BS. Critical Enzymes Involved in Endocannabinoid Metabolism. Protein and Peptide Letters 2007; 14(3): 237-246

Benito C, Tolón RM, Pazos MR, Núñez E, Castillo AI, Romero J. Cannabinoid CB2 receptors in human brain inflammation. British Journal of Pharmacology 2008; 153: 277–285.

Benito C, Núñez E, Tolón RM, Carrier EJ, Rábano A, Hillard CJ, Romero J. Cannabinoid CB2 Receptors and Fatty Acid Amide Hydrolase Are Selectively Overexpressed in

Neuritic Plaque-Associated Glia in Alzheimer's Disease Brains. Journal of Neuroscience 2003; 23(35): 11136–11141

Bernier LP, York EM, MacVicar BA. Immunometabolism in the Brain: How Metabolism Shapes Microglial Function. Trends in Neurosciences 2020; 43(11): 854–869

Bielanin JP, Sun D. Significance of Microglial Energy Metabolism in Maintaining Brain Homeostasis. Translational Stroke Research 2022; 10.1007/s12975-022-01069-6

Bouaboula M, Poinot-Chazel C, Marchand J, Canat X, Bourrié B, Rinaldi-Carmona M, Calandra B, Le Fur G, Casellas P. Signaling pathway associated with stimulation of CB2 peripheral cannabinoid receptor. Involvement of both mitogen-activated protein kinase and induction of Krox-24 expression. European Journal of Biochemistry 1996; 237(3): 704-711.

Brown AJ. Novel cannabinoid receptors. British Journal of Pharmacology 2007; 152(5): 567–575

Brubaker SW, Bonham KS, Zanoni I, Kagan JC. Innate immune pattern recognition: a cell biological perspective. Annual Review of Immunology 2015; 33: 257-290

Buckley NE, McCoy KL, Mezey É, Bonner T, Zimmer A, Felder CC, Glass M, Zimmer A. Immunomodulation by cannabinoids is absent in mice deficient for the cannabinoid CB2 receptor. European Journal of Pharmacology 2000; 396(2–3): 141–149.

Capozzi A, Caissutti D, Mattei V, Gado F, Martellucci S, Longo A, Recalchi S, Manganelli V, Riitano G, Garofalo T, Sorice M, Manera C, Misasi R. Anti-inflammatory Activity of a CB2 Selective Cannabinoid Receptor Agonist: Signaling and Cytokines Release in Blood Mononuclear Cells. Molecules 2022; 27(1): 64

Carlisle SJ, Marciano-Cabral F, Staab A, Ludwick C, Cabral GA. Differential expression of the CB2 cannabinoid receptor by rodent macrophages and macrophage-like cells in relation to cell activation. International Immunopharmacology 2002; 2(1): 69–82.

Casali BT, Reed-Geaghan EG. Microglial Function and Regulation during Development, Homeostasis and Alzheimer's Disease. Cells 2021; 10(4): 957

Casano AM, Peri F. Microglia: multitasking specialists of the brain. Developmental Cell 2015; 32(4): 469–477

Castillo PE, Younts TJ, Chávez AE, Hashimotodani Y. Endocannabinoid Signaling and Synaptic Function. Neuron 2012; 76(1): 70–81

Cheng J, Zhang R, Xu Z, Ke Y, Sun R, Yang H, Zhang X, Zhen X, Zheng LT. Early glycolytic reprogramming controls microglial inflammatory activation. Journal of Neuroinflammation 2021; 18(1): 1–18

Chiurchiù V, Cencioni MT, Bisicchia E, De Bardi M, Gasperini C, Borsellino G, Centonze D, Battistini L, Maccarrone M. Distinct modulation of human myeloid and plasmacytoid dendritic cells by anandamide in multiple sclerosis. Annals of Neurology 2013; 73(5): 626–636

Chiurchiù V, Lanuti M, Catanzaro G, Fezza F, Rapino C, Maccarrone M. Detailed characterization of the endocannabinoid system in human macrophages and foam cells, and anti-inflammatory role of type-2 cannabinoid receptor. Atherosclerosis 2014; 233(1): 55–63

Colonna M, Butovsky O. Microglia Function in the Central Nervous System During Health and Neurodegeneration. Annual Review of Immunology 2017; 35: 441–468.

Correa F, Hernangómez M, Mestre L, Loría F, Spagnolo A, Docagne F, Di Marzo V, Guaza C. Anandamide enhances IL-10 production in activated microglia by targeting CB2 receptors: Roles of ERK1/2, JNK, and NF-κB. Glia 2010; 58(2): 135–147

Correa F, Mestre L, Docagne F, Guaza C. Activation of cannabinoid CB 2 receptor negatively regulates IL-12p40 production in murine macrophages: Role of IL-10 and ERK1/2 kinase signaling. British Journal of Pharmacology 2005; 145(4): 441–448

Crocq MA. History of cannabis and the endocannabinoid system. Dialogues in Clinical Neuroscience 2020; 22(3): 223-228

Cronk JC, Filiano AJ, Louveau A, Marin I, Marsh R, Ji E, Goldman DH, Smirnov I, Geraci N, Acton S, Overall CC, Kipnis J. Peripherally derived macrophages can engraft the brain

independent of irradiation and maintain an identity distinct from microglia. Journal of Experimental Medicine 2018; 215(6): 1627–1647

Cuadros MA, Navascués J. The origin and differentiation of microglial cells during development. Progress in Neurobiology 1998; 56(2): 173–189

Cuadros MA, Sepulveda MR, Martin-Oliva D, Marín-Teva JL, Neubrand VE. Microglia and Microglia-Like Cells: Similar but Different. Frontiers in Cellular Neuroscience 2022; 16: 816439

de Melo Reis RA, Isaac AR, Freitas HR, de Almeida MM, Schuck PF, Ferreira GC, Andrade-da-Costa BLDS, Trevenzoli IH. Quality of Life and a Surveillant Endocannabinoid System. Frontiers in Neuroscience 2021; 15: 747229

Deczkowska A, Keren-Shaul H, Weiner A, Colonna M, Schwartz M, Amit I. Disease-Associated Microglia: A Universal Immune Sensor of Neurodegeneration. Cell 2018; 173(5): 1073–1081

del Rio-Hortega P. El “tercer elemento” de los centros nerviosos. III. Naturaleza probable de la microglia. Bol Soc Esp Biol 1919; VIII: 108-115

del Rio-Hortega P. “Microglia” in Cytology and and Cellular Pathology of the Nervous System, ed W. Penfield (New York: Hoeber) 1932; 483 - 534

Duan T, Du Y, Xing C, Wang HY, Wang RF. Toll-Like Receptor Signaling and Its Role in Cell-Mediated Immunity. Frontiers in Immunology 2022; 13: 812774

Edler MK, Mhatre-Winters I, Richardson JR. Microglia in aging and Alzheimer’s disease: A comparative species review. Cells 2021; 10(5): 1138

Ehrhart J, Obregon D, Mori T, Hou H, Sun N, Bai Y, Klein T, Fernandez F, Tan J, Shytle D. Stimulation of cannabinoid receptor 2 (CB2) suppresses microglial activation. Journal of Neuroinflammation 2005; 2: 29

El-Brolosy MA, Stainier DYR. Genetic compensation: A phenomenon in search of mechanisms. PLoS Genetics 2017; 13(7): e1006780

Eljaschewitsch E, Witting A, Mawrin C, Lee T, Schmidt PM, Wolf S, Hoertnagl H, Raine CS, Schneider-Stock R, Nitsch R, Ullrich O. The Endocannabinoid Anandamide Protects Neurons during CNS Inflammation by Induction of MKP-1 in Microglial Cells. Neuron 2006; 49(1): 67–79

Elliott MB, Tuma RF, Amenta PS, Barbe MF, Jallo JI. Acute Effects of a Selective Cannabinoid-2 Receptor Agonist on Neuroinflammation in a Model of Traumatic Brain Injury. Journal of Neurotrauma 2011; 28(6): 973–981

Everts B, Amiel E, Huang SC, Smith AM, Chang CH, Lam WY, Redmann V, Freitas TC, Blagih J, van der Windt GJ, Artyomov MN, Jones RG, Pearce EL, Pearce EJ. TLR-driven early glycolytic reprogramming via the kinases TBK1-IKKε supports the anabolic demands of dendritic cell activation. Nature Immunology 2014; 15(4): 323-332

Falcicchia C, Tozzi F, Arancio O, Watterson DM, Origlia N. Involvement of p38 mapk in synaptic function and dysfunction. International Journal of Molecular Sciences 2020; 21(16): 5624

Fernández-Arjona MDM, Grondona JM, Fernández-Llebrez P, López-Ávalos MD. Microglial Morphometric Parameters Correlate With the Expression Level of IL-1β, and Allow Identifying Different Activated Morphotypes. Frontiers in Cellular Neuroscience 2019; 13: 472

Fiebich BL, Batista CRA, Saliba SW, Yousif NM, de Oliveira ACP. Role of microglia TLRs in neurodegeneration. Frontiers in Cellular Neuroscience 2018; 12: 329

Forte G, Sorrentino R, Montinaro A, Pinto A, Morello S. Cl-IB-MECA enhances TNF-α release in peritoneal macrophages stimulated with LPS. Cytokine 2011; 54(2): 161–166

Ginhoux F, Greter M, Leboeuf M, Nandi S, See P, Gokhan S, Mehler MF, Conway SJ, Ng LG, Stanley ER, Samokhvalov IM, Merad M. Fate mapping analysis reveals that adult microglia derive from primitive macrophages. Science 2010; 330(6005): 841–845

Ginhoux F, Lim S, Hoeffel G, Low D, Huber T, Sierra A. Origin and differentiation of microglia. Frontier in Cellular Neuroscience 2013; 7: 45

Ginhoux F, Prinz M. Origin of microglia: Current concepts and past controversies. Cold Spring Harbor Perspectives in Biology 2015; 7(8): a020537

Hansen JN, Brückner M, Pietrowski MJ, Jikeli JF, Plescher M, Beckert H, Schnaars M, Fülle L, Reitmeier K, Langmann T, Förster I, Boche D, Petzold GC, Halle A. MotiQ: an open-source toolbox to quantify the cell motility and morphology of microglia. Molecular Biology of the Cell 2022; 33(11): ar99

Hashimoto C, Hudson KL, Anderson KV. The Toll gene of drosophila, required for dorsal-ventral embryonic polarity, appears to encode a transmembrane protein. Cell 1988; 52(2): 269–279

He Y, Taylor N, Yao X, Bhattacharya A. Mouse primary microglia respond differently to LPS and poly(I:C) in vitro. Scientific Reports 2021; 11(1): 10447

Herrera B, Carracedo A, Diez-Zaera M, Guzmán M, Velasco G. p38 MAPK is involved in CB2 receptor-induced apoptosis of human leukaemia cells. FEBS Letters 2005; 579(22): 5084–5088

Hoeffel G, Ginhoux F. Fetal monocytes and the origins of tissue-resident macrophages. Cellular Immunology 2018; 330: 5–15

Howlett AC, Barth F, Bonner TI, Cabral G, Casellas P, Devane WA, Felder CC, Herkenham M, Mackie K, Martin BR, Mechoulam R, Pertwee RG. International Union of Pharmacology. XXVII. Classification of cannabinoid receptors. Pharmacological Reviews 2002; 54(2): 161–202

Perry VH. A revised view of the central nervous system microenvironment and major histocompatibility complex class II antigen presentation. Journal of Neuroimmunology 1998; 90(2): 113–121

Kacimi R, Giffard RG, Yenari MA. Endotoxin-activated microglia injure brain derived endothelial cells via NF-κB, JAK-STAT and JNK stress kinase pathways. Journal of Inflammation 2011; 8: 7

Kelly B, O'neill LA. Metabolic reprogramming in macrophages and dendritic cells in innate

immunity. Cell Research 2015; 25(7): 771–784.

Kibret BG, Ishiguro H, Horiuchi Y, Onaivi ES. New Insights and Potential Therapeutic Targeting of CB2 Cannabinoid Receptors in CNS Disorders. International Journal of Molecular Sciences 2022; 23(2): 975.

Kielian T. Toll-like receptors in central nervous system glial inflammation and homeostasis. Journal of Neuroscience Research 2006; 83(5): 711–730.

Kierdorf K, Erny D, Goldmann T, Sander V, Schulz C, Perdiguero EG, Wieghofer P, Heinrich A, Riemke P, Hölscher C, Müller DN, Luckow B, Brocker T, Debowski K, Fritz G, Opdenakker G, Diefenbach A, Biber K, Heikenwalder M, Geissmann F, Rosenbauer F, Prinz M. Microglia emerge from erythromyeloid precursors via Pu.1- and Irf8-dependent pathways. Nature Neuroscience 2013; 16(3): 273–280

Kishimoto S, Kobayashi Y, Oka S, Gokoh M, Waku K, Sugiura T. 2-Arachidonoylglycerol, an Endogenous Cannabinoid Receptor Ligand, Induces Accelerated Production of Chemokines in HL-60 Cells. J. Biochem 2004; 135: 517–524

Komorowska-Müller JA, Rana T, Olabiyi BF, Zimmer A, Schmöle AC. Cannabinoid receptor 2 alters social memory and microglial activity in an age-dependent manner. Molecules 2021; 26(19): 5984

Komorowska-Müller JA, Schmöle AC. CB2 receptor in microglia: The guardian of self-control. International Journal of Molecular Sciences 2021; 22(1): 19

Lauro C, Limatola C. Metabolic Reprograming of Microglia in the Regulation of the Innate Inflammatory Response. Frontiers in Immunology 2020; 11: 493

Lauterbach MA, Hanke JE, Serefidou M, Mangan MSJ, Kolbe CC, Hess T, Rothe M, Kaiser R, Hoss F, Gehlen J, Engels G, Kreutzenbeck M, Schmidt SV, Christ A, Imhof A, Hiller K, Latz E. Toll-like Receptor Signaling Rewires Macrophage Metabolism and Promotes Histone Acetylation via ATP-Citrate Lyase. Immunity 2019; 51(6): 997-1011.e7

Leng F, Edison P. Neuroinflammation and microglial activation in Alzheimer disease: where do we go from here? Nature Reviews Neurology 2021; 17(3): 157–172

Li L, Li N, Pang W, Zhang X, Hammock BD, Ai D, Zhu Y. Opposite effects of gene deficiency and pharmacological inhibition of soluble epoxide hydrolase on cardiac fibrosis. PLoS One 2014; 9(4): e94092

Lier J, Streit WJ, Bechmann I. Beyond activation: Characterizing microglial functional phenotypes. Cells 2021; 10(9): 2236

López A, Aparicio N, Pazos MR, Grande MT, Barreda-Manso MA, Benito-Cuesta I, Vázquez C, Amores M, Ruiz-Pérez G, García-García E, Beatka M, Tolón RM, Dittel BN, Hillard CJ, Romero J. Cannabinoid CB 2 receptors in the mouse brain: Relevance for Alzheimer's disease. Journal of Neuroinflammation 2018; 15(1): 158

Lu HC, Mackie K. Review of the Endocannabinoid System. Biological Psychiatry. Cognitive Neuroscience and Neuroimaging 2021; 6(6): 607-615

Lund H, Pieber M, Parsa R, Han J, Grommisch D, Ewing E, Kular L, Needhamsen M, Espinosa A, Nilsson E, Överby AK, Butovsky O, Jagodic M, Zhang XM, Harris RA. Competitive repopulation of an empty microglial niche yields functionally distinct subsets of microglia-like cells. Nature Communications 2018; 9(1): 4845

Ma L, Jia J, Liu X, Bai F, Wang Q, Xiong L. Activation of murine microglial N9 cells is attenuated through cannabinoid receptor CB2 signaling. Biochemical and Biophysical Research Communications 2015; 458(1): 92–97

Mado H, Adamczyk-Sowa M, Sowa P. Role of Microglial Cells in the Pathophysiology of MS: Synergistic or Antagonistic? International Journal of Molecular Sciences 2023; 24(3): 1861

Martín-Moreno AM, Brera B, Spuch C, Carro E, García-García L, Delgado M, Pozo MA, Innamorato NG, Cuadrado A, de Ceballos ML. Prolonged oral cannabinoid administration prevents neuroinflammation, lowers β-amyloid levels and improves cognitive performance in Tg APP 2576 mice. Journal of Neuroinflammation 2012; 9: 8

McCoy KL. Interaction between Cannabinoid System and Toll-Like Receptors Controls Inflammation. Mediators of Inflammation 2016; 2016: 5831315

McGrath KE, Koniski AD, Malik J, Palis J. Circulation is established in a stepwise pattern in the mammalian embryo. Blood 2003; 101(5): 1669–1675

Mecha M, Feliú A, Carrillo-Salinas FJ, Rueda-Zubiaurre A, Ortega-Gutiérrez S, de Sola RG, Guaza C. Endocannabinoids drive the acquisition of an alternative phenotype in microglia. Brain, Behavior, and Immunity 2015; 49: 233–245

Mechoulam R, Ben-Shabat S, Hanus L, Ligumsky M, Kaminski NE, Schatz AR, Gopher A, Almog S, Martin BR, Compton DR, Pertwee RG, Griffin G, Bayewitch M, Barg J, Vogel Z. Identification of an endogenous 2-monoglyceride, present in canine gut, that binds to cannabinoid receptors. Biochemical Pharmacology 1995; 50(1): 83–90

Mechoulam R, Parker LA. The Endocannabinoid System and the Brain. Annual Review of Psychology 2013; 64: 21–47

Medzhitov R, Preston-Hurlburt P, Janeway CA. A human homologue of the Drosophila toll protein signals activation of adaptive immunity. Nature 1997; 388(6640): 394–397

Melton EM, Li H, Benson J, Sohn P, Huang LH, Song BL, Li BL, Chang CCY, Chang TY. Myeloid Acat1/Soat1 KO attenuates pro-inflammatory responses in macrophages and protects against atherosclerosis in a model of advanced lesions. Journal of Biological Chemistry 2019; 294(43): 15836–15849

Merighi S, Gessi S, Varani K, Simioni C, Fazzi D, Mirandola P, Borea PA. Cannabinoid CB2 receptors modulate ERK-1/2 kinase signalling and NO release in microglial cells stimulated with bacterial lipopolysaccharide. British Journal of Pharmacology 2012; 165(6): 1773–1788

Mestre L, Correa F, Arévalo-Martín A, Molina-Holgado E, Valenti M, Ortar G, Di Marzo V, Guaza C. Pharmacological modulation of the endocannabinoid system in a viral model of multiple sclerosis. Journal of Neurochemistry 2005; 92(6): 1327–1339

Molina-Holgado F, Pinteaux E, Moore JD, Molina-Holgado E, Guaza C, Gibson RM, Rothwell NJ. Endogenous Interleukin-1 Receptor Antagonist Mediates Anti-Inflammatory and Neuroprotective Actions of Cannabinoids in Neurons and Glia. The Journal of

Neuroscience 2003; 23(16), 6470-6474

Montecucco F, Burger F, Mach F, Steffens S. CB2 cannabinoid receptor agonist JWH-015 modulates human monocyte migration through defined intracellular signaling pathways. American Journal of Physiology. Heart and Circulatory Physiology 2008; 294(3): H1145-H1155

Moreno-Fernández RD, Nieto-Quero A, Gómez-Salas FJ, Chun J, Estivill-Torrús G, de Fonseca FR, Santín LJ, Pérez-Martín M, Pedraza C. Effects of genetic deletion versus pharmacological blockade of the LPA1 receptor on depression-like behaviour and related brain functional activity. Disease models and mechanisms 2018; 11(9) dmm035519

Munro S, Thomas KL, Abu-Shaar M. Molecular characterization of a peripheral receptor for cannabinoids. Nature 1993; 365(6441): 61–65

Muzio L, Viotti A, Martino G. Microglia in Neuroinflammation and Neurodegeneration: From Understanding to Therapy. Frontiers in Neuroscience 2021; 15: 742065

Nair S, Sobotka KS, Joshi P, Gressens P, Fleiss B, Thornton C, Mallard C, Hagberg H. Lipopolysaccharide-induced alteration of mitochondrial morphology induces a metabolic shift in microglia modulating the inflammatory response in vitro and in vivo. Glia 2019; 67(6): 1047–1061

Naito M, Takahashi K, Nishikawa SI. Development, differentiation, and maturation of macrophages in the fetal mouse liver. Journal of Leukocyte Biology 1990; 48(1): 27–37

Nimmerjahn A, Kirchhoff F, Helmchen F. Neuroscience: Resting microglial cells are highly dynamic surveillants of brain parenchyma in vivo. Science 2005; 308(5726): 1314–1318

Nissl F. Über einige Beziehungen zwischen Nervenzellerkrankungen und gliösen Erscheinungen bei verschiedenen Psychosen. Arch Psychiatr 1899; 32: 1-21

O'Neill LAJ, Golenbock D, Bowie AG. The history of Toll-like receptors - redefining innate immunity. Nature Reviews Immunology 2013; 13(6): 453–460

O'Neill LAJ, Kishton RJ, Rathmell J. A guide to immunometabolism for immunologists.

Nature Reviews Immunology 2016; 16(9): 553–565

Oddi S, Scipioni L, Maccarrone M. Endocannabinoid system and adult neurogenesis: a focused review. Current Opinion in Pharmacology 2020; 50: 25–32

Ofek O, Karsak M, Leclerc N, Fogel M, Frenkel B, Wright K, Tam J, Attar-Namdar M, Kram V, Shohami E, Mechoulam R, Zimmer A, Bab I. Peripheral cannabinoid receptor, CB2, regulates bone mass. Proceedings of the National Academy of Sciences of the United States of America 2006; 103(3): 696–701

Parkhurst CN, Gan W-B. Microglia dynamics and function in the CNS. Current Opinion in Neurobiology 2010; 20(5): 595-600

Pons V, Rivest S. Beneficial Roles of Microglia and Growth Factors in MS, a Brief Review. Frontiers in Cellular Neuroscience 2020; 14: 284

Priller J, Flügel A, Wehner T, Boentert M, Haas CA, Prinz M, Fernández-Klett F, Prass K, Bechmann I, De Boer BA, Frotscher M, Kreutzberg GW, Persons DA, Dirnagl U. Targeting gene-modified hematopoietic cells to the central nervous system: Use of green fluorescent protein uncovers microglial engraftment. Nature Medicine 2001; 7(12): 1356–1361

Reusch N, Ravichandran KA, Olabiyi BF, Komorowska-Müller JA, Hansen JN, Ulas T, Beyer M, Zimmer A, Schmöle AC. Cannabinoid receptor 2 is necessary to induce toll-like receptor-mediated microglial activation. Glia 2022; 70(1): 71–88

Rinaldi-Carmona M, Barth F, Millan J, Derocq JM, Casellas P, Congy C, Oustric D, Sarran M, Bouaboula M, Calandra B, Portier M, Shire D, Brelière JC, Le Fur G. SR144528, the first potent and selective antagonist of the CB2 cannabinoid receptor. Journal of Pharmacology and Experimental Therapeutics 1998; 284(2): 644–650

Robertson F. A microscopic demonstration of the normal and pathological histology of mesoglia cells. Journal of Mental science 1900; 46(195): 724-724

Roh JS, Sohn DH. Damage-Associated Molecular Patterns in Inflammatory Diseases. Immune Network 2018; 18(4): e27

Romero-Sandoval EA, Horvath R, Landry RP, DeLeo JA. Cannabinoid receptor type 2 activation induces a microglial anti-inflammatory phenotype and reduces migration via MKP induction and ERK dephosphorylation. Molecular Pain 2009; 5: 25

Sacerdote P, Massi P, Panerai AE, Parolaro D. In vivo and in vitro treatment with the synthetic cannabinoid CP55,940 decreases the in vitro migration of macrophages in the rat: Involvement of both CB1 and CB2 receptors. Journal of Neuroimmunology 2000; 109(2): 155–163

Savage JC, Carrier M, Tremblay MÈ. Morphology of Microglia Across Contexts of Health and Disease. Methods in Molecular Biology 2019; 2034: 13–26

Schmöle AC, Lundt R, Gennequin B, Schrage H, Beins E, Krämer A, Zimmer T, Limmer A, Zimmer A, Otte DM. Expression Analysis of CB2-GFP BAC Transgenic Mice. PloS One 2015; 10(9): 0138986

Schmöle AC, Lundt R, Ternes S, Albayram Ö, Ulas T, Schultze JL, Bano D, Nicotera P, Alferink J, Zimmer A. Cannabinoid receptor 2 deficiency results in reduced neuroinflammation in an Alzheimer's disease mouse model. Neurobiology of Aging 2015; 36(2): 710–719

Schmöle AC, Lundt R, Toporowski G, Hansen JN, Beins E, Halle A, Zimmer A. Cannabinoid Receptor 2-Deficiency Ameliorates Disease Symptoms in a Mouse Model with Alzheimer's Disease-Like Pathology. Journal of Alzheimer's Disease 2018; 64(2): 379–392

Shi Q, Cheng L, Liu Z, Hu K, Ran J, Ge D, Fu J. The p38 MAPK inhibitor SB203580 differentially modulates LPS-induced interleukin 6 expression in macrophages. Central-European Journal of Immunology (2015); 40(3): 276-282

Smolders SM, Kessels S, Vangansewinkel T, Rigo JM, Legendre P, Brône B. Microglia: Brain cells on the move. Progress in Neurobiology 2019; 178: 101612

Soethoudt M, Grether U, Fingerle J, Grim TW, Fezza F, de Petrocellis L, Ullmer C, Rothenhäusler B, Perret C, Van Gils N, Finlay D, MacDonald C, Chicca A, Gens MD,

Stuart J, de Vries H, Mastrangelo N, Xia L, Alachouzos G, Baggelaar MP, Martella A, Mock ED, Deng H, Heitman LH, Connor M, Di Marzo V, Gertsch J, Lichtman AH, Maccarrone M, Pacher P, Glass M, van der Stelt M. Cannabinoid CB2 receptor ligand profiling reveals biased signalling and off-target activity. Nature Communications 2017; 8: 13958

Soulet D, Rivest S. Bone-marrow-derived microglia: myth or reality? Current Opinion in Pharmacology 2008; 8(4): 508–518

Stratoulias V, Venero JL, Tremblay MÈ, Joseph B. Microglial subtypes: diversity within the microglial community. The EMBO Journal 2019; 38(17): e101997

Streit WJ, Mrak RE, Griffin WST. Microglia and neuroinflammation: A pathological perspective. Journal of Neuroinflammation 2004; 1(1): 4

Takeda K, Kaisho T, Akira, S. Toll-like receptors. Annual Review of Immunology 2003; 21: 335–376

Tannahill GM, Curtis AM, Adamik J, Palsson-Mcdermott EM, McGettrick AF, Goel G, Frezza C, Bernard NJ, Kelly B, Foley NH, Zheng L, Gardet A, Tong Z, Jany SS, Corr SC, Haneklaus M, Caffrey BE, Pierce K, Walmsley S, Beasley FC, Cummins E, Nizet V, Whyte M, Taylor CT, Lin H, Masters SL, Gottlieb E, Kelly VP, Clish C, Auron PE, Xavier RJ, O'Neill, LAJ. Succinate is an inflammatory signal that induces IL-1β through HIF-1α. Nature 2013; 496(7444): 238–242

Tenor JL, Aballay A. A conserved Toll-like receptor is required for Caenorhabditis elegans innate immunity. EMBO Reports 2008; 9(1): 103–109

Thewke D, Freeman-Anderson N, Pickle T, Netherland C, Chilton C. AM-251 and SR144528 are acyl CoA:cholesterol acyltransferase inhibitors. Biochemical and Biophysical Research Communications (2009); 381(2): 181–186

Tolón RM, Núñez E, Pazos MR, Benito C, Castillo AI, Martínez-Orgado JA, Romero J. The activation of cannabinoid CB2 receptors stimulates in situ and in vitro beta-amyloid removal by human macrophages. Brain Research 2009; 1283: 148–154

Turcotte C, Blanchet MR, Laviolette M, Flamand N. The CB2 receptor and its role as a regulator of inflammation. Cellular and Molecular Life Sciences 2016; 73(23): 4449–4470

Van den Bossche J, O'Neill LA, Menon D. Macrophage Immunometabolism: Where Are We (Going)? Trends in Immunology 2017; 38(6): 395–406

Vander Heiden MG, Cantley LC, Thompson CB. Understanding the Warburg Effect: The Metabolic Requirements of Cell Proliferation. Science 2009; 324(5930): 1029–1033

Vaure C, Liu Y. A comparative review of toll-like receptor 4 expression and functionality in different animal species. Frontiers in Immunology 2014; 5: 316

Vijay K. Toll-like receptors in immunity and inflammatory diseases: Past, present, and future. International Immunopharmacology 2018; 59: 391–412

Vuic B, Milos T, Tudor L, Konjevod M, Perkovic MN, Jembrek MJ, Erjavec GN, Strac DS. Cannabinoid CB2 Receptors in Neurodegenerative Proteinopathies: New Insights and Therapeutic Potential. Biomedicines 2022; 10(12): 3000

Wang L, Pavlou S, Du X, Bhuckory M, Xu H, Chen M. Glucose transporter 1 critically controls microglial activation through facilitating glycolysis. Molecular Neurodegeneration 2019; 14(1): 2

Warburg O. The metabolism of carcinoma cells [1]. The Journal of Cancer Research 1925; 9(1): 148–163

Wolf SA, Boddeke HWGM, Kettenmann H. Microglia in Physiology and Disease. Annual Review of Physiology 2017; 79: 619–643

Yang I, Han SJ, Kaur G, Crane C, Parsa AT. The role of microglia in central nervous system immunity and glioma immunology. Journal of Clinical Neuroscience 2010; 17(1): 6–10

Yousif NM, de Oliveira ACP, Brioschi S, Huell M, Biber K, Fiebich BL. Activation of EP2 receptor suppresses poly(I: C) and LPS-mediated inflammation in primary microglia and organotypic hippocampal slice cultures: Contributing role for MAPKs. Glia 2018; 66(4):

708–724

Zhou Y, Ling EA, Dheen ST. Dexamethasone suppresses monocyte chemoattractant protein-1 production via mitogen activated protein kinase phosphatase-1 dependent inhibition of Jun N-terminal kinase and p38 mitogen-activated protein kinase in activated rat microglia. Journal of Neurochemistry 2007; 102(3): 667–678

Zimmer A, Zimmer AM, Hohmann AG, Herkenham M, Bonner TI. Increased mortality, hypoactivity, and hypoalgesia in cannabinoid CB1 receptor knockout mice. Proceedings of the National Academy of Sciences of the United States of America 1999; 96(10): 5780-5785

9. Acknowledgements

Profound appreciation goes to Prof. Dr. Andreas Zimmer for giving me the opportunity to do this project under his supervision. Thank you for your unwavering support all through the years, your mentorship has shaped me into becoming a better scientist. I would like to express my gratitude to Dr. Anne Schmöle for her supervision and guidance for the project. Thank you for believing in me.

I would also like to thank my thesis advisory committee members: Prof. Dr. Waldemar Kolanus, Prof. Dr. Katrin Paeschke and Prof. Dr. Dagmar Wachten for dedicating their valuable time to the fruitful discussions and their words of encouragement. This project would have been impossible without the assistance of Dr. Eva Beins, who came in at a dire time and contributed immensely to the success of this project.

A big thank you to the entire Institute of Molecular Psychiatry for fostering a stimulating environment that enabled my scientific growth. I would like to especially thank Dr. Andras Bilkei-Gorzo for always cheering me on and giving me emotional support, your kind gesture will never be forgotten. My sincere gratitude to Dr. Este Leidmaa for the positive discussions and for all you taught me. I would like to thank Kerstin Nicolai, Anne Zimmer and Edda Erxlebe for their technical and administrative support.

I would like to particularly thank my PhD colleagues Joanna Komorowska-Müller, Michela Palmisano, Alessandra Gargano and Lena-Louise Schüle. Thank you for the friendship, moral support and all our collaborations. To my friend and science buddy, Kishore Aravind Ravichandran, thank you for the shared adventures and strong support. We grew and learned together throughout this journey. Many thanks to all my friends who were there for me during the ups and downs of the journey.

I am immensely thankful to my parents, Mr. and Mrs. Olabiyi and my brothers, whose consistent support, love and prayers served as a source of strength throughout the journey. Finally, I want to offer a special thank you to my fiancé Isaac Owusu for the love and care you showered upon me all through the journey.

10. List of publications

- **Olabiyi B.F.**, Schmoele A.C., Beins E.C. and Zimmer A. (2023). Pharmacological blockade of cannabinoid receptor 2 signaling does not affect LPS/IFN-γ-induced microglial activation. *Scientific Reports*. 13(1), 11105. doi: 10.1038/s41598-023-37702-z. PMID: 37429837.

- Gargano A., **Olabiyi B.F.**, Palmisano M., Zimmer A. and Bilkei-Gorzo A. (2023). Possible role of locus coeruleus neuronal loss in age-related memory and attention deficits. *Frontiers in Neuroscience*. 17:1264253. doi: 10.3389/fnins.2023.1264253.

- Reusch N., Ravichandran K.A., **Olabiyi B.F.**, Komorowska-Müller J.A., Hansen J.N., Ulas T., Beyer M., Zimmer A. and Schmöle A.C. (2022). Cannabinoid receptor 2 is necessary to induce toll-like receptor-mediated microglial activation. *Glia.* 70(1), 71-78. doi: 10.1002/glia.24089. PMID: 3449976.

- Palmisano M., Gargano A., **Olabiyi B.F.**, Lutz B. and Bilkei-Gorzo A. (2022). Hippocampal deletion of CB1 receptor impairs social memory and leads to age-related changes in the hippocampus of adult mice. *International Journal of Molecular Sciences*. 24(1), 26. doi: 10.3390/ijms24010026. PMID: 36613469.

- **Olabiyi B.F.**, Fleitas C., Zammou B., Ferrer I., Rampon C., Egea J. and Espinet C. (2021). proNGF involvement in the adult neurogenesis dysfunction in Alzheimer's disease. *International Journal of Molecular Sciences*. 24(26), 10744 doi: 10.3390/ijms221910744. PMID: 34639085.

- Komorowska-Muller J.A., Rana T., **Olabiyi B.F.**, Zimmer A. and Schmöle A.C. (2021). Cannabinoid Receptor 2 alters socialmemory and microglial activity in an age-dependent manner. *Molecules* (Basel Switzerland). 26(19), 5984. doi: 10.3390/molecules26195984. PMID: 34641528.

- Adedara I.A., **Olabiyi B.F.**, Ojuade T.D, Idris U.F., Onibiyo E.M. and Farombi E.O. (2017). Taurine reverses Sodium Fluoride-mediated increase in inflammation, caspase-3 and oxidative damage along the Brain-Pituitary-Gonadal axis in male rats. *Canadian Journal of Physiology and Pharmacology*. doi: 10.1139/cjpp-2016-0641. PMID: 28654759.

- Oyewole O.I., **Olabiyi B.F.**, and Oladele J.O. (2017). Antioxidative Potential of Ricinus communis leaf extract on cadmium-induced Brain toxicity in rats*. Uniosun Journal of Sciences*. Volume 2, Issue 2. Online publication access: www.ujs.uniosun.edu.ng.

- Adedara I.A., Abolaji A.O., Idris U.F., **Olabiyi B.F.**, Onibiyo E.M., Ojuade T.D and Farombi E.O. (2016). Neuroprotective influence of taurine on fluoride-induced biochemical and behavioral deficits in rats. *Chemico-Biological Interactions*. 261(2017) 1-10. doi: 10.1016/j.cbi.2016.11.011. PMID: 27840156.
- Adedara I.A., Ojuade T.D, **Olabiyi B.F.**, Idris U.F., Onibiyo E.M., Ajeigbe O.F. and Farombi E.O. (2016). Taurine ameliorates renal oxidative damage and thyroid dysfunction in rats chronically exposed to fluoride. *Biological Trace Element Research*. 175(2) 388-395. doi: 10.1007/s120111- 016-0784-2. PMID: 27334436.
- Oyewole O.I., Oyedara O.O., **Olabiyi B.F.** and Fasanya T. (2013). Phytochemical, antimicrobial and toxicity studies on Phyllanthus amarus whole plant extract. *International Journal of Bioassay*. 2(3): 519-523. USA. ISSN: 2278-778X, NLM ID: 101656591.